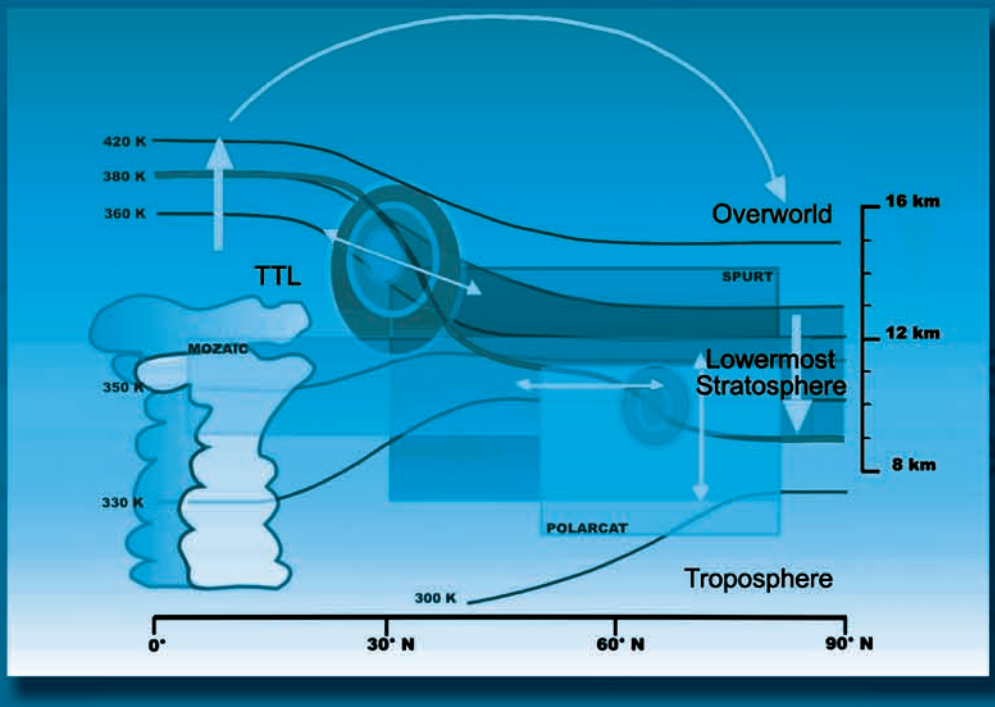

Observation– and model–based study of the extratropical UT/LS

Anne Kunz

Mitglied der Helmholtz-Gemeinschaft

JÜLICH
FORSCHUNGSZENTRUM

Schriften des Forschungszentrums Jülich
Reihe Energie & Umwelt / Energy & Environment Band / Volume 54

Forschungszentrum Jülich GmbH
Institute of Chemistry and Dynamics of the Geosphere (ICG)
Stratosphere (ICG-1)

Observation- and model-based study of the extratropical UT/LS

Anne Kunz

Schriften des Forschungszentrums Jülich
Reihe Energie & Umwelt / Energy & Environment Band / Volume 54

ISSN 1866-1793 ISBN 978-3-89336-603-3

Bibliographic information published by the Deutsche Nationalbibliothek.
The Deutsche Nationalbibliothek lists this publication in the Deutsche Nationalbibliografie; detailed bibliographic data are available in the Internet at http://dnb.d-nb.de.

Publisher and Distributor:	Forschungszentrum Jülich GmbH Zentralbibliothek, Verlag D-52425 Jülich phone:+49 2461 61-5368 · fax:+49 2461 61-6103 e-mail: zb-publikation@fz-juelich.de Internet: http://www.fz-juelich.de/zb
Cover Design:	Grafische Medien, Forschungszentrum Jülich GmbH
Printer:	Grafische Medien, Forschungszentrum Jülich GmbH
Copyright:	Forschungszentrum Jülich 2010

Schriften des Forschungszentrums Jülich
Reihe Energie & Umwelt / Energy & Environment Band / Volume 54

D 468 (Diss., Wuppertal, Univ., 2009)

ISSN 1866-1793
ISBN: 978-3-89336-603-3

Abstract

Coupling between processes of different nature, as radiation, dynamics and chemistry, in the upper troposphere and lower stratosphere (UT/LS) makes this region highly sensitive to climate change. This thesis addresses the climatological representativeness of trace gases measured in–situ within the UT/LS as well as their temporal variability. Possible atmospheric processes which may contribute to the maintenance of tropopause related structures in the extratropics are discussed. These studies are based on the closely linked use of experimental data, statistical analyzes and atmospheric models.

In the first part of this thesis, a statistical analysis is presented for the comparability of water vapor (H_2O) and ozone (O_3) data sets sampled during the SPURT aircraft campaigns and the MOZAIC passenger aircraft flights. A different variability character in both trace gas data sets is evident by a variance analysis. While the SPURT H_2O data can only resolve atmospheric processes variable on a diurnal or synoptic time scale, MOZAIC H_2O data also resolve processes on an inter–seasonal and a seasonal time scale. The SPURT H_2O data set does not represent the full MOZAIC H_2O variance in the UT/LS for climatological investigations, whereas the variance of O_3 is much better represented. SPURT H_2O data are better suited in the stratosphere, where the MOZAIC relative humidity sensor loses its sensitivity. This is the first analysis which addresses the ability of measured trace gases to detect the atmospheric variability in the UT/LS.

In the second part of the thesis, the relationship between the static stability N^2 within the tropopause inversion layer (TIL) in the extratropics and the atmospheric mixing in that region is investigated using the SPURT O_3 and CO observations. For this purpose N^2 is determined from ECMWF fields. A new measure of mixing degree based on O_3–CO tracer correlations is developed. It is found that high N^2 is related to an enhanced mixing degree in the extratropical mixing layer. A temporal variance analysis of N^2 at the particular SPURT measurement locations suggests that the processes responsible for the composition of the TIL occur on a seasonal time scale. The Reading radiative transfer model is used to simulate the influence of a change in O_3 and H_2O vertical gradients on the temperature gradient and thus on the static stability above the tropopause. Zonal and time mean ECMWF O_3 and H_2O profiles, which

are used as reference mixed profiles, are perturbed to represent idealized non–mixed profiles in the atmosphere. The results of the simulations show that N^2 increases with enhanced mixing degree near the tropopause and a temperature inversion develops. In the idealized case of non–mixed profiles the TIL vanishes. H_2O plays the dominant role in maintaining the temperature inversion and the TIL structure compared to O_3. Here, the two different atmospheric features, i.e., the mixing layer and the TIL in the extratropics, are discussed together for the first time.

In the last part of the thesis, the gradient of the potential vorticity with equivalent latitude is used to determine the core of the jet streams and its meridional boundaries on different middle world isentropes (300–380 K). The jet cores represent a physical boundary on the isentropes between the troposphere at lower latitudes and the stratosphere at higher latitudes. Thus, a PV gradient tropopause related to the isentropic gradient of the potential vorticity is proposed, which may represent the separation between the two atmospheric reservoirs troposphere and stratosphere in a more appropriate manner than the use of a particular value of PV. Dependent on season the zonal and time mean PV at this newly defined tropopause varies between 2.0 PVU–3.5 PVU and decreases from lower toward higher latitudes in the northern hemisphere. This decrease is sharper on the southern hemispheres compared to the northern hemisphere. The analysis indicates that as the dynamical tropopause the commonly used 2 PVU threshold is too low most of the time. With the help of tracer correlations and a new coordinate system, using equivalent latitude relative to the jet core, the isentropic distribution and transition of the static stability across the PV gradient tropopause is analyzed. This transition is more pronounced during winter than summer on each isentrope in the lowermost stratosphere, which is consistent with the transport barrier at the jet streams related to the sharpness of the tropopause.

Zusammenfassung

Durch die Kopplung verschiedener atmosphärischer Prozesse, wie Strahlung, Dynamik und Chemie, ist die Region der oberen Troposphäre und untere Stratosphäre (UT/LS) sensitiv für Klimaänderungen. Die vorliegende Dissertation widmet sich der klimatologischen Repräsentativität von in–situ gemessenen Spurengasen in der UT/LS, sowie deren zeitlichen Variabilität. Mögliche atmosphärische Prozesse, die zum Erhalt von extratropischen Phänomenen gekoppelt an die Tropopause führen können, werden diskutiert. Die Analysen basieren auf dem gemeinsamen Gebrauch von experimentellen Daten, statistischen Analysen und atmosphärischen Modellen.

Im ersten Teil der Arbeit wird eine statistische Analyse präsentiert, welche die Vergleichbarkeit von Datensätzen wie z.B. Wasserdampf (H_2O) und Ozon (O_3) untersucht. Die Daten stammen aus den SPURT Kampagnen und den kommerziellen MOZAIC Flügen. Eine Varianzanalyse macht deutlich, dass beide Spurengasdatensätze einer unterschiedlichen zeitlichen Variabilität unterliegen. Während die SPURT H_2O Daten nur atmosphärische Prozesse auf einer Tageszeitskala oder einer synoptischen Zeitskala beinhalten, repräsentieren die MOZAIC Daten auch Prozesse, die auf einer Zeitskala von einigen Monaten bis zu einer Jahreszeitenskala bedeutend sind. Der SPURT H_2O Datensatz kann die MOZAIC H_2O Varianz in der UT/LS, welche für klimatologische Untersuchungen bedeutend ist, nicht repräsentieren. Dies gilt allerdings nicht für die O_3 Varianz in SPURT, welche mit der MOZAIC O_3 Varianz gut übereinstimmt. Die SPURT H_2O Daten sind in der Stratosphäre besser geeignet als die MOZAIC H_2O Daten, denn der MOZAIC Relative Feuchte Sensor verliert in der Stratosphäre seine Sensitivität. Dies ist die erste Analyse zur Untersuchung von gemessenen Spurengasen hinsichtlich ihrer Qualität die atmosphärische Variabilität in der UT/LS zu beschreiben.

Im zweiten Teil der Arbeit wird der Zusammenhang zwischen statischer Stabilität N^2 in der extratropischen Tropopauseninversionsschicht (TIL) und der atmosphärischen Vermischung in der UT/LS mit den SPURT O_3 und CO Daten untersucht. Hierfür wird N^2 aus operationellen Daten (ECMWF) bestimmt. Ein neues Maß für den Vermischungsgrad basierend auf O_3–CO Spurengaskorrelationen wird eingeführt. Es wird deutlich, dass ein hohes N^2 mit einem erhöhten Grad der Vermischung in der extratropischen Vermischungsschicht zusam-

menhängt. Eine Varianzanalyse von N^2 an den jeweiligen SPURT Messorten zeigt eine jahreszeitlich variierende Varianz und deutet somit auf Prozesse auf dieser Zeitskala hin, welche die TIL beeinflussen können. Mit dem Reading Strahlungstransfermodell wird der Einfluss einer Veränderung der O_3 und H_2O Vertikalgradienten und somit der statischen Stabilität oberhalb der Tropopause untersucht. Zonal und zeitlich gemittelte ECMWF O_3 und H_2O Referenzprofile, welche implizit eine Vermischung enthalten, werden gezielt gestört, so dass sie idealisierte Profile ohne Vermischung in der Atmosphäre repräsentieren. Die Ergebnisse zeigen, dass mit einer Erhöhung der Vermischung in Tropopausennähe N^2 ansteigt und die Temperaturinversion ausgebildet wird. Im idealisierten Fall ohne Vermischung existiert keine TIL. H_2O spielt eine größere Rolle als O_3 bei der Erhaltung der Temperaturinversion und der Struktur der TIL. Die Vermischungsschicht und die TIL in den Extratropen werden das erste Mal gemeinsam untersucht.

Im letzten Teil der Arbeit wird der Kern der Strahlströme sowie deren meridionalen Grenzen auf verschiedenen Isentropen (300–380 K) mittels Gradient der Potentiellen Vorticity (PV) auf äquivalenten Breiten bestimmt. Die Kerne der Strahlströme repräsentieren eine physikalische Grenze auf Isentropen zwischen der Troposphäre in niederen geographischen Breiten und der Stratosphäre in höheren Breiten. Eine 'PV–Gradiententropopause' wird präsentiert, welche die Trennung zwischen den beiden atmosphärischen Reservoirs besser repräsentieren kann als die gewöhnliche Verwendung eines festen PV Wertes. Die PV auf dieser neuen Tropopause variiert jahreszeitenabhängig von 2.0 PVU–3.5 PVU, wobei sie in Richtung Pol abnimmt. Diese Abnahme ist schärfer auf der Südhemisphäre als auf der Nordhemisphäre. Die Analyse deutet an, dass der oft verwendete feste 2 PVU Schwellenwert als dynamische Tropopause meist zu niedrig ist. Mittels Spurengaskorrelationen und einer neuen Koordinate, der äquivalenten Breite relativ zum Kern des Strahlstroms, wird die isentrope Verteilung und der Übergang der statischen Stabilität durch die PV Gradiententropopause analysiert. Der Übergang ist im Winter auf jeder Isentrope der unteren Stratosphäre ausgeprägter als im Sommer. Dies steht im Einklang mit dem Strahlstrom, der im Winter als Transportbarriere agiert verbunden mit einer schärferen Tropopause.

Contents

List of Figures

List of Tables

Chapter 1

Introduction

1.1 Upper troposphere and lower stratosphere (UT/LS)

The upper troposphere and lower stratosphere (UT/LS) is the transition region between the troposphere and the stratosphere, and is characterized by exchange processes between these two atmospheric regions. The UT/LS is a highly coupled region: dynamics, chemistry, microphysics, and radiation are fundamentally interconnected. The concentration of water vapor and ozone, two of the most important greenhouse gases in the UT/LS, is controlled by both transport processes, such as stratosphere–troposphere exchange, and also chemical processes including multiphase chemistry or cloud microphysics, which in turn are influenced by the temperature and aerosol distributions.

There are some distinct characteristics of the UT/LS which influence the Earth's climate. The UT/LS contains the coldest part of the lower atmosphere. The low temperatures have an impact on chemical reactions and thus on photochemical processes, and make the radiative forcing sensitive to the distribution of climate–relevant trace gases (Forster et al., 1997; Shepherd, 2007). Thus, a change in the atmospheric composition in the UT/LS region affects surface climate change and has an impact on the chemical and dynamical evolution of the stratosphere. The UT/LS contains a large extent of particles which facilitate heterogeneous reactions on solid substrates and multiphase reactions in liquid droplets. The particles, e.g., in cirrus clouds, can directly interact with the radiation. Thus, in the UT/LS the interaction of the radiation with greenhouse gases, cirrus cloud particles and aerosols strongly influence the Earth's radiative balance (e.g., Forster and Shine, 1997). Dynamics and radiative cooling are significant for the cold temperatures in the UT/LS. As a consequence, the greatest radiative forcing of greenhouse gases occurs in the UT/LS region. The strong coupling of different processes makes the UT/LS highly sensitive to climate change (see e.g., Shepherd, 2002). Furthermore, it has been suggested that the height of the tropopause serves as an

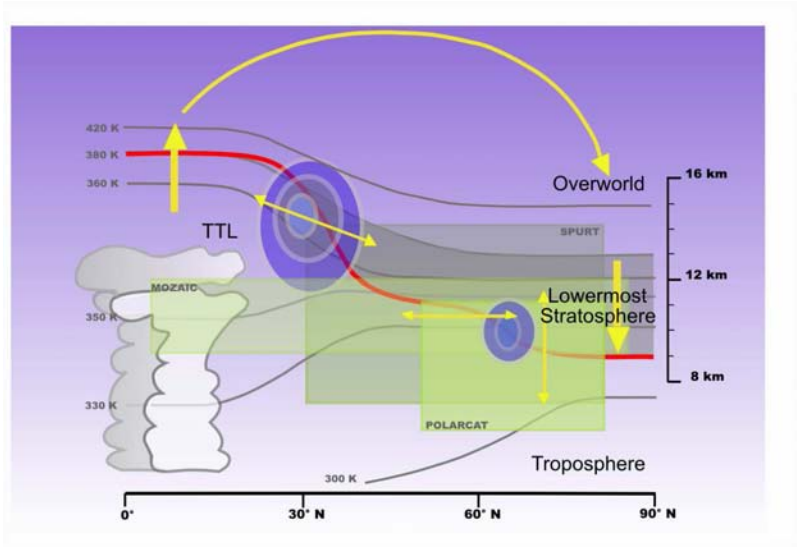

Figure 1.1: Schematic of the dynamical contribution to stratosphere–troposphere exchange. The tropopause (solid red line) separates the troposphere from the stratosphere. The lowermost stratosphere in the extratropics extends between the tropopause and the 380 K isentrope (solid gray line). The overworld is the region above the 380 K isentrope. Air masses are moved upward in the tropics from the tropical transition layer (TTL) into the LS (broad upward–directed arrow). Transport from lower to higher latitudes by the Brewer–Dobson circulation is indicated by the yellow curved arrow in the overworld. In the extratropics, these air masses are moved into the lowermost stratosphere due to large–scale subsidence. Further, exchange processes occur via isentropic transport (horizontal yellow double–headed arrows) by eddy motions, including tropical upper tropospheric troughs and midlatitude tropopause folds, from and to the troposphere across the jet streams (blue contours). Tropopause deformations occur in the vicinity of the polar front and via diabatic ascent or descent due to convection or stratospheric intrusions (thin vertical yellow double–headed arrows). The altitude range of aircraft campaigns, such as that of SPURT, MOZAIC and POLARCAT–GRACE, is marked by green areas.

useful indicator of climate change (e.g. Santer et al., 2003). Therefore, it is of great scientific interest to investigate the role of the different processes contributing to the structure of the UT/LS. Following Holton et al. (1995) and Hintsa et al. (1998), the relevant dynamical aspects of the stratosphere–troposphere exchange influencing the structure of the UT/LS are now discussed in a 2D–picture of the lower atmosphere (Figure 1.1).

The exchange of air masses between the stratosphere and the troposphere in the UT/LS takes place across the tropopause. The existence of the tropopause has been known for more than a century (e.g., Hoinka, 1996). The tropopause (Figure 1.1, solid red line) separates

the well mixed troposphere from the stratified stratosphere and is thus characterized by an increase in static stability (buoyancy frequency squared, N^2). In a climatological mean, the zonally averaged height of the tropopause decreases from the tropical region toward the polar regions (Hoinka, 1998). The tropical tropopause is roughly at $\approx 17\,\mathrm{km}$ and slopes down toward the polar regions at $\approx 9\,\mathrm{km}$.

There are several concepts for defining the tropopause. The conventional definition is the *thermal tropopause*, which is located at the lowest level at which the temperature lapse rate $\gamma = \frac{\partial T}{\partial z}$, where T is temperature and z is altitude, decreases below $\gamma = 2\,\mathrm{K\,km^{-1}}$. Hereby, the average of γ between this level and all higher levels within 2 km has to remain below this value (WMO, 1957). This conventional definition of the tropopause obscures the fact that the tropopause often behaves like a material surface. This quasi–material behavior can be rationalized by assuming that the tropical tropopause corresponds roughly to an isentropic surface, with a potential temperature of $\theta = 380$ K in the annual mean, and the extratropical tropopause is close to a potential vorticity surface (Holton et al., 1995). Thus there is also the definition of a *dynamical tropopause*, which is defined by Ertel's potential vorticity PV, a conserved property for adiabatic and frictionless motion (e.g., Ertel, 1942; Hoskins, 1991). This tropopause is the lowest level at which the PV exceeds a certain threshold (WMO, 1986). Different threshold values are used in literature, ranging between 1 and 4 PVU (1 PVU $= 10^{-6}\,\mathrm{K\,m^2\,kg^{-1}\,s^{-1}}$) (see e.g., Hoerling et al., 1991; Holton et al., 1995; Wirth, 2000). There is also a chemically defined tropopause based on specific thresholds in trace gas concentrations such as ozone, which in individual midlatitude upper tropospheric flow disturbances is in good agreement with the dynamical tropopause (Bethan et al., 1996; Wirth, 2000). A method for defining this chemical tropopause is the use of correlations between a tropospheric tracer (CO) and a stratospheric tracer ($\mathrm{O_3}$) (Pan et al., 2004; Zahn et al., 2004). A meaningful definition of the tropopause should be consistent with the change of chemical composition across the tropopause region. Pan et al. (2004) suggested the chemical transition between the stratosphere and the troposphere is centered around the thermal tropopause.

For meteorological analysis, a vertical coordinate different from the geometrical height, isolines of constant potential temperature (Figure 1.1, solid gray lines), is used. Depending on these isentropes, the lower atmosphere is divided into three different parts (Hoskins, 1991; Holton et al., 1995), which are explained in the following. The tropical tropopause roughly corresponds to the 380 K isentropic surface, but toward the extratropics the tropopause and the 380 K isentrope do not coincide. The *overworld* is the region where the isentropes are entirely within the stratosphere, i.e., isentropes above the 380 K isentrope. Air parcels within this region cannot reach the troposphere due to quasi–horizontal isentropic

transport. Air parcels have to descend across isentropic surfaces related by diabatic cooling to reach the troposphere. In contrast, the *underworld* lies entirely within the troposphere. Tropospheric air parcels have to rise diabatically to reach the stratosphere. The *middle world* is located between the 380 K isentrope and the tropopause (Figure 1.1, gray shaded area). It is also called the lowermost stratosphere, which is characterized by isentropes lying in the troposphere at low latitudes and in the stratosphere at high latitudes. These isentropes cross the extratropical tropopause (Hoskins, 1991) and a bidirectional exchange between both parts of the middle world is possible (Holton et al., 1995).

Due to transport processes between the troposphere and stratosphere, the lowermost stratosphere is a convergence zone between tropospheric and stratospheric air (Holton et al., 1995; Hoskins, 1991). The gradient of stratospheric and tropospheric radiative active trace gases, e.g., O_3 and H_2O, is enhanced over a large altitude range in the lowermost stratosphere. The trace gases are transported into the lowermost stratosphere from their source regions, the stratosphere and the troposphere, respectively. This transport across the tropopause plays an important role in determining the chemical composition and radiative properties both in the troposphere and stratosphere. Therefore, the investigation of transport into the middle world is valuable in order to understand climate change on the Earth. Thus the structure of the lowermost stratosphere (Figure 1.1, gray area) is strongly determined by large– and small–scale transports of trace gases. In the following, the governing processes which lead to the exchange of air masses between the stratosphere and the troposphere are discussed.

A net upward mass flux from the troposphere to the stratosphere in the tropics (Figure 1.1, yellow upward arrow) is balanced by a net downward flux from the stratosphere to the troposphere in the extratropics (Figure 1.1, yellow downward arrow). There is a vertical mixing of trace gases into the tropical tropopause layer (TTL) in the tropics (Atticks and Robinson, 1983; Konopka et al., 2007; Fueglistaler et al., 2009; Plöger et al., 2009). The TTL couples the Hadley circulation in the tropical troposphere with the much slower Brewer–Dobson circulation in the stratosphere. The TTL extends from the level of main convective outflow at around 14 km to the level above the cold point tropopause located at around 18.5 km. Figure 1.1 shows the mean level of main convective outflow at the lower limit of the TTL above the isentropic surface $\theta = 350\,\mathrm{K}$ (upper level of the white convective clouds), but the highest level of observed single deep convective events may well be up to $\theta = 380\,\mathrm{K}$ (Sherwood and Dessler, 2001). The upper limit of the TTL is around $\theta = 425\,\mathrm{K}$ (Konopka et al., 2007; Fueglistaler et al., 2009). Laterally, the TTL is bounded by the seasonally varying position of the subtropical jet streams. After air masses are transported upward near the equator due to the convective processes resulting from the intensive solar insolation and

entering the TTL above the level of main convective outflow, the air is radiatively heated under all sky conditions. Above $\theta = 360\,\mathrm{K}$, the level of zero clear sky radiative heating, short–wave radiation is strong enough to drive the tropical upwelling (Randel et al., 2002). Due to this tropical upwelling, the air slowly rises into the stratosphere above the TTL and the trace gas concentrations in the tropical lower stratosphere are changed.

Because of the cold tropopause in the tropics, H_2O is freeze–dried to the ice saturation mixing ratio when entering the stratosphere. This process is responsible for the dryness of the stratosphere. The low water vapor signal is 'remembered' by the air masses on their upward transport pathways into the stratosphere. Seasonal differences in the tropical tropopause temperatures affect the H_2O mixing ratios through the entire stratosphere. The related time–dependent transport pattern of alternating higher and lower H_2O mixing ratios is commonly referred to as the atmospheric tape recorder (Mote et al., 1996, 1998). The H_2O signal of this atmospheric tape recorder can be observed up to 10 hPa (30 km) almost 18 months after the air has passed through the tropopause. Due to the dehydration to the very low saturation mixing ratios characteristic for this region, the observed tropical stratospheric water vapor mixing ratios are often lower than the saturation mixing ratio at the mean tropopause temperature (Holton and Gettelman, 2001). The lowest values of H_2O are thus found near the tropical tropopause, where Schiller et al. (2009) observed efficient dehydration down to the lowest H_2O mixing ratios of less than 2 ppmv.

The large–scale circulation of the stratosphere, with rising motion at low latitudes followed by poleward motion and descent at high latitudes, is described by the Brewer–Dobson circulation (Figure 1.1, thin yellow curved arrow). The model of this circulation was first described by Brewer (1949) and Dobson et al. (1946) based on water vapor or column ozone measurements, respectively. As a consequence of the Brewer–Dobson circulation ozone and other trace gases are transported poleward and downward. This transport leads to a low ozone concentration within its source region in the tropical LS and to a high ozone concentration within the polar LS. In the LS, transport processes dominate the distribution of ozone because of its photochemical lifetime of several months (Sankey and Shepherd, 2003; Shepherd, 2007). The large scale Brewer–Dobson circulation is driven by wave drag (e.g., Holton et al., 1995; Haynes and Shuckburgh, 2000a), which can be quantified by the Eliassen–Palm flux divergence, related to extratropical pumping with the circulation at any level controlled by the wave drag above that level. The extratropical stratosphere and mesosphere act persistently upon the tropical lower stratosphere as a kind of global–scale fluid–dynamical suction pump, driven by certain eddy motions. The causes of this air flow can be understood by taking into account processes in the Earth's radiation equilibrium, planetary waves and subsidence processes in the polar vortex. Eddy effects give

a persistently one–way pumping action with seasonally and annually varying strength. The air parcels, which are pulled upward into the tropical stratosphere, are adiabatically cooled below radiative values and pushed poleward and downward, where adiabatic warming leads to temperatures of the air parcels above radiative values. This mechanically pumped global–scale circulation is often referred to as 'wave–driven circulation' (Holton et al., 1995). There is a rapid adiabatic exchange of air masses between the upper troposphere and lower stratosphere along isentropic surfaces across the tropopause (Figure 1.1, yellow horizontal double–headed arrows) in the vicinity of the jet streams (blue contours) (Stohl et al., 2003; Holton et al., 1995). Bidirectional mixing on isentropes across the extratropical tropopause takes place on synoptic time scales (Chen, 1995; Dethof et al., 2000). In any case the vertical exchange in the troposphere takes hours to days, and the mixing of the stratosphere months to years. This horizontal exchange is related to a two–way mixing of air masses. The diabatic vertical bidirectional exchange process mainly takes place within the extratropics (Figure 1.1, thin yellow vertical arrows) where it is associated with synoptic scale baroclinic eddies. These have been identified as being associated with dynamical processes. The synoptic scale and mesoscale processes are tropopause folds near the polar and subtropical jet streams (Hoskins and Bretherton, 1972; Shapiro, 1980; Sprenger et al., 2003). These mesoscale processes are the key features of cross–tropopause exchange especially in the subtropics, whereas in the extratropics other tropopause structures are also of importance (Sprenger et al., 2003). Cutoff lows (Ancellet et al., 1994; Sprenger et al., 2007), filamentation and fragmentation of stratospheric streamers (Appenzeller and Davies, 1992; Sprenger et al., 2003; Wernli and Sprenger, 2007; Sprenger et al., 2007), mesoscale convective systems and thunderstorms (Poulida et al., 1996) and breaking gravity waves (Lamarque et al., 1996) also play a role in cross tropopause exchange in the extratropics. Tropopause folds are intrusions of stratospheric air into the troposphere along strongly tilted isentropes. These are related to an upper–tropospheric baroclinic zone as a result of cross frontal secondary circulation associated with jet streams in upper level troughs and cutoff lows (Rao et al., 2008). There is an annual cycle of tropopause folds, with a significantly smaller frequency of tropopause folds in summer than in all other seasons (Elbern et al., 1998; Sprenger et al., 2003). The stratospheric (tropospheric) PV streamers are rather narrow filaments of high–PV air, which extend far toward the equator (pole).

Diabatic ascent or descent, such as moist convection or stratospheric intrusions from the overworld also play a role in the extratropics. Convection has been identified as penetrating the tropopause and injecting boundary layer air directly into the lowermost stratosphere within several hours (Poulida et al., 1996; Fischer et al., 2003). The actual transport from the lowermost stratosphere into the troposphere is due to small scale processes. These

processes are associated with anticyclones and filamentation events. In addition, radiative processes associated with the decay of anticyclones might also play a part in the transport of air into the lowermost stratosphere in the extratropics (Zierl and Wirth, 1997). All these processes make the middle world an important seasonally variable region, which affects the coupling between the TTL and subtropical jet streams to the midlatitudes and polar regions. These rather localized exchange processes between the troposphere and the stratosphere affect an irreversible mixing in the extratropical UT/LS. This mixing leads to the formation of a so–called mixing layer around the extratropical tropopause, which was first described by Dessler et al. (1995) and further analyzed by Fischer et al. (2000) and Hoor et al. (2002, 2004). This mixing layer has a large seasonal variability (Krebsbach et al., 2006; Brioude et al., 2008) with a higher vertical extend in summer than in winter (Hoor et al., 2002). It exhibits the photochemical characteristics of both the troposphere and the stratosphere and the gradient of climate–relevant trace gases is changed. Due to radiative forcing of surface temperatures, an enhancement of O_3 near the tropopause contributes to a temperature increase, but an enhancement of H_2O to a temperature decrease (Forster, 1999; Forster and Shine, 2002). This also has an impact on the temperature gradient and the static stability near the tropopause and thus influences the sharpness of the extratropical tropopause. Birner et al. (2002, 2006) observed a strong mean temperature inversion above a sharp local tropopause evident from radiosonde profiles with a vertical extension of about 2 km and a temperature increase of about 4 K. This phenomenon is commonly called Tropopause Inversion Layer (TIL), and involves a sharp maximum in static stability (buoyancy frequency squared, N^2) above the thermal tropopause. Different processes maintaining the TIL have been suggested in the literature. The TIL is presented as a result of poleward heat fluxes together with extratropical baroclinic eddies (Birner, 2006; Birner et al., 2006), or as a result of anticyclonic influences (Wirth, 2003) or as result of radiative effects of climate–relevant trace gases H_2O and O_3 (Randel et al., 2007b; Kunz et al., 2009). However, no process has yet been identified as the primary contributor to the maintenance of the TIL.

1.2 Overview of the thesis

This thesis makes use both of the MOZAIC (Measurement of Ozone and Water Vapour by Airbus In-Service Aircraft) long–time measurements onboard passenger aircraft and of measurements from the SPURT (Trace gas transport in the tropopause region) and POLARCAT–GRACE (Greenland Aerosol and Chemistry Experiment) aircraft campaigns for an observational study of the UT/LS to understand and quantify atmospheric processes in this region.

The MOZAIC data, which are based on at least two flights per day, and the SPURT data, which are distributed equally over the seasons, are well suited to test the climatological behavior of the UT/LS. The POLARCAT–GRACE measurements serve as a spatial extension of the SPURT measurements toward the northern hemisphere polar regions. All three data sets deliver sufficient H_2O, O_3 and CO data within the extratropical UT/LS. Figure 1.1 shows the vertical and meridional extension of the flights during these three different projects (green transparent boxes). Chapter 2 will give a short survey of the MOZAIC, SPURT and POLARCAT projects including a short introduction to the measurement systems.

Chapter 3 describes a statistical analysis of the data sets obtained in the two projects MOZAIC and SPURT (see also Kunz et al., 2008). A statistical procedure is presented suitable for comparing trace gas data sets from different sources even if they do not coincide in space and time. Data from the sparse SPURT flights are tested against data from the frequent MOZAIC flights in terms of the representativeness of the atmospheric variability of trace gases within the European UT/LS. The tests are adapted for an application on field measurements, but are also suited for an evaluation of atmospheric models.

Chapter 4 will contribute to the discussion on the different maintenance processes of the TIL. In particular, the link between mixing and the formation of the tropopause inversion layer (TIL) in the UT/LS is analyzed with the help of SPURT observations (see also Kunz et al., 2009). The results are additionally supported by an analogous investigation of the POLARCAT–GRACE observations. A new measure for the degree of extratropical mixing f_{mix} is deduced from SPURT O_3 and CO tracer–tracer correlations and the correlation between f_{mix} and static stability N^2 in the extratropical tropopause region is analyzed. The spatial and temporal behavior of N^2 within the TIL is investigated with backward trajectory calculations using CLaMS, the Chemical Lagrangian Model of the Stratosphere (McKenna et al., 2002b,a; Konopka et al., 2007). The influences of the climate–relevant trace gases O_3 and H_2O on the temperature gradient and thus on N^2 and the TIL above the tropopause is analyzed using the Reading radiative transfer model (Shine, 1991; Forster, 1999). Further the relation between the upper tropospheric dynamics, which can be inferred from the ECMWF relative vorticity field, and the TIL above the tropopause is examined.

Chapter 5 presents a method to determine the location of the core of the jet streams $J_c(\theta)$ and the location of their respective boundaries $J_b(\theta)$ on middle world isentropes θ between 300 K and 380 K. The jet boundaries $J_b(\theta)$ describe the meandering and splitting parts of the respective jet streams. This determination is based on the gradient of the potential vorticity with equivalent latitude on isentropes. The potential vorticity gradient on isentropes was also used by Nash et al. (1996) to determine the edge of the polar vortex. In this thesis, the procedure of Nash et al. (1996) is extended and modified and the isentropic gradient of the

PV is for the first time adapted in order to determine the location of the jet streams. The extratropical tropopause is alternatively identified by a sharp horizontal gradient of the PV along isentropic surfaces (Hoskins et al., 1985). Thus the gradient of the PV is used to define a new dynamical tropopause $\mathrm{TP}_{\mathrm{gradPV}}$. The concept of $\mathrm{TP}_{\mathrm{gradPV}}$ is based on the spatial and time–dependent location of the PV gradient, which gives a more physical definition of a transport barrier as the tropopause. In contrast, the conventional dynamical tropopause $\mathrm{TP}_{\mathrm{dyn}}$ is based on a particular chosen PV value.
Each chapter contains a clear summary of the results of that chapter. Chapter 6 gives an overall summary of the thesis together with the outlook for possible future research on UT/LS related processes.

Chapter 2

Survey of airborne projects

The strong variability of the processes within the UT/LS in time and space implies a highly variable composition of the tropopause region in different seasons and different geographical regions. To understand and quantify atmospheric processes within the extratropical UT/LS several aircraft campaigns have been performed during the past two decades.

On the one hand, there are long–time measurements onboard passenger aircraft, e.g., measurements of the projects CARIBIC (Civil Aircraft for Regular Investigation of the Atmosphere Based on an Instrument Container) (Brenninkmeijer et al., 2007) or MOZAIC (Measurement of Ozone and Water Vapour by Airbus In-Service Aircraft) (Marenco et al., 1998). CARIBIC is based on an airfreight container with automated instruments for measuring trace gases and has been operated on a monthly basis during long–distance flights since 1997. Within the MOZAIC program civil aircraft are in regular service for making routinely measurements of chemical species in the atmosphere with almost global coverage. The project was initiated in 1993 with automatic in–situ H_2O and O_3 measurements onboard of up to five long–range A340 aircraft (Marenco et al., 1998). To date at least four flights are performed each day. In 2005, MOZAIC became part of the new European Research Infrastructure project IAGOS–ERI (In–service Aircraft for a Global Observing System), which will establish and operate a distributed infrastructure for longterm observations of the atmospheric composition, aerosol and cloud particles. This is done on a global scale by a fleet of initially 10–20 long–range in–service aircraft of internationally operating airlines.

On the other hand there are data from single aircraft campaigns using research aircraft. For example, the START (Stratosphere–Troposphere Analyses of Regional Transport) experiment was motivated to examine the behavior of the extratropical tropopause and the chemical structure of the extratropical UT/LS under a variety of dynamical conditions to investigate stratosphere–troposphere exchange (Pan et al., 2007a, 2009a). The two experiments in December 2005 and in April to June 2008 were operated from Boulder Colorado and had a

challenging stacked flight pattern at different levels above an extensive geographical region of North America. The SPURT (Trace gas transport in the tropopause region) aircraft campaigns including 36 flights between November 2001 and July 2003 deliver the distribution of a wide range of trace gases in the UT/LS region above Europe. As the campaigns cover all seasons, an accurate data set with climatological character should have been obtained to study atmospheric transport and to investigate seasonal variability of trace gases in the UT/LS (Engel et al., 2006). Within the project POLARCAT (Polar Study using Aircraft, Remote Sensing, Surface Measurements and Models, of Climate, Chemistry, Aerosols, and Transport) a campaign was performed in July 2008 above Greenland which delivered data of the summer polar UT/LS.
In this thesis, observations from three different airborne projects, e.g., SPURT, MOZAIC and POLARCAT–GRACE (Greenland Aerosol and Chemistry Experiment), are used to analyze the distribution of trace gases in the UT/LS. The SPURT data, which are distributed equally over the seasons, and the MOZAIC data, which are based on at least two flights per day, are well suited to test the climatological behavior of the UT/LS. The POLARCAT–GRACE measurements serve as an ideal spatial extension of the SPURT measurements toward the northern hemisphere polar regions. Thus, the following chapter gives a short survey of the three projects SPURT, MOZAIC and POLARCAT–GRACE. These three projects deliver sufficient measurements of typical tropospheric and stratospheric tracers, e.g., H_2O, O_3 and CO, in the UT/LS and may be well suited to test the climatological behavior of the extratropical UT/LS in the northern hemisphere.

2.1 SPURT, MOZAIC and POLARCAT–GRACE projects

The aim of the SPURT research program was to understand the role of the dynamical and the chemical processes in the extratropical UT/LS. This particularly includes the improvement of the scientific understanding of the governing processes. Therefore, high resolution airborne in–situ measurements of different chemical tracers are performed, such as O_3, H_2O, NO_y, CO, N_2O, CH_4, CO_2, SF_6, $CFC-11$ and, $CFC-12$, during different seasons. The following aspects were of scientific interest during the SPURT campaigns:

- Spatial and temporal variability of the trace gas distribution in the UT/LS (e.g., Fischer et al., 2006; Hegglin et al., 2006; Krebsbach et al., 2006; Kunz et al., 2008).

- The role of processes (global, mesoscale and local) on the extent of the trace gas budgets in the LS, i.e., isentropic transport of trace gases across the tropopause, diabatic

descent of processed vortex air, existence of transport barriers (e.g., Hegglin et al., 2004, 2006).

- Coupling between the UT and the LS in seasonal and spatial dependence (e.g., Hoor et al., 2004; Krebsbach et al., 2006).
- Conditions and characteristics of mixing in the UT/LS (e.g., Kunz et al., 2009).
- Transport processes in the UT/LS identified from the trace gas variability in that region.

The goal of MOZAIC is to collect experimental data on the composition of the atmosphere up to cruising altitudes and to study the change of the atmosphere under the influence of human activity, with particular interest in the effects of aircraft. Regular measurements of O_3, H_2O, CO, and NO_y are made by autonomous instruments deployed aboard long range passenger aircraft. The large database of in–situ measurements collected in the course of MOZAIC allows detailed studies of chemical and physical processes in the atmosphere, and hence the validation of global chemistry transport models. This will also be valuable to improve the knowledge about the processes occurring in the UT/LS, and the model treatment of near tropopause chemistry and transport. The overall aims are the improvement of scientific knowledge regarding:

- The physical and chemical understanding of the atmosphere and thus an evaluation of the atmospheric impact of aircraft through validation of three–dimensional chemistry and transport models (e.g., Bousserez et al., 2007; Choi et al., 2008).
- The climatology and inter–annual variability of O_3 in the UT/LS (e.g. Thouret et al., 2006; Kunz et al., 2008).
- The distribution of H_2O in the UT and the quality of its representation by ECMWF analyses, on the ice super saturation phenomena, and on processes responsible for its distribution in the tropical UT (e.g., Luo et al., 2008).
- First large scale distributions of CO and NO_y in the UT/LS, including seasonality and vertical distribution at a quasi–global scale (e.g. Nedelec et al., 2005; Brioude et al., 2008; Choi et al., 2008).
- The impact of stratospheric intrusions on the composition of the troposphere and of vertical transport from the boundary layer on the chemical composition of the UT.
- Validation of the Chemistry Transport Models, which are the tools used for quantification of the UT/LS ozone budget, assessment of climate change and impact of aircraft,

and for providing answers to policy makers and industry (e.g. Bousserez et al., 2007; Søvde et al., 2008).

The Arctic troposphere is largely effected by aerosols due to radiation and transmission directly and indirectly via clouds. This motivates POLARCAT to study the transport of aerosols to the Arctic, as well as the air pollution from anthropogenic sources and boreal forest fires. The effects of this pollution on atmospheric chemistry and climate is of interest.
The POLARCAT international program includes measurements from aircraft, satellite and ground stations with the objective to quantify the import of trace gases and aerosols to the Arctic and their impact on atmospheric composition and climate. POLARCAT consists of different campaigns at different times of the year in order to follow pollution plumes of different origin as they are transported into the Arctic and observe the chemistry, aerosol processes, and radiation effects of these plumes. The first campaign took place in March–April 2007 in Longyearbyen (Spitsbergen). The last campaign was the POLARCAT–GRACE campaign in July 2008 based at Kangerlussuaq (Greenland). This airborne campaign was motivated to study various locations throughout the Arctic and the boreal region. Measurements of O_3, H_2O, CO, CO_2, NO, NO_2, NO_y, $J(NO_2)$, BrO, OClO, PFC, PAN, PPN and, MPAN were performed during this campaign. The following description bases on the flights performed during this campaign above Greenland. The scientific objectives of POLARCAT–GRACE are to get insight into:

- Annual variation of the distribution of trace gases and aerosols in the Arctic.
- Pathways and dispersion of boreal forest fire emissions at high latitudes.
- The role of mixing during long–range transport using ambient and artificial tracers.
- Processing (chemistry, aerosol aging) in pollution plumes for different sources (forest fires, urban pollution) and pathways.
- Effects of boreal forest fire emissions injected into the LS by pyro–convection.
- The distribution and impact of reactive halogen compounds in the Arctic.
- Validation of space–borne observations of trace gases and aerosol properties.

2.2 Geographical and vertical distribution

Within the SPURT project from November 2001 to July 2003, eight measurement campaigns were carried out using a Learjet 35 A with a ceiling altitude of 13 km as measurement platform. A typical campaign consisted of 2–3 consecutive mission days. The data set is based

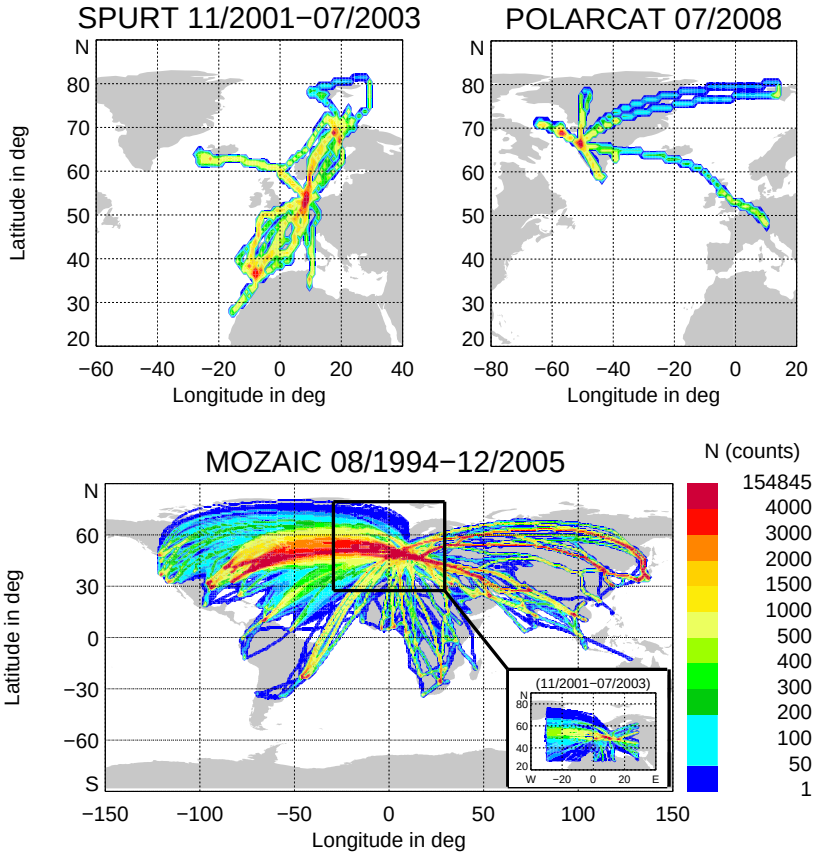

Figure 2.1: Geographical distribution of flights during SPURT (top left–hand panel), POLARCAT–GRACE (top right–hand panel) and MOZAIC (bottom panel). The frequency of 1 Hz (SPURT, POLARCAT) or 1–minute–averaged (MOZAIC) data points in each geographical 1° lat × 1° lon bin is color–coded. The area of SPURT flights is marked as black box in the MOZAIC plot and the frequency of MOZAIC flights in this European sector during 2001 and 2003 can be seen down right–hand.

on 36 flight missions and 147 flight hours. Each season during the SPURT period is captured by two measurement campaigns in subsequent years in order to investigate the seasonality of the trace gas concentrations (e.g., Krebsbach et al., 2006; Hoor et al., 2004; Hegglin et al., 2006). A description of the SPURT campaigns, the project strategy and performance is given in Engel et al. (2006). Figure 2.1 (top left–hand panel) shows the geographical distribution of the SPURT flights by means of the number of 1 s data points. The aircraft was based at the Hohn military base in northern Germany. Faro in southern Portugal was usually used for

refueling for southbound flights and Tromsø in Norway for northbound flights. Around the three stations the data density is very high because of slow ascents and descents.
The geographical distribution of MOZAIC measurements between 1994 and 2005 is displayed as one minute averages of the number of 5 s measurements in Figure 2.1 (bottom panel). MOZAIC flights cover all continents with the exception of Antarctica. The northern hemisphere is better covered than the southern hemisphere, with more than 40 % of MOZAIC flights in the North Atlantic flight corridor, more than 30 % in Asia and around 10 % of flights above Africa. Most of the measurements (90 %) correspond to cruise altitudes 9–12 km (Marenco et al., 1998), lying in the troposphere in the tropics and subtropics and in the UT/LS at mid latitudes. The European region of SPURT campaigns is highlighted as black box and the measurement frequency between 2001 and 2003 in this region can be seen in the right–hand bottom.
Figure 2.2 (left–hand panel) displays the vertical data coverage of SPURT and MOZAIC in Europe (see black box in Figure 2.1 bottom panel) in 5 K potential temperature bins in reference to the dynamical tropopause (2 PVU surface). The distance of the trace gas data from the dynamical tropopause ($\mathrm{DTP_{dyn}}$) is derived on the basis of potential vorticity and potential temperature, calculated from ECMWF output fields. The measurement frequency of MOZAIC in Europe (red line) peaks at a potential temperature of 330 K which corresponds to the vicinity of the tropopause. The maximum measurement frequencies of SPURT (black line) range between 335 K and 350 K, i.e., around 5 K below to 25 K above the tropopause. The average ceiling altitudes of the MOZAIC flights are lower and hence the maximum percentage of measurements appears at lower altitudes. More than 50 % of MOZAIC flights and more than 75 % of SPURT flights are performed in the lower stratosphere, so data should allow an investigation of trace gases in the tropopause region (Thouret et al., 2006; Law et al., 1998) and of exchange processes between the troposphere and the stratosphere.
The GRACE field deployment of the DLR Falcon research aircraft is a German contribution to the POLARCAT activity, a core project of the International Polar Year (IPY) in 2007 and 2008. The base of the Falcon operation during GRACE in July 2008 was Kangerlussuaq in Greenland. Within this campaign 20 different flights were performed from 01 July to 17 July 2008. Including the transfer flights from Oberpfaffenhofen the geographical distribution was between 50° N and 80° N (Figure 2.1, top right–hand panel). The main goal was to detect pollution plumes due to boreal fires. Thus the ceiling altitude was 12 km, which lies below those of the SPURT flights. Figure 2.2 (right–hand panel) shows the vertical percentage of POLARCAT measurements (cyan line) in comparison with the summer SPURT flights (black line) and the summer MOZAIC flights (red line) above the North–Atlantic flight corridor from 11/2001–07/2003. The picture relative to the dynamical tropopause (Figure 2.2, right–hand

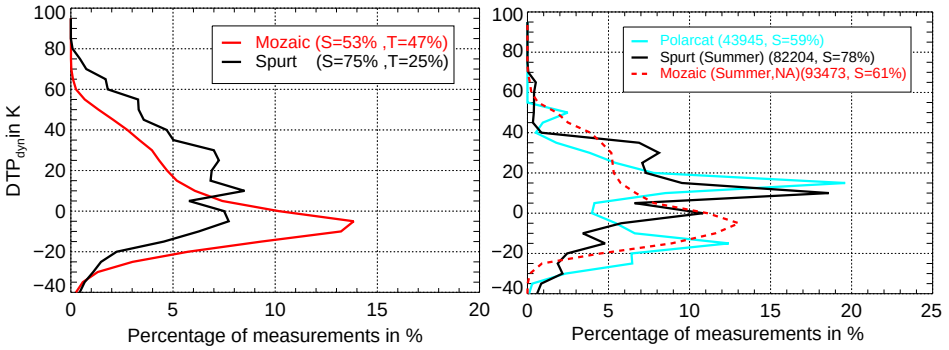

Figure 2.2: Left–hand panel: Vertical distribution of percentage of data points dependent on potential temperature in distance to the dynamical tropopause $\mathrm{DTP_{dyn}}$ during SPURT (black line) and MOZAIC in the European region (red line). Averages in 5 K bins are shown in reference to the tropopause (PV=2 PVU, $\mathrm{DTP_{dyn}}$=0 K). Right–hand panel: Vertical distribution of percentage of data points in $\mathrm{DTP_{dyn}}$ during POLARCAT–GRACE (solid cyan line). The summer MOZAIC data above the North–Atlantic flight corridor (dashed red line) and the summer SPURT data (solid black line) are additionally shown. The legend contains the percentage of data points in the stratosphere (S) and troposphere (T).

panel) reveals that the vertical percentage of POLARCAT measurements maximizes just above the tropopause with the similar distance to the tropopause ($\mathrm{DTP_{dyn}}$) as for SPURT, while most of the MOZAIC flights are just below the tropopause. But during POLARCAT most measurements were performed between 300 to 320 K, a potential temperature range below the main detected areas during SPURT (330 to 350 K) and MOZAIC (320 to 340 K) (not shown). Although the POLARCAT flights were performed in order to detect tropospheric plumes, the tropopause was in most cases low enough so that around 59% of flights were in the lower stratosphere.

2.3 Measurement systems

The measurement instruments of the trace gases O_3, H_2O and CO are described in the following. These are the trace gases which will be used for the analysis of the UT/LS with O_3 as stratospheric tracer and H_2O and CO as tropospheric tracers within this thesis.

2.3.1 O_3 measuring instruments

MOZAIC O_3 is measured with a modified commercial dual beam UV–absorption photometer (Thermo–Electron, Model 49-103). The measuring system and its performance are reported in detail by Thouret et al. (1998). The response time is better than 4 seconds with a detection

limit of about ± 2 ppbv. The overall uncertainty is estimated to be about $\pm$(2 ppbv + 2% of the observed reading). This corresponds to ± 2 ppbv for an O_3 mixing ratio of 10 ppbv, ± 4 ppbv for 100 ppbv, ± 6 ppbv for 200 ppbv (Thouret et al., 1998).
O_3 during SPURT was measured by UV absorption using the JOE (Jülich Ozone Experiment) instrument. The instrument is based on a Thermo Environmental Instrument ozonometer similar to that used for the MOZAIC program. The instrument was operated with a time resolution of 10 s and has an accuracy of 5% (Mottaghy, 2001). The MOZAIC and SPURT O_3 instruments are regularly calibrated in the Jülich laboratories against the same reference instrument. Similar to SPURT the O_3 mixing ratio during POLARCAT was also measured by a commercial UV–absorption photometer (Thermo–Environment, Model 49) (Brough et al., 2003). This analyzer has a range of 0–1000 ppbv and a detection limit of 1 ppbv. The major contributor to the uncertainty of the detector is the accuracy of the signal output of the instrument. As the accuracy of the signal output remains constant the uncertainty of the instrument increases with decreasing pressure in the absorption cell. The overall uncertainty of the O_3 analyzer was between 4% to 5%.

2.3.2 H_2O measuring instruments

During POLARCAT and SPURT H_2O mixing ratio was measured in–situ using the FISH (Fast In Situ Stratospheric Hygrometer) instrument (Zöger et al., 1999) which is based on the Lyman α photofragment fluorescence technique. The FISH instrument has a forward facing inlet and measures total water, i.e., the sum of the gaseous phase and the condensed phase. The response time is 1 s, which allows the detection of small–scale variations of H_2O mixing ratios in the vicinity of the tropopause, in clouds and contrails. The instruments accuracy is approximately 6 % and the detection limit is better than 0.2 ppmv.
On board of the five MOZAIC airbuses relative humidity with respect to liquid water (RH) is measured with compact airborne humidity sensing devices (Helten et al., 1998). The sensing element consists of a capacitive sensor (Humicap–H, Vaisala, Finland) with a hydro–active polymer film as dielectric material whose capacitance depends on the relative humidity, and a platinum resistance sensor (PT100) for direct measurement of temperature at the humidity sensor. The sensor mounted in an appropriate Rosemount housing is designed for measurement of gas–phase water which is calculated from the relative humidity measurement. Adiabatic compression leads to a temperature increase of the sampled air and thus to a reduction of the dynamic range of the sensor and to a sufficient time response at low static air temperatures. In the middle troposphere the overall uncertainty is within $\pm 4\%$ RH and around $\pm 7\%$ RH between 9 and 13 km. This implies a limited use of the MOZAIC H_2O sen-

sor in the stratosphere dominated by low RH and thus an increasing large uncertainty. The response time is around 10 s in the lower and middle troposphere and increases up to 1–3 min in the upper troposphere at 10–12 km altitude (Helten et al., 1998). After 500 operation hours the MOZAIC sensor is calibrated in the laboratory in Jülich. Recently, a new in–flight calibration (IFC) method for the MOZAIC sensor has been developed (Smit et al., 2008). The IFC method corrects the potential drift of the sensor offset at zero relative humidity, which is the critical parameter in determining the uncertainty of the measurements. The sensor offset is determined from the measurements themselves as obtained during flights in the lower stratosphere, where the H_2O values are very low at around 5 ppmv.
The characteristics of the different H_2O measuring instruments in MOZAIC and SPURT and the consequences on a common analysis of H_2O data of both instruments will be discussed in Chapter 3.

2.3.3 CO measuring instruments

During SPURT CO was measured with the Tunable Diode Laser Absorption Spectrometer (TDLAS) TRISTAR (Tracer in situ TDLAS for atmospheric research) (Wienhold et al., 1998). This instrument also measures CH_4 and N_2O and the time resolution is ultimately limited by the summed integration times for three measurement channels resulting in a duty cycle of less than 5 s for each species (Hoor et al., 2004). The instrument is calibrated in–flight using secondary standards of dried ambient air, whose concentrations are calibrated against a laboratory long–term standard, which is traced against NOAA standards to guarantee consistency over the different campaigns. The total uncertainty for CO is better than 1.5%.
CO during MOZAIC is measured by IR–Absorption (Nedelec et al., 2003). The MOZAIC CO analyzer is an improved version of a commercial Model 48CTL from Thermo Environmental Instruments, based on the Gas Filter Correlation principle of infrared absorption by the 4.67 μm fundamental vibration–rotation band of CO. The IR gas filter correlation (GFC) has the important advantage of long–term stability of the calibration factor, which obviates the need for an in situ calibration using compressed gas cylinders. This reduces the weight of the equipment, increases the time between services and leads to easier certification for commercial aircraft. The accuracy specification of the commercial instrument is 10 ppbv CO for 300 s integration time. CO was measured by VUV fluorescence during POLARCAT (Brough et al., 2003). A detailed description of the CO instrument can be found in Gerbig et al. (1999). This DLR CO instrument has a linear response from 0 to 1000 ppmv and has a time resolution of 1 s. Following the analysis of Gerbig et al. (1999) the instruments detection limit is smaller than 6 ppbv and the precision is 1.5 ppbv.

Chapter 3

Statistical analysis of H_2O and O_3 in the UT/LS

The crucial question of this chapter is on the representativeness of data sets with different sampling strategies and instrumentation. The motivation of the SPURT campaigns was the climatological investigation of the UT/LS, i.e., the seasonal variability of trace gases in this region (Engel et al., 2006). To proof this, the comparability of trace gas mixing ratios observed during the limited number of flights in SPURT with those of the climatological data set obtained during the frequent MOZAIC flights is investigated. A statistical analysis of H_2O and O_3 follows to show in an objective manner the strengths and weaknesses of the two data sets.
Both data sets are statistically analyzed in order to assess the comparability of H_2O and O_3 data in SPURT and MOZAIC. For this purpose, the main focus is set on the following questions:

- Do the data sets with different coverage in space (region and altitude), time and with different instrument characteristics represent the same population in the atmospheric system?

- Are the SPURT campaigns, with around eight flight missions in each season, as representative as the MOZAIC daily flights? Are the SPURT data really suited for a climatological investigation on a seasonal and annual time scale and do they represent the full atmospheric variability of trace gases in the UT/LS?

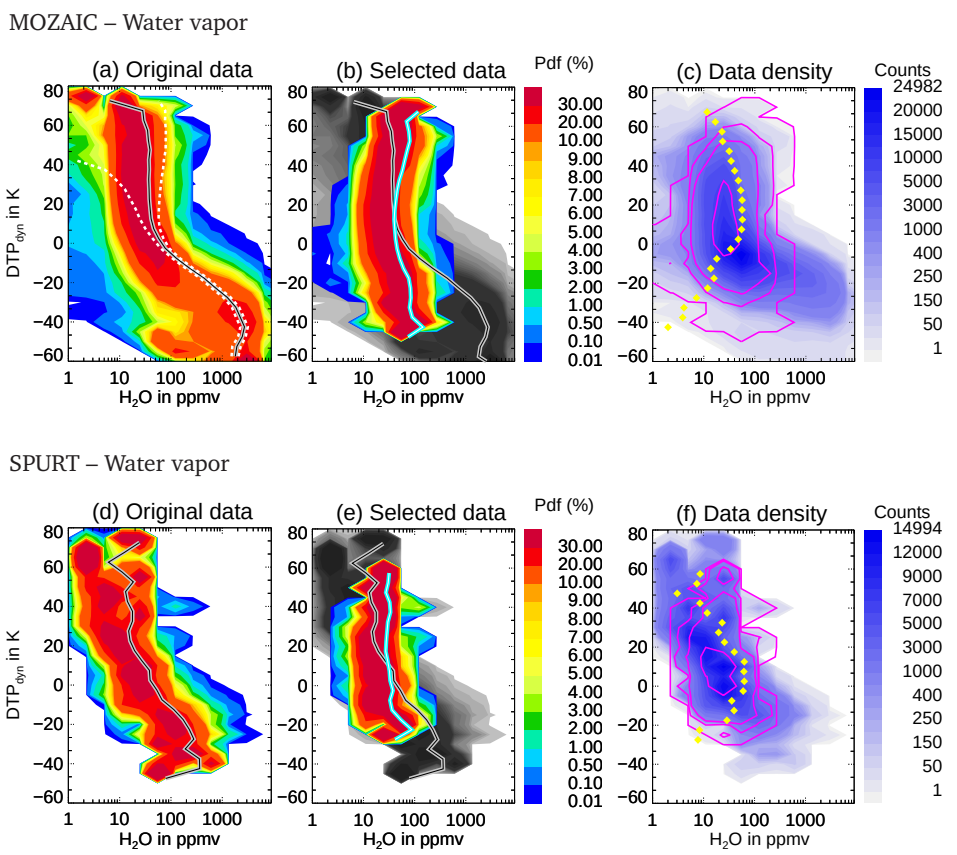

Figure 3.1: Probability distribution functions of MOZAIC (top panels) and SPURT (bottom panels) H_2O mixing ratio related to the distance to the local dynamical tropopause DTP_{dyn} in K, defined by the 2 PVU surface. H_2O is binned in the logarithmical space between 0 and 9.6 with a bin size of 0.8, the distance to local tropopause in 5 K bins. **Left–hand panels**: PDF of original H_2O data. The mean vertical profile (solid gray–black line) and the uncertainty of 5 % RH (dashed white lines) are shown for the MOZAIC PDF. SPURT accuracy of H_2O data is 6 % of concentration (not shown). **Middle panels**: The distribution of the original data (panels (a) and (d)) is shaded and that of the selected H_2O data is color coded. The mean PDFs are also shown as black–gray line (original data) and blue–white line (selected data). **Right–hand panels**: Number of original data points per bin (blue shaded) and of selected data (non filled pink contours 0, 100, 500, 5000 data per DTP_{dyn} bin). The fraction of selected data relative to the original number in each DTP_{dyn} bin in percent is shown as yellow diamonds for all DTP_{dyn} bins with more than 1 % of the total data.

3.1 Probability distribution and selection of data

The following statistical analysis is performed for MOZAIC data observed in the same geographical region where the SPURT campaigns were carried out and for the same period from

MOZAIC – Ozone

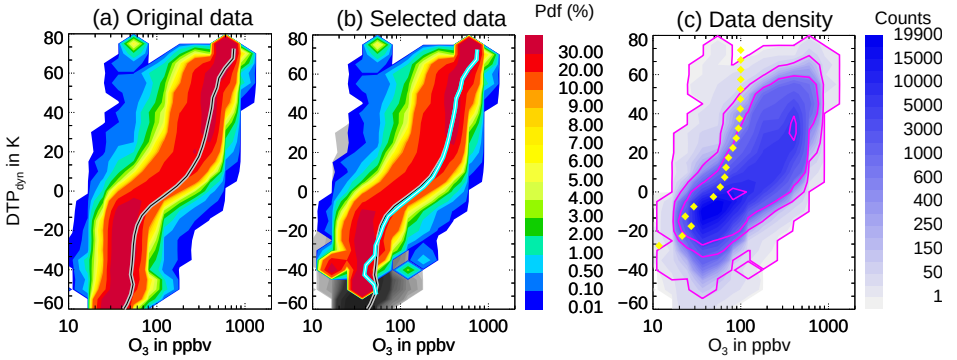

SPURT – Ozone

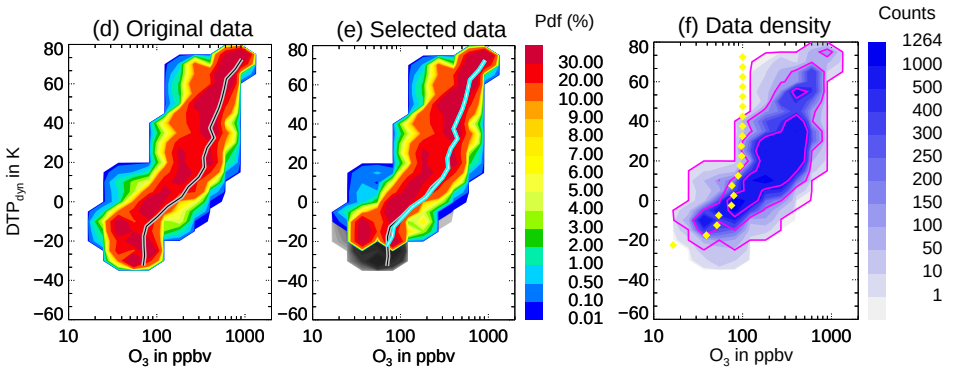

Figure 3.2: Probability distribution functions of MOZAIC (top panels) and SPURT (bottom panels) as in Figure 3.1, but now for O_3 mixing ratios related to the 2 PVU tropopause. The bin size for O_3 is 0.4 in the logarithmical space between 0 and 7.6, the bin size for $\mathrm{DTP_{dyn}}$ is again 5 K. With a very high accuracy of 5 % the original trace gas distributions do not contain any accuracy limits. The right–hand panels show the fraction of selected data relative to the original number in each $\mathrm{DTP_{dyn}}$ bin with more than 10 % data as yellow diamonds.

November 2001 to July 2003 (black box in Figure 2.1 bottom panel). The MOZAIC and SPURT data sets are split according to the distance to the local tropopause (2 PVU surface):

- *Upper troposphere (UT):* $\mathrm{DTP_{dyn}} < -5\mathrm{K}$
- *Lower stratosphere (LS):* $\mathrm{DTP_{dyn}} > 5\mathrm{K}$

This approach should account for different sampling strategies and different trace gas characteristics. Influences by the large trace gas gradients in the vicinity of the tropopause ($-5\,\mathrm{K} <$

$DTP_{dyn} < 5\,K$) are excluded.

Figure 3.1 shows the probability distribution functions (PDF) of H_2O data and Figure 3.2 those of O_3 data dependent on the distance to the dynamical tropopause for MOZAIC and SPURT (panels (a) and (d), respectively). The trace gas frequencies are calculated in 5 K bins relative to the tropopause.

However, these probability distributions of H_2O reveal some differences between SPURT and MOZAIC. A very high probability of SPURT H_2O values lower than 10 ppmv occurs in the stratosphere more than 20 K above the tropopause (panel (d)). There is only a very low probability of H_2O data in the respective mixing ratio bins in MOZAIC (panel (a)). In the stratosphere, the maximum MOZAIC H_2O probability corresponds to considerably higher H_2O values than in the case of SPURT. There are no SPURT H_2O values larger than 2000 ppmv in the troposphere more than 45 K below the tropopause, where the MOZAIC H_2O data density is still quite high (see density plots, panels (c) and (f) of Figure 3.1). This is due to the different measurement characteristics, while MOZAIC data are sampled from the ground, SPURT data are sampled above the 400 hPa level. Hence MOZAIC has a higher mean PDF (solid gray–black line) corresponding to a higher mean vertical H_2O profile both in the troposphere and in the stratosphere than SPURT. The MOZAIC mean H_2O profile remains nearly constant around 40 ppmv in the stratosphere more than 5 K above the tropopause, whereas the SPURT mean H_2O profile decreases from 40 ppmv at the tropopause to mixing ratios lower than 10 ppmv around 60 K above the tropopause. Hereby, the 5 % uncertainty of the MOZAIC sensor in the UT/LS must be accounted for. The uncertainties of ± 5 % relative humidity with respect to liquid water are shown as dashed white lines in panel (a). The uncertainty range in volume mixing ratio scale is expanded in the entire stratosphere, attaining even negative values 40 K above the tropopause. The 5 % RH uncertainty leads to a decreasing precision of H_2O volume mixing ratio deeper in the stratosphere. The SPURT H_2O data with a high relative accuracy of 6 % of H_2O concentration do not reveal this problem and the mean vertical mixing ratio also decreases in the stratosphere. A corresponding dashed white line is not shown in the SPURT PDF because of the small amount around the mean vertical profile.

The O_3 MOZAIC data set is stronger influenced by low mixing ratios than the SPURT data set (see panels (a) and (d) of Figure 3.2). There is a very high probability of MOZAIC O_3 data in the troposphere below -35 K, where the SPURT data do not contain any O_3 mixing ratios. In the UT/LS above -35 K the mean vertical O_3 profiles (gray–black lines) of SPURT and MOZAIC are very similar and the mixing ratio at the tropopause is around 150 ppbv in both cases.

Differences between both data sets, in particular in the H_2O distributions, basically result

from different instrumental characteristics or measurement strategies. Because of the different H_2O measurement techniques (see Section 2.3.2), the H_2O data have to be modified before a statistical comparison using the following selection criteria:

- The MOZAIC Humicap sensor has a precision of 4–7 % RH, i.e., low H_2O mixing ratios are not detected and cannot be contained in the PDFs of Figure 3.1. Thus the dry measurements according to $RH < 10$ % in particular in the stratosphere, where SPURT was focused on, cannot be included in the comparison due to sensitivity limitations of the MOZAIC sensor at low RH.

- The FISH instrument has a foreward facing inlet and measures total water, i.e., both the gas phase and the condensed phase H_2O mixing ratios. The MOZAIC Humicap sensor measures relative humidity with respect to liquid water and the mixing ratios represent only the gas phase. Therefore, only data with a relative humidity with respect to ice $RH_{ice} \leq 100\,\%$ should be compared in order to eliminate measurements in clouds and under supersaturation conditions.

- H_2O mixing ratios larger than 500 ppmv are sorted out, because the FISH instrument is calibrated for mixing ratios below this limit. At larger mixing ratios the measurement cell of FISH becomes optically dense and the FISH fluorescence method is limited on in–situ measurements above a mixing ratio of 500 ppmv. To select only data representative for the UT/LS the 250 hPa pressure level is chosen as lower limit.

- In the UT/LS the MOZAIC sensor has a response time of $\tau \approx 60\,\mathrm{s}$ and the FISH instrument of $\tau \approx 1\,\mathrm{s}$. Therefore, a running mean with a time interval of 60 seconds is applied on the SPURT data for this study.

These selection criteria are applied on the MOZAIC and SPURT H_2O data. The third criterion with a data selection above the 250 hPa pressure level is also applied on the O_3 data in order to compensate for the tropospheric bias of the complete MOZAIC data set.
Panels (b) and (e) in Figure 3.1 and Figure 3.2 show H_2O and O_3 PDFs modified according to the selection criteria (color coded) and the original PDFs, also shown in panels (a) and (d), as shaded area. The mean vertical profile of the selected H_2O data set (blue line) is shifted toward larger values in the stratosphere and toward lower values in the troposphere for both MOZAIC and SPURT. As a consequence of the criterion to select data with relative humidities above $RH > 10\,\%$, H_2O mixing ratios below 10 ppmv are excluded. The most probable H_2O data in the stratosphere are now between 10 and 30 ppmv both in SPURT and MOZAIC. In the troposphere the data are removed because of the 500 ppmv, the 250 hPa and

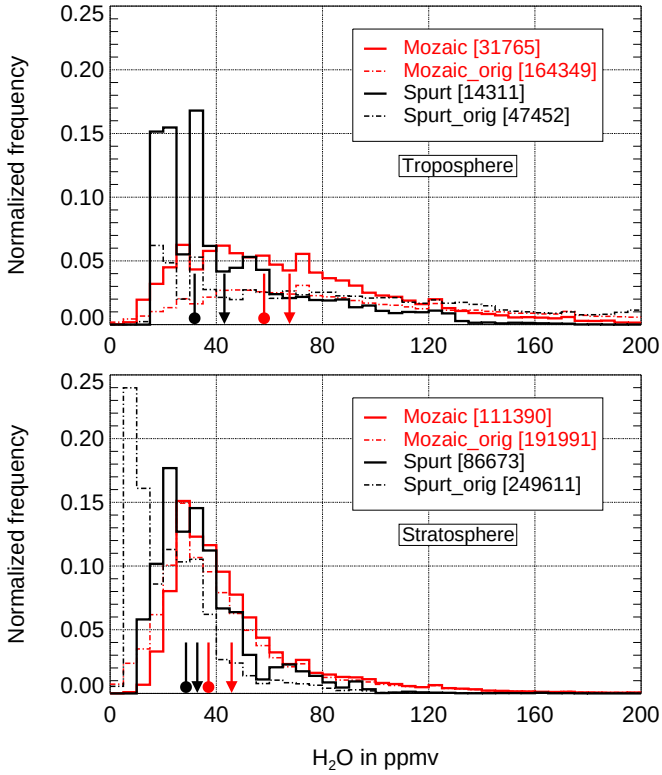

Figure 3.3: Frequency distribution of H_2O mixing ratio in the troposphere ($DTP_{dyn} < -5K$, top panel) and in the stratosphere ($DTP_{dyn} > 5K$, bottom panel). The bin size for H_2O is 5 ppmv and the bin frequencies are normalized by the total number of data points (see legend). The frequency distributions of the data selected by the instrument criteria (see text) are shown by the solid lines, those of the original data by the dashed lines. The means of the selected MOZAIC and SPURT data are marked by the triangle symbols, the medians by circle symbols. In the case of unselected data they are beyond the range of the ordinate.

the $RH_{ice} \leq 100\,\%$ criteria. The 250 hPa criterion excludes most O_3 data in the troposphere. This has the largest impact on the MOZAIC data set.

Figure 3.3 shows the normalized frequency distributions of H_2O and Figure 3.4 shows those of O_3 mixing ratios of MOZAIC (red) and SPURT (black). These distributions further illustrate a better agreement for both trace gases when the data selection is applied (solid lines = selected data; dashed lines = original data). But there are still some differences left as e.g., a high normalized H_2O frequency in SPURT at lower mixing ratios in the troposphere. A difference in sample means and medians also remains (triangles and dots in Figures 3.3 and 3.4, respectively). The mean O_3 mixing ratios are larger in SPURT than in MOZAIC and

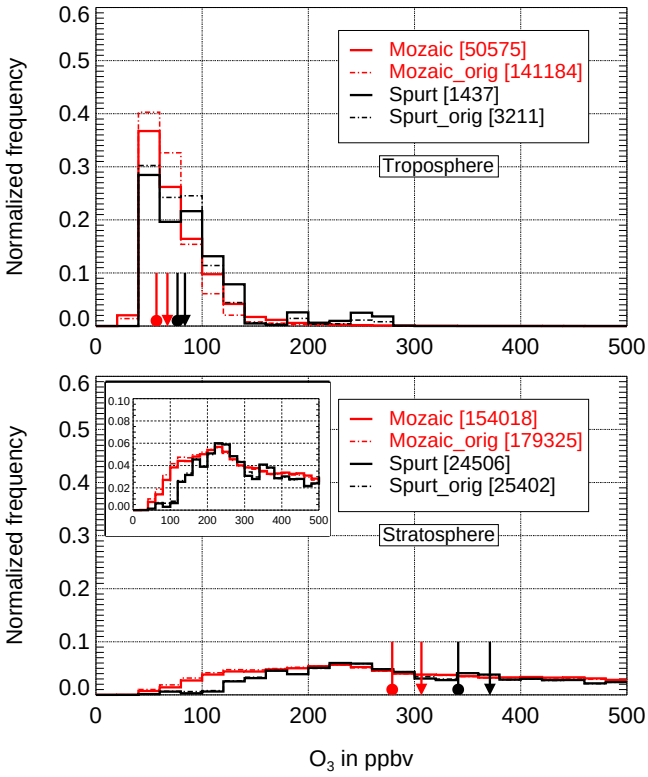

Figure 3.4: Frequency distribution of O_3 mixing ratio in the troposphere ($DTP_{dyn} < -5$K, top panel) and in the stratosphere ($DTP_{dyn} > 5$K, bottom panel). The bin size of O_3 is 10 ppbv.

vice versa for H_2O, thus still reflecting the different vertical sampling range of both projects. The broadness of the SPURT and MOZAIC H_2O distribution after the selection is very similar especially in the stratosphere. The number of data points (legends of Figures 3.3 and 3.4) demonstrates a reduction by around 65 % of H_2O due to data selection both for SPURT and MOZAIC, around 12 % of O_3 data points are rejected for SPURT and around 45 % of O_3 data points for MOZAIC.

The data selection is essential to achieve a sufficient agreement of the frequency distribution functions for both trace gases and projects (see Figures 3.3 and 3.4) with some differences left to allow for a statistical comparison of both data sets. For the following statistical analysis, the reduced data sets of H_2O and O_3 in which differences due to the different H_2O measurement techniques and sampling strategies are eliminated as far as possible, will be used.

3.2 Kolmogoroff–Smirnoff test

The Kolmogoroff–Smirnoff goodness–of–fit test compares two independent random samples of measured data and examines whether they stem from the same population (Brandt, 1999; Sachs and Hedderich, 2006). Compared to other goodness–of–fit tests, e.g., the χ^2–test, the Kolmogoroff–Smirnoff test can be applied to non-normally distributed data. The test is well suited to investigate if both random samples belong to the same population. The central tendency of the variance, the skewness and kurtosis, i.e., differences of the type of distribution and thus of the distribution functions in Figures 3.3 and 3.4 are captured.

3.2.1 Mathematical description

The test statistic is the maximum observed difference of the ordinate between the two non overlapping cumulative frequency curves. Both statistical samples, i.e., the MOZAIC and SPURT data, are binned in an equal number of classes. The empirical cumulative distribution functions $\hat{\mathrm{F}}_{\mathrm{spurt}}$ and $\hat{\mathrm{F}}_{\mathrm{mozaic}}$ and their differences $\hat{\mathrm{F}}_{\mathrm{spurt}} - \hat{\mathrm{F}}_{\mathrm{mozaic}}$ are calculated. The test statistic $\hat{\mathrm{D}}$ is the maximum of the absolute value of this difference, i.e.,

$$\hat{\mathrm{D}} = \max \left| \left(\hat{\mathrm{F}}_{\mathrm{spurt}} - \hat{\mathrm{F}}_{\mathrm{mozaic}} \right) \right| . \tag{3.1}$$

For large sample sizes ($\mathrm{n}_{\mathrm{spurt}} + \mathrm{n}_{\mathrm{mozaic}} > 35$) the cutoff value D_α can be approximated by

$$\mathrm{D}_\alpha = \mathrm{K}_\alpha \cdot \sqrt{\frac{\mathrm{n}_{\mathrm{spurt}} + \mathrm{n}_{\mathrm{mozaic}}}{\mathrm{n}_{\mathrm{spurt}} \cdot \mathrm{n}_{\mathrm{mozaic}}}} , \tag{3.2}$$

with $\mathrm{n}_{\mathrm{spurt}}$ and $\mathrm{n}_{\mathrm{mozaic}}$ the number of elements of the two statistical samples and K_α the Kolmogoroff–Smirnoff constant dependent on the confidence α. Table 3.1 contains the corresponding values of K_α.

Table 3.1: Selected constants K_α dependent on different confidences α for the Kolmogoroff–Smirnoff test (Sachs and Hedderich, 2006)

α	0.80	0.85	0.90	0.95	0.99	0.999
K_α	1.07	1.14	1.22	1.36	1.63	1.95

If the test statistic $\hat{\mathrm{D}}$, calculated from both samples, is greater or equal to the cutoff value D_α, both distribution functions are significantly different with a selected error probability or confidence.

Table 3.2: Kolmogoroff–Smirnoff test statistics $\hat{D}$ and cutoff values D_α (rounded for four decimal places) for two different confidences $\alpha = 95\,\%$ and $\alpha = 99.9\,\%$

	$\hat{D}(H_2O)$	$D^{H_2O}_{\alpha=95\,\%}$	$D^{H_2O}_{\alpha=99.9\,\%}$	$\hat{D}(O_3)$	$D^{O_3}_{\alpha=95\,\%}$	$D^{O_3}_{\alpha=99.9\,\%}$
Troposphere	0.3691	0.0137	0.0164	0.1757	0.0308	0.0369
Stratosphere	0.2503	0.0061	0.0074	0.1403	0.0090	0.0107

3.2.2 Test performance

The null–hypothesis H_0 'Both distribution functions of trace gases H_2O and O_3 in MOZAIC and SPURT are the same' is tested against the alternative hypothesis H_A 'Both distribution functions are different from each other' with a confidence of $\alpha = 95\,\%$. The larger the test statistic $\hat{D}$ in equation 3.1, the more the null–hypothesis has to be rejected.

Table 3.2 shows the values of the test statistic $\hat{D}$ and the corresponding cutoff values D_α calculated both for data within the troposphere ($DTP_{dyn} < -5K$) and the stratosphere ($DTP_{dyn} > 5K$). The test statistic $\hat{D}$ in table 3.2 is much larger than the cutoff value D_α for all cases. The null hypothesis of equal distribution functions for both the H_2O and the O_3 mixing ratio can be rejected with a confidence of $\alpha = 95\,\%$. The tests are also performed for different confidences varying between $\alpha = 95\,\%$ and $\alpha = 99.9\,\%$ (see also table 3.2) with the same test results. Therefore, with high confidence the H_2O and O_3 mixing ratios of the MOZAIC and SPURT data sets differ from each other.

A graphical display of the Kolmogoroff–Smirnoff test results gives a so–called probability network (see Figure 3.5). The H_2O and O_3 cumulative frequency functions $\hat{F}_{spurt}$ and $\hat{F}_{mozaic}$ are plotted logarithmically in this probability network for troposphere (top panels) and stratosphere (bottom panels). The corresponding cutoff value D_α is plotted as confidence region for each distribution function (dotted lines). If the null hypothesis H_0 of equal distribution functions was not rejected, the frequency function of $\hat{F}_{mozaic}$ lies within the confidence limit of the other distribution function $\hat{F}_{spurt}$ and vice versa. Note the distorted ordinate according to the χ^2–distribution function, which causes the different range of confidence limits although the Kolmogoroff–Smirnoff constant is equal in the entire mixing ratio range of the abscissa. The corresponding cutoff values and test statistics can be found in table 3.2. The test results in table 3.2 are reflected well in these figures. In each case a region is found, where both cumulative frequency functions differ significantly from each other, i.e., where the difference between both functions is largest. The maximum difference in ordinate, corresponding to the test statistic $\hat{D}$, is always located at the middle range of mixing ratios (see dashed cyan line in Figure 3.5). The two tested cumulative distribution functions do not generally lie in the confidence limit of the other one, thus both statistical data samples are different from each

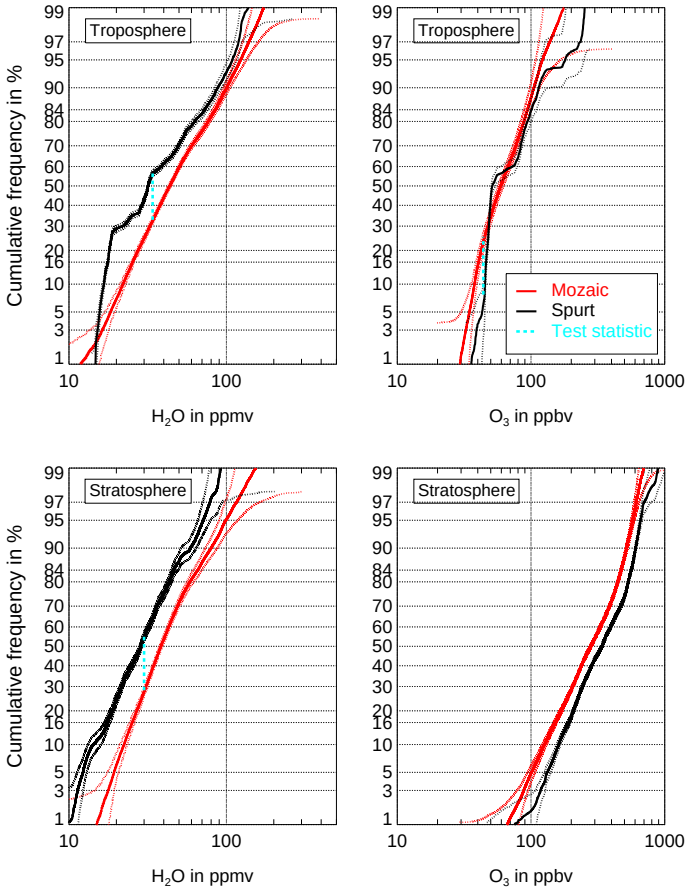

Figure 3.5: Probability networks with empirical cumulative frequency functions in % of H_2O and O_3 mixing ratios in MOZAIC (red) and SPURT (black). Top panels: Troposphere ($DTP_{dyn} < -5K$). Bottom panels: stratosphere ($DTP_{dyn} > 5K$). The cutoff value D_α is displayed as $\alpha = 95\,\%$ confidence region for each frequency function (dotted line) and the corresponding test statistic $\hat{D}$ (dashed cyan line) is also shown.

other and do not belong to the same population.

Although the O_3 cumulative distribution functions are very close to each other for each atmospheric region a small area is found where the test statistic becomes larger than the cutoff value and thus a statistical difference between both distribution functions results.

A difference between the cumulative distribution functions both for O_3 data based on the same measurement techniques and for H_2O data using different measurement techniques is evident. The H_2O cumulative distribution function for MOZAIC is larger than that for SPURT

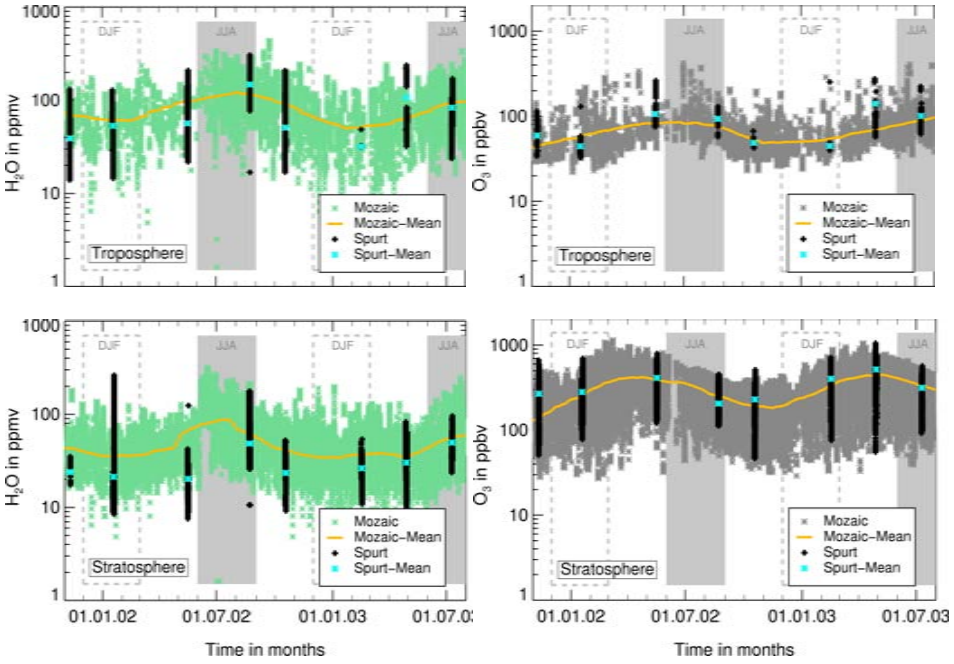

Figure 3.6: Time series of H_2O (left–hand panels) and O_3 (right–hand panels) in the troposphere ($DTP_{dyn} < -5\,K$) (top panels) and stratosphere ($DTP_{dyn} > 5\,K$) (bottom panels) between 11/2001 and 07/2003. MOZAIC measurements are gray for O_3 and green for H_2O. SPURT measurements are black. The mean MOZAIC mixing ratio is orange and the mean SPURT mixing ratio is blue, respectively.

both in the UT and LS, and vice versa for O_3. There are still different sample means with higher SPURT H_2O means and lower O_3 means than in MOZAIC. This indicates that there are other, most likely sampling or regional causes for the differences between the trace gas data in SPURT and MOZAIC. Especially in the stratosphere this must be due to the different campaign performance, with the Learjet in SPURT flying deeper into the stratosphere and thus sampling on average a higher O_3 and lower H_2O mixing ratio (see Figure 2.2).

3.3 Variance analysis

Here, the selected data samples are examined for their variability characteristics. A typical SPURT campaign consisted of four flights, with a flight time of around four hours each. One season is covered by eight single flights with H_2O data. Thus these few days represent a whole season in this data set. Figure 3.6 shows the different temporal variability of the SPURT measurements (black symbols) in comparison to the MOZAIC measurements (colored

symbols). MOZAIC provides at least two flights with H_2O data (green symbols) for each day. The O_3 measurements (gray color) are shown in a similar way. Although both data sets, i.e., SPURT and MOZAIC, reveal a seasonal cycle in the troposphere (top panels) and stratosphere (bottom panels), they are expected to vary on different time scales.
The term time scale in this context is more a matter of speech. Since the movement of the aircrafts is fast compared to the wind speed the onboard sensors encounter the spacial gradients at short time scales and the temporal gradients at long time scales. Since both aircrafts are moving with approximately the same speed the interaction of spatial and temporal gradients is comparable on lower time scales around 4 hours, when the spatial and temporal variability play comparable roles. The concept of a temporal statistical variance analysis is an appropriate tool to investigate trace gas variability and provides information about atmospheric and even chemical influences (Rohrer and Berresheim, 2006).

3.3.1 Test description

For a variance analysis the H_2O and O_3 data sets in MOZAIC and SPURT (Figure 3.6) are binned into series of time intervals of different lengths, i.e., time scales, from several minutes to years. A mean variance is calculated for each time scale. When dividing a data set of a time scale of one year into two half year data sets, a variance is calculated of the data within the half year bins. Both resulting sample variances are averaged and the mean variance for the data set about a half year results. Then the one year data set is divided into three four month data sets, the procedure is repeated and the mean variance about a three month bin is calculated. This successive subsampling of the data is done 100 times toward lower bin sizes.

3.3.2 Analysis applied on a joint flight of FISH and MOZAIC sensor

Before doing the variance analysis on the complete SPURT and MOZAIC data of Section 3.2, the analysis is applied on the water vapor data observed during one single flight of the CIRRUS III campaign (Figure 3.7, top panel). The motivation of the three CIRRUS campaigns between 2002 and 2006 was to investigate the formation mechanism of cirrus clouds, their radiative effects and to study the chemical or microphysical properties of the cloud particles. Both the FISH instrument and the MOZAIC sensor, already described in Section 2.3.2, were onboard the Learjet 35 A during the last CIRRUS III campaign in November 2006. The CIRRUS III midlatitude cirrus field experiment took place at the Hohn military base. Six flights mainly inside and outside frontal cirrus clouds were performed in the altitude range from $7 - 12\,\mathrm{km}$ between $45 - 70°\,\mathrm{N}$.
An inflight comparison of both instruments can be performed which shows the results of a

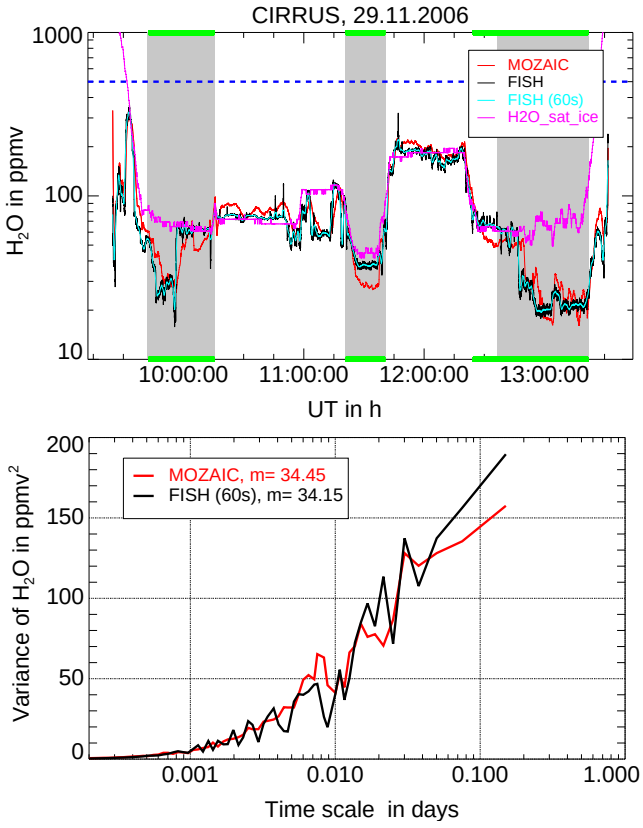

Figure 3.7: Top panel: In–flight comparison of FISH (black) and MOZAIC sensor (red) H_2O mixing ratio during the CIRRUS III flight on 29 November 2006. The 60 s running mean of the FISH H_2O mixing ratio is highlighted in cyan and the saturation H_2O mixing ratio in pink. The part of the flight, which is performed above the 250 hPa pressure level is bounded by the green line. After all selection criteria are applied, data above the gray shaded area are used for the variance analysis. Bottom panel: Variance analysis of FISH (black) and the MOZAIC sensor (red) H_2O mixing ratio during the CIRRUS III flight.

variance analysis, if the data are sampled under the same spatial and temporal conditions. This is a good opportunity to study the importance of interaction between temporal and spatial variances on small time scales during an in–flight comparison. The selection criteria are also applied on this data set and for the resulting data (gray shaded area in Figure 3.7, top panel) the variance analysis reveals a really good agreement between the H_2O variances as observed by FISH (black) and MOZAIC H_2O (red) sensor (Figure 3.7, bottom panel). A similar increasing variance on a time scale of 3.5 hours demonstrates that both instruments

detected the same atmospheric processes and that there is no discrepancy due to the unequal measurement instruments left.

3.3.3 Analysis on MOZAIC and SPURT flights

Figure 3.8 shows the variance analysis of MOZAIC and SPURT H_2O and Figure 3.9 the variance analysis of O_3 data for the troposphere (top panel) and the stratosphere (bottom panel). The variance of H_2O in MOZAIC increases from short to long time scales within the troposphere (red line, Figure 3.8, top panel). There are four consecutive time scale regions, representing a different strength and change of atmospheric H_2O variability. An increasing variance on time scales of one hour to one or two days, representing the H_2O variability on a diurnal time scale. Further an enhancement on a typical synoptic ten–day time scale and on an inter–seasonal time scale between 10 and 90 days is observed. On both time scales the variance enhancement is not as sharp as on the diurnal time scale. At least there is an extreme increase of variance of H_2O data on the 90 to 300 days time scale, representing a seasonal variability of H_2O mixing ratio in MOZAIC.
The tropospheric H_2O variance in SPURT (black line, Figure 3.8, top panel) coincides with that of MOZAIC on a time scale of 0.15 days, i.e., around four hours. This variance represents the temporal and the spatial variance. The typical duration of a SPURT flight or the duration of the MOZAIC flights within Europe is around four hours. The aircrafts velocity of both projects is nearly the same and both measurement systems are comparable on a short time scale of some hours as shown in Figure 3.7. There is still a good agreement on a time scale of 1 day, but on longer time scales both variances diverge more and more resulting in a much lower variance of H_2O in SPURT than in MOZAIC. An increasing variance of SPURT H_2O can be observed on a three day time scale, the typical time scale of the mission days during each aircraft campaign. On longer periods until 90 days the variance remains approximately constant, fluctuating around a statistical mean on a three to ten day time scale. This fluctuation reduces on longer time scales. On a seasonal time scale a variance of SPURT H_2O data is observed.
When dividing the SPURT data set into different time series of non–regular time scales, most of the bins do not contain measurement data. On an inter–seasonal time scale there are SPURT data available on two or three consecutive days (see also 3.6 black symbols). As a consequence when calculating the variance on a 100 day time scale the variance will remain constant until reaching the prescribed bin, which contains the measurement data. This bin includes a time scale of one or two days. As consequence no H_2O variability is found on an inter–seasonal time scale in SPURT. The variance on a seasonal time scale is based on single

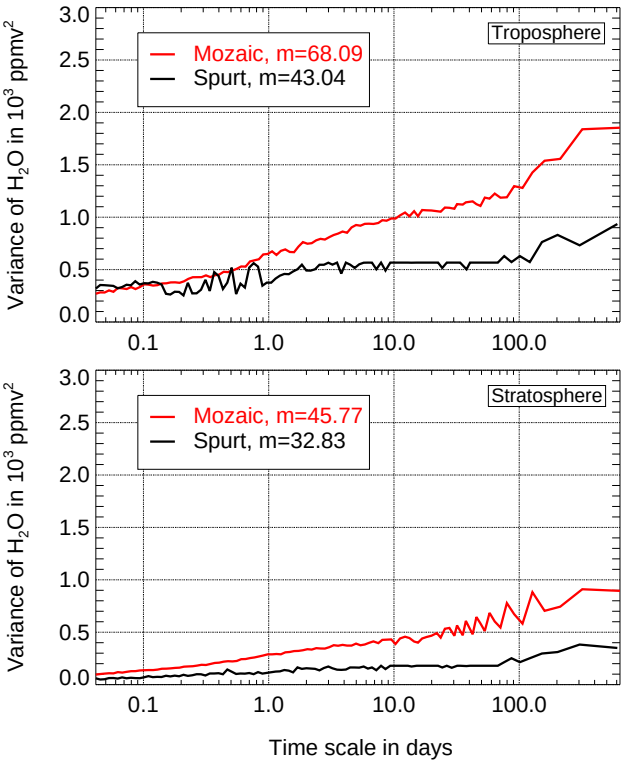

Figure 3.8: Variance analysis of H_2O in ppmv^2 of MOZAIC (red) and SPURT (black). Top panel: troposphere ($\mathrm{DTP}_{\mathrm{dyn}} < -5\mathrm{K}$). Bottom panel: stratosphere ($\mathrm{DTP}_{\mathrm{dyn}} > 5\mathrm{K}$).

flights on two or three consecutive days each season during the two years.

The H_2O variances are lower within the stratosphere for each time scale (Figure 3.8, bottom panel), representing the smaller H_2O variability in the upper atmosphere. The difference of the variance between MOZAIC and SPURT reduces in the stratosphere, but a discrepancy remains.

For SPURT, the stratospheric tracer O_3 reveals an enhancing variance on a ten–day time scale as for MOZAIC (see Figure 3.9). There is no enhancement of SPURT O_3 variance on an inter–seasonal time scale until 90 days, but for MOZAIC the O_3 variance increases only marginally. On a seasonal time scale until 300 days there is an increasing variance both for SPURT and MOZAIC O_3. Compared to the troposphere the O_3 variance increases in the stratosphere. The slope of the O_3 variance of SPURT is similar to that of MOZAIC and there is no considerable difference between SPURT and MOZAIC O_3 variance as observed for the tropospheric tracer H_2O.

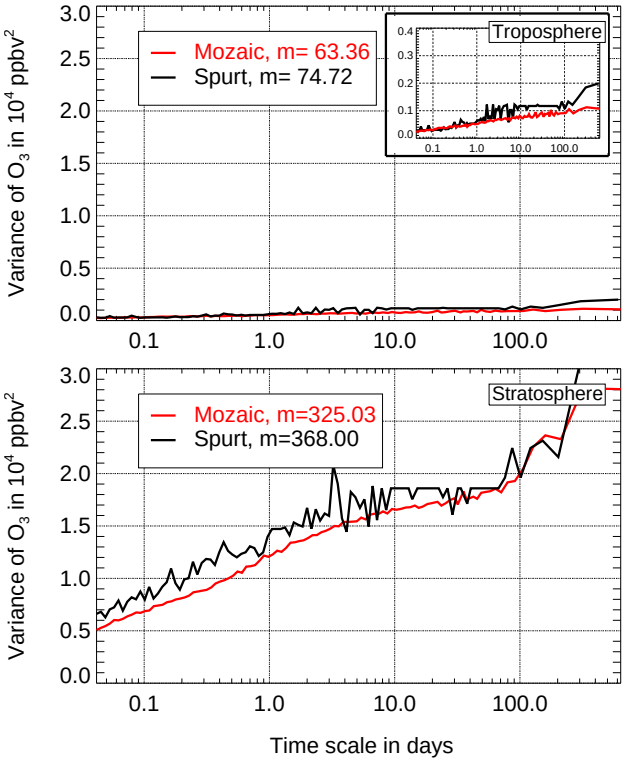

Figure 3.9: Variance analysis of O_3 in ppbv^2 of MOZAIC (red) and SPURT (black). Top panel: troposphere ($\mathrm{DTP_{dyn}} < -5$K). Bottom panel: stratosphere ($\mathrm{DTP_{dyn}} > 5$K). The tropospheric variance of MOZAIC O_3 is additionally shown enlarged top right–hand.

3.3.4 Discussion on variability of SPURT and MOZAIC data

The H_2O data observed during the SPURT campaigns contain atmospheric processes, which take place on a diurnal time scale. There is a fluctuating variance between several minutes up to two to three days. The SPURT data set does not contain information about any processes on longer inter–seasonal time scales, but on a seasonal time scale between 90 and 300 days. Thus SPURT contains on the one hand processes playing a role on the typical campaign time scale (one to three days). Further the seasonal variability is based on the equally time–spaced performed campaigns, while each season is covered by two campaigns. Thus the trace gas variability within a season (10 to 90 days) is not included which is about 50 % of the total variance of H_2O.

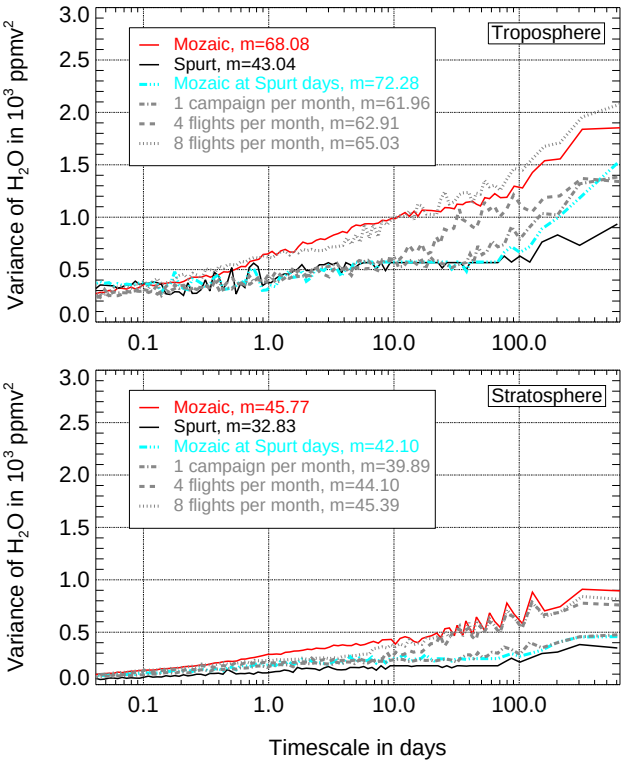

Figure 3.10: Variance analysis of H_2O subsamples from the MOZAIC data set in the troposphere (top panel) and stratosphere (bottom panel). The H_2O variances of the SPURT (black) and full MOZAIC data (red) from Figure 3.8 are additionally shown with the variance of MOZAIC data sampled on the same SPURT flight days (cyan). Further variances are calculated corresponding to one campaign per month (dashed–dotted), i.e., flights on two consecutive days each month between November 2001 and July 2003. Four flight days per month (dashed), i.e., flights on every sixth day. Eight flight days according to flights every fourth day (dotted).

The MOZAIC H_2O measurements are influenced by synoptic scale processes on a ten–day time scale and by processes on an inter–seasonal time scale. The variance enhancing on a ten–day time scale represents a variability which is typical for synoptic weather systems influencing the air mass composition in a specific region as low or high pressure systems. Further there is a variance between 10 and 90 days, representing processes varying on an inter–seasonal time scale up to three months and a variability on a seasonal time scale. Contrary to SPURT the MOZAIC data set gives information about processes on each time scale. Especially MOZAIC contains information about processes which are representative for the

different seasons. The SPURT H_2O variance is not representative for the seasonal time scale and rather gives an instantaneous picture of the atmosphere on the single flight days. SPURT is rather dominated by short scale fluctuating processes. These different processes in both data sets are the reason for differences in the frequency distribution functions (Figures 3.3 and 3.4).

On long time scales the H_2O variances of MOZAIC and SPURT differ more and more due to the different measurement frequency. The difference is largest in the troposphere, the full atmospheric H_2O variance in the UT is not captured by the SPURT campaigns. Large scale atmospheric processes and turbulent systems playing a role in the UT on a longer than diurnal time scale and influencing the variability of the tropospheric tracer H_2O are not contained in the SPURT data and account for this difference. The H_2O difference in variance lessens in the stratosphere, but still remains.

The stratospheric tracer O_3 does not reveal the differences in variance in SPURT and MOZAIC as observed for H_2O. SPURT O_3 data represent the atmospheric processes influencing the O_3 distribution in the UT/LS on each time scale despite the inter–seasonal time scale between 10 and 90 days as expected. But the full atmospheric O_3 variance as MOZAIC shows is achieved in the UT/LS on every time scale thus demonstrating that contrary to the tropospheric tracer H_2O the amount of SPURT data is sufficient to represent the full O_3 variability even on seasonal time scales. This demonstrates the different variability behavior of the stratospheric tracer O_3, which has a typical photochemical life time of several months and longer in the LS (Sankey and Shepherd, 2003). O_3 is independent of short scale fluctuating processes and definitely acts on longer time scales than H_2O.

Figure 3.10 shows the variance analysis for different subsamples of MOZAIC data in the troposphere (top panel) and in the stratosphere (bottom panel). The variance of the full MOZAIC H_2O data between November 2001 and July 2003 (red line) is compared with that of the MOZAIC data on the single SPURT mission days (cyan line), which has a very similar shape as that of SPURT H_2O (black line). The difference to the variance of the full MOZAIC data (red) reduces marginally on the time scale between 40 to 300 days in the troposphere and between 40 to 150 days in the stratosphere, if there would be one campaign each month (dashed–dotted line). To capture the full atmospheric H_2O variance as MOZAIC shows there have to be every fourth day measurement flights in the troposphere (dotted line), while in the stratosphere measurements every sixth day are sufficient especially on inter–seasonal and seasonal time scales (dashed line). That means that the research aircraft would have to fly on around eight days per month in the troposphere and around four days per month in the stratosphere to capture the full climatological variability of MOZAIC H_2O.

3.4 Results of this chapter

The statistical analysis shows that the SPURT data set, despite its much larger temporal and spatial coverage as compared to other campaigns with research aircraft, does not represent the full variability of atmospheric H_2O in the tropopause region as observed during MOZAIC and can only be used for limited climatological investigations. The limited number of SPURT flights cannot replace the large number of MOZAIC flights when analyzing the H_2O distribution in a climatological manner. The SPURT observations rather give an instantaneous picture of one day variability especially of the upper tropospheric H_2O mixing ratio. Information about large scale processes varying on a seasonal time scale are less representative, as a variance analysis reveals. For O_3 the number of SPURT flights is almost sufficient. SPURT delivers the atmospheric variability of O_3 on each time scale except of the inter–seasonal one, which however is weak as the MOZAIC data show. Therefore, SPURT O_3 can be used even for climatological investigations.

This result suggests an oversampling of MOZAIC O_3 data within the UT/LS, a regular sampling from season to season seems sufficient to represent the climatological behavior of O_3 in the UT/LS. The MOZAIC trace gas data are not limited in the variance characteristics. These data represent atmospheric processes varying on longer time scales like synoptic weather systems. They are ideal for seasonal and annual investigations of H_2O and O_3 mixing ratios. However, the statistical comparison reveals the known limitation of the MOZAIC RH sensor in the LS. Small scale fluctuations in the UT/LS cannot be observed by this capacitive sensor, while the FISH instrument in SPURT is well suited for studies with attention to fast processes in the UT/LS, as mixing and transport processes.

Chapter 4

An observational analysis of the Tropopause Inversion Layer

One feature coupled with the UT/LS, which has gained an increasing importance in the last years, is the so–called tropopause inversion layer (TIL) above the extratropical tropopause in the lowermost stratosphere (Birner et al., 2002). The TIL is characterized by an inversion in the temperature profile and by an enhanced static stability (buoyancy frequency squared, N^2) compared to the troposphere and the entire stratosphere. Tracer correlations between a stratospheric (O_3) and a tropospheric tracer (CO) reveal an extratropical mixing layer in the lowermost stratosphere (Fischer et al., 2000; Hoor et al., 2002). The gradient of these trace gases is enhanced within the mixing layer. There is a large seasonal variability of exchange across the tropopause which influences the thickness of the mixing layer. Both the strength of the TIL and the thickness of the mixing layer have a large winter to summer contrast (Hoor et al., 2002; Birner, 2006). Further the UT/LS is a region where the atmospheric radiative balance is very sensitive to changes in trace gases such as H_2O or O_3 (Forster, 1999; Forster and Shine, 2002). The height of the tropopause, which is related to the TIL and the mixing layer, is also very sensible to the upper tropospheric flow. It has been shown that anticyclonic balanced disturbances lead to a higher and sharper tropopause with an enhanced N^2 just above the tropopause. Contrary, cyclonic balanced dynamics lead to a lower and less sharp tropopause with reduced N^2 above the tropopause (Wirth, 2003).

Several hypotheses on the maintenance of the TIL, i.e., the upper tropospheric dynamics, mixing of trace gases and also radiative forcing, have been proposed so far. Due to mixing the trace gas gradients are changed in the LS, which may influence the temperature gradient and thus the static stability N^2 in the TIL. Randel et al. (2007b) suggested that the radiative effects of both O_3 and H_2O near the tropopause may be a substantial contribution to the formation and the maintenance of the TIL. They further postulated that the vertical

scale of the TIL is partly linked to the thickness of the mixing layer. Birner (2006) argued that the TIL could be the result of poleward heat fluxes together with extratropical baroclinic eddies. These eddies act on the background temperature gradient in the tropopause region. Balanced dynamics studies by Wirth (2003) revealed enhanced N^2 in the LS as a feature of anticyclonic upper–tropospheric flow. A dynamical mechanism was proposed by Wirth (2004) that the asymmetry between upper–level cyclones and anticyclones and their effects on the local stratification around the tropopause is responsible for the existence of the TIL in the climatological mean (see also Wirth and Szabo, 2007). Hereby, the convergence and divergence of the vertical wind may affect the vertical separation of the isentropes and thus can modify the static stability above the tropopause and the TIL. Randel et al. (2007b) showed that the TIL is evident both for anticyclonic and cyclonic upper tropospheric flow. Recently, Hegglin et al. (2009) delivered further observational support for the mechanism proposed by Randel et al. (2007b) and emphasized the relevance of H_2O for maintaining the TIL. The seasonal changes of H_2O satellite data and their relative vertical gradient are similar to the N^2 structure within the TIL.

Based on in situ observations and radiative calculations, this thesis further investigates the possible maintenance processes of the TIL. Using the observations obtained during the SPURT aircraft campaigns and the data from ECMWF output fields, the following questions are of interest:

- Is there any link between the extratropical mixing layer and the TIL? To quantify the relationship between the static stability N^2 and the mixing degree a measure of the mixing degree will be introduced.
- Does the TIL also exist in an atmosphere with a non–mixed state? To investigate this question, the impact of a 'L–shaped' tracer correlation between a tropospheric (H_2O) and a stratospheric tracer (O_3) on the thermal stratification is analyzed with a radiative transport model.
- Which upper tropospheric flow is related to the TIL? An analysis of the relative vorticity field in the upper troposphere associated with the TIL regions will be performed.

4.1 Static stability and Tropopause Inversion Layer (TIL)

In a stably stratified atmosphere the Brunt–Väisälä frequency is defined as the frequency N of an oscillating air parcel if it was displaced vertically without disturbing its environment (Holton, 2004). A measure for the static stability of the environment is the Brunt–Väisälä frequency squared, i.e.

$$N^2 = \frac{g}{\theta}\frac{\partial\theta}{\partial z} \tag{4.1}$$

with g the gravitational acceleration and θ the potential temperature. If $N^2 < 0$, i.e., the potential temperature is decreasing with height, the displacement will increase exponentially with time and the stratification will be statically unstable. In the atmosphere convective systems are statically unstable. If $N^2 = 0$, an accelerating force does not exist and the air parcel is in neutral equilibrium. If $N^2 > 0$, i.e., the potential temperature increases with height, the parcel will oscillate about its initial level. The stratification will be statically stable. With the help of the ideal gas equation $p = \rho RT$ and the definition of the potential temperature $\theta = T\left(\frac{p_0}{p}\right)^{\frac{R}{c_p}}$, the Brunt–Väisälä frequency is also given by

$$N^2 = \frac{g}{T}\left(\frac{\partial T}{\partial z} + \frac{g}{c_p}\right). \tag{4.2}$$

The pressure is denoted by p, the reference pressure is p_0, the specific heat at constant pressure is c_p and the universal gas constant is R. In the following, the Brunt–Väisälä frequency N^2 squared is referred to as static stability.

The zonal and time mean static stability N^2 in $10^{-4}\,\mathrm{s}^{-2}$ is shown in Figure 4.1 for summer (top panel) and winter (bottom panel). N^2 is calculated from ECMWF data at the 18 single SPURT flight days between 2001 and 2003. The T511L61 operational ECMWF data (Simmons et al., 2005) are used. The data are interpolated on a $1^\circ \times 1^\circ$ horizontal grid and to 35 vertical pressure levels (19 equidistant levels between $1000\,\mathrm{hPa}$ and $100\,\mathrm{hPa}$). The time mean is calculated for 12 UTC ECMWF data.

Within the well mixed troposphere the zonal and time mean static stability is very low around $N^2 = 1 - 2 \cdot 10^{-4}\,\mathrm{s}^{-2}$. Characteristic for the winter pole is an intensive inversion at the bottom due to the missing solar radiation. During polar night the surface and the air masses above the surface cool out. As consequence the static stability near the surface is enhanced and an intensive temperature inversion results in the lower troposphere. This can be partly seen at the south pole during winter (JJA) at 4 km (Figure 4.1, top panel). The inversion near the surface at the north pole during winter (DJF) is below 4 km, but this is obscured in Figure 4.1 (top panel) due to the y–axis limits.

The largest gradient in static stability is within the tropopause region around the thermal tropopause (white line). The entire lower stratosphere is stably stratified and the static stability is higher than in the troposphere with values around $N^2 = 4 - 5 \cdot 10^{-4}\,\mathrm{s}^{-2}$. The transition between the troposphere to stratosphere related to a high gradient of static stability is largest in the tropics and the midlatitudes. The slope of the isentropes (pink contours) is also largest across the tropopause. Especially the middle world isentropes are characterized

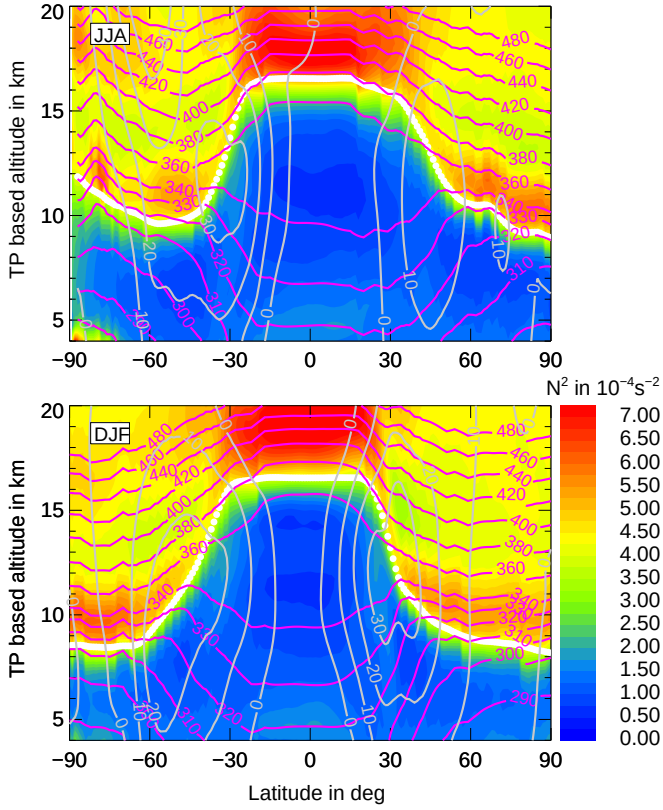

Figure 4.1: Static stability N^2 in $10^{-4}\,\mathrm{s}^{-2}$ calculated with ECMWF operational fields for summer (top panel) and winter (bottom panel). The thermal tropopause is given by the solid white line, the isentropic surfaces as pink isolines and the isotaches as gray isolines.

by a positive slope within the troposphere and by a negative slope within the stratosphere. Near the winter polar regions these isentropes are enhancing again, which is related to the presence of a polar vortex. This feature is most evident during the winter at the south pole, demonstrating a more stable vortex at the south pole than at the north pole.

The highest static stability $N^2 > 5 \cdot 10^{-4}\,\mathrm{s}^{-2}$ is located above the tropical tropopause and in a layer above the extratropical tropopause. This layer is the so–called tropopause inversion layer (TIL). The vertical temperature gradient exhibits a strong inversion within this layer with the temperature strongly increasing above a sharp thermal tropopause (Birner et al., 2002). As consequence of the sharp maximum in temperature the N^2 is maximized within the TIL, i.e., N^2 is enhanced compared to values of N^2 in the entire stratosphere. This layer

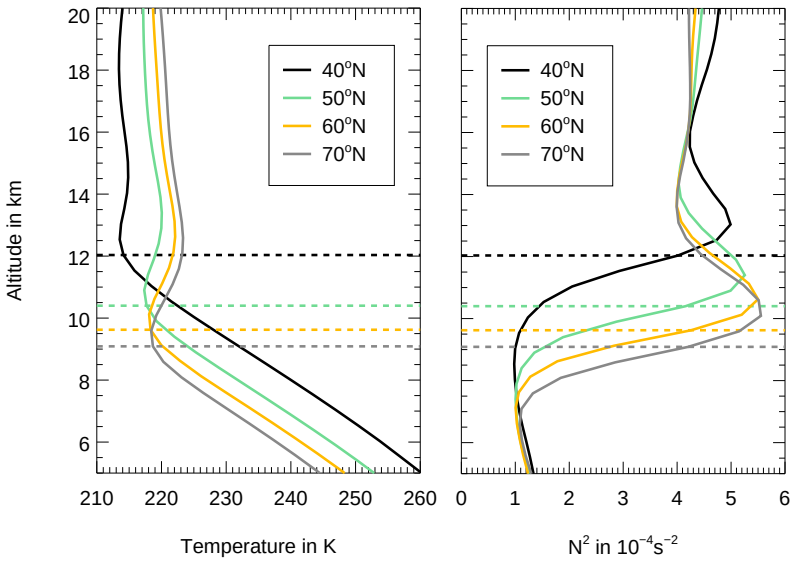

Figure 4.2: ECMWF zonal and time mean vertical profiles of the temperature (left–hand panel) and the static stability (right–hand panel) between 40° N (black line) and 70° N (gray line). The thermal tropopause at the different latitudes is given by the horizontal dashed line.

with enhanced N^2 roughly contains the stratospheric part of the middle world isentropes between the thermal tropopause and the 380 K isentrope, i.e., within the lowermost stratosphere. There is a large winter to summer contrast with a more intensive TIL in the summer hemisphere than in the winter hemisphere. During the winter the TIL has a greater vertical and meridional extension than during the summer. Especially in the winter hemisphere there is a layer of lower static stability $N^2 \approx 3 \cdot 10^{-4}\,\mathrm{s}^{-2}$ above the TIL in the subtropics related to the upper part of the subtropical jet stream (gray contours). This layer may be due to secondary thermal tropopauses with tropical characteristics. Pan et al. (2009b) already discussed deep intrusions of tropospheric air into the lower stratosphere above the subtropical jet stream, which are characterized by low static stability and which occur along and under the poleward extending tropical tropopause.

Figure 4.2 shows four different ECMWF zonal and time mean vertical profiles of the temperature (left–hand panel) and the static stability (right–hand panel) between 40° N (black line) and 70° N (gray line). The profiles represent the zonal and time mean of the ECMWF data at the 18 SPURT flight days. Above the thermal tropopause (horizontal dashed lines) there is a sharp positive temperature gradient within the TIL. This temperature inversion is dependent on latitude, i.e., the inversion is more intensive toward higher latitudes. At the same time

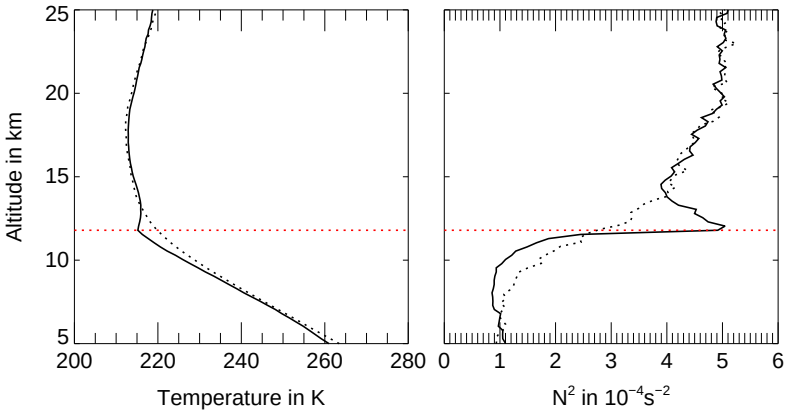

Figure 4.3: Time mean temperature in K and static stability in $10^{-4}\,\mathrm{s}^{-2}$ from the Boulder balloon data from 1980–2007. The mean height of the thermal tropopause is $z_{TP_{th}} = 11.79\,\mathrm{km}$ (dashed red line). Dashed black lines represent the conventional sea level based mean, solid lines the corresponding tropopause based mean.

there is a sharp maximum in static stability above the thermal tropopause. This maximum is more intensive at $70^\circ\,\mathrm{N}$ than at $40^\circ\,\mathrm{N}$. The static stability above the sharp maximum declines with height. The existence and sharpness of the peak in N^2 above the tropopause is often referred to as a measure for the sharpness of the tropopause (e.g., Wirth and Szabo, 2007). The sharpness of the tropopause is also analyzed by Pan et al. (2004) with the help of correlations between a stratospheric and a tropospheric tracer. They analyzed the nature of the connection between the two branches, stratosphere and troposphere, in a correlation plot, which provides information on the characteristics of the transition and thus on the sharpness of the tropopause.

To obtain the fine–scale climatological structure of the tropopause region, e.g., the characteristic feature of the TIL with the sharp maximum in N^2 above the thermal tropopause, the zonal and time mean have to be calculated relative to the tropopause as described by Birner et al. (2002) and Birner (2006). For this purpose, the thermal tropopause $\mathrm{TP_{th}}$ has to be computed first for each vertical profile. The vertical profiles of a quantity $x(t,z)$ are interpolated on equidistant spaces with respect to the local time–dependent height of the tropopause $z_{TP_{th}}$, using the tropopause as reference level. A cubic spline interpolation is performed to receive equally spaced levels. Therefore, a 500 m distance is used for the ECMWF data in Figures 4.1 and 4.2. Thus, the difference between the height of each level with the height of the tropopause, i.e., $z - z_{TP_{th}}$, is computed. Then the tropopause based parameter are averaged in a zonal and time mean to receive a tropopause based average $\overline{x(t, z - z_{TP_{th}})}$ of

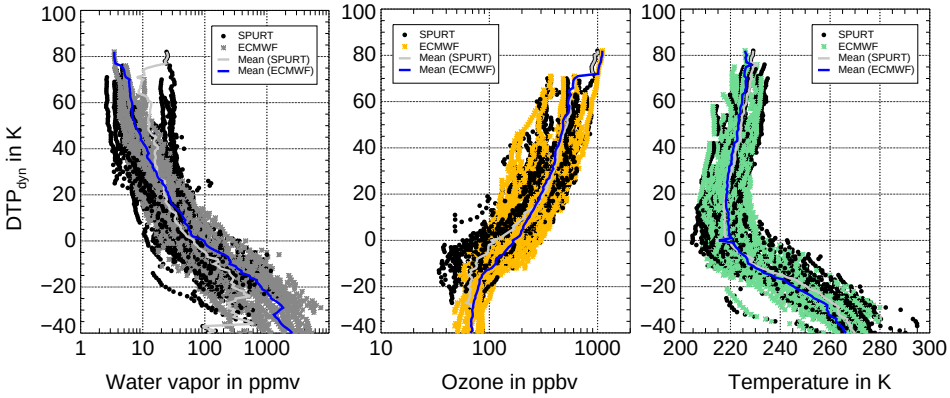

Figure 4.4: Vertical profiles of water vapor (left–hand panel), ozone (middle panel) and temperature (right–hand panel) relative to the dynamical tropopause in $\mathrm{DTP_{dyn}}$ in K of all SPURT data (black dots) and the interpolated ECMWF data (colored crosses). The mean vertical profiles for SPURT data (solid gray lines) and of ECMWF data (solid blue lines) are shown.

the quantity x. The vertical coordinate in a sea level based manner can be readjusted by the time–averaged height of the tropopause $\overline{z_{TP_{th}}}$, i.e., $z_{readj} = \overline{z - z_{TP_{th}}} + \overline{z_{TP_{th}}}$. This averaging procedure was performed to receive the fine–scale structure of the TIL in Figures 4.1 and 4.2. Despite this tropopause based averaging, the transition across the thermal tropopause from the upper troposphere to the lower stratosphere is very smooth in the ECMWF vertical profiles (Figure 4.2). The reason is the vertical resolution of the ECMWF data. The vertical resolution of $\Delta \mathrm{z} \sim 0.8 - 1.4\,\mathrm{km}$ around the extratropical tropopause and the horizontal resolution of $1^\circ \times 1^\circ$ are sufficient to resolve a well–pronounced TIL in the time and zonal mean. But similar to other model results in Birner et al. (2006), who used data from the NCEP/NCAR reanalysis and the Canadian Middle Atmosphere Model CMAM, the TIL is not as sharp as for data sets with a higher resolution.

Figure 4.3 shows the tropopause based time mean (solid line) of the temperature (left–hand panel) and the static stability (right–hand panel) for vertical sonde profiles taken at $40^\circ\,\mathrm{N}$ and $105.25^\circ\,\mathrm{W}$ in Boulder, Colorado, between 1980 and 2007. These sonde data with a high resolution of 250 m also in the tropopause region represent a sharp tropopause transition in the temperature and static stability distribution. There is a sharp maximum of the static stability above the thermal tropopause. Note that a conventional sea level based averaging of the profiles (dashed lines, respectively) results in a blurred structure at the tropopause. The temperature inversion and the sharp maximum in static stability are not resolved. In this sea level based averaging the vertical coordinate is fixed in time and horizontal space.

Any feature strongly variable in space and time, e.g., the height of the tropopause, is blurred in the resulting sea level based climatology. Therefore, in a climatology of the tropopause region and thus of the static stability and the temperature within that region the tropopause based averaging is advantageous compared to the conventional sea level based averaging.

4.2 High static stability in the extratropical mixing layer

The high static stability within the TIL is roughly in that part of the extratropical tropopause region where the mixing layer is observed. This mixing layer has different chemical characteristics than the entire stratosphere or the entire troposphere. Therefore, a possible link between mixing and the TIL in the extratropics is investigated in the following. For this purpose the observational CO and O_3 data from the eight SPURT aircraft campaigns over Europe between 2001 and 2003 (Engel et al., 2006) are analyzed. The obtained data sets represent the UT/LS up to $13.5\,\mathrm{km}$ and a high frequency of flights were above the tropopause (Figure 2.2). This analysis comprises 34 SPURT flights with sufficient data in the vicinity of the tropopause. The static stability calculated from ECMWF data is interpolated on the flight path. This is done both spatially, i.e., in the horizontal and vertical space, and temporally. First the respective positions of the SPURT flight paths at noon time (12 UTC) are determined by trajectory calculations with CLaMS (Chemical Lagrangian Model of the Stratosphere, McKenna et al. (2002b); Konopka et al. (2007)). Then the spatial interpolation is done.

Figure 4.4 shows vertical profiles of the ECMWF data at the SPURT flight paths together with the SPURT measurements for H_2O (left–hand panel), O_3 (middle panel) and temperature (right–hand panel). A good agreement of the mean vertical profiles of SPURT (solid gray lines) and ECMWF (solid blue lines) is shown. The temperature field consistent between ECMWF and SPURT, O_3 is consistent in the stratosphere with a slight difference in the upper troposphere. H_2O shows a good agreement in the tropopause region, with a higher mixing ratio of ECMWF than SPURT in the troposphere and vice versa in the stratosphere. Shifts in space or time of modeled data compared to reality can appear in the vicinity of strong dynamical activities as the jet streams. These discrepancies are not evident in the used ECMWF data in the vicinity of the SPURT measurements.

4.2.1 SPURT case study

Figure 4.5 panel (a) shows the tracer correlation of O_3 and CO observed during the SPURT flight on 27 April 2003. The air with $CO < 34\,\mathrm{ppbv}$ is defined as stratospheric (pink) and the

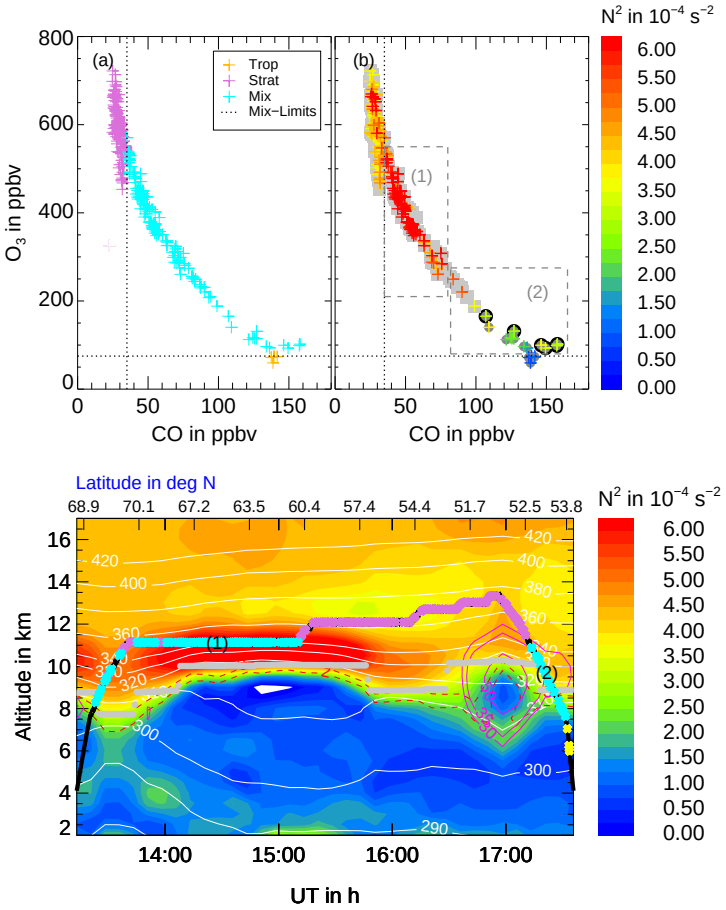

Figure 4.5: SPURT flight on 27 April 2003 from Kiruna ($68°\mathrm{N}$, $21°\mathrm{E}$) toward Hohn ($54°\mathrm{N}$, $9°\mathrm{E}$). **Top panels**: O_3 and CO correlation colored according to the stratosphere (pink), troposphere (yellow) and mixed branch (cyan) in panel (a) and according to N^2 in panel (b). Measurements above the thermal tropopause are marked by light gray squares, those below by dark gray circles, which are additionally bordered in black if they are above the dynamical tropopause ($2\,\mathrm{PVU}$). **Bottom panel**: Vertical cross section of N^2 along the flight path (black), colored according to the three branches in panel (a). The mixed parts (cyan) at the beginning and end of the flight path are numbered and marked in panel (b) as gray dashed boxes. Isotaches in $\mathrm{m\,s^{-1}}$ (red), 2 and 3 PVU isolines (red dashed), isentropes in K (white) and the thermal tropopause (gray) are shown.

air with $O_3 < 75\,\mathrm{ppbv}$ as tropospheric (yellow). These thresholds for O_3 and CO are arbitrary and different in literature. Here, similar values to Pan et al. (2006) are used, who select the data within the mixing layer according to $CO < 30\,\mathrm{ppbv}$ and $O_3 < 50\,\mathrm{ppbv}$. The results of this analysis are not sensitive to the used thresholds. All other air masses are considered to

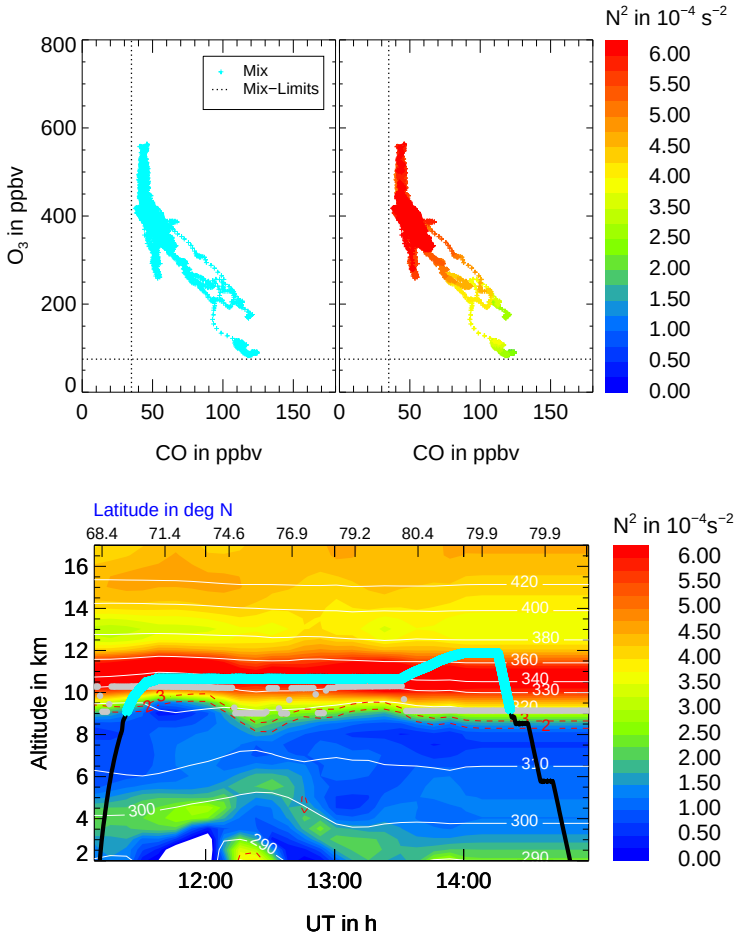

Figure 4.6: POLARCAT flight on 15 July 2008 from Kangerlussuaq toward Spitsbergen. See Figure 4.5 for figure description.

be mixed (cyan). The highest values of static stability ($N^2 \approx 7 \cdot 10^{-4}\,\mathrm{s}^{-2}$) can be found in the middle and upper part of the mixed branch (box 1, Figure 4.5 (b)). The lowest values ($N^2 \approx 1 \cdot 10^{-4}\,\mathrm{s}^{-2}$) are found in the troposphere and intermediate values ($N^2 \approx 4 \cdot 10^{-4}\,\mathrm{s}^{-2}$) in the stratosphere. Thus, the mixing layer contains a significant amount of high stability air. The vertical cross section of N^2 along the flight path (bottom panel) shows that these mixed air masses (cyan flight segment) with high N^2 (deep red filled contours) were detected immediately after entering the stratosphere at the beginning of the flight. During this flight segment the TIL was sampled (denoted (1), see also panel (b)). Thereafter, stratospheric air masses with lower N^2 were observed (pink flight segment) before again entering into a

mixed air mass in the vicinity of the polar jet stream (red contours) with a higher N^2 than in the entire troposphere and a lower N^2 than in the TIL. Box 2 shows the corresponding part in panel (b).

The mixed branch in the vicinity of the jet stream is likely the result of recent quasi–isentropic mixing of trace gases from the troposphere to the stratosphere. Mean age of air calculations with CLaMS reveal that these mixed air masses close to the jet stream are younger than the mixed air masses in the TIL (not shown). The younger air masses are partly below the thermal tropopause (dark gray circles, panel (b)). The older air masses within the TIL are above the tropopause (light gray squares, panel (b)) and far away from the jet stream.

The high static stability related to the TIL within the mixing layer is also evident in case studies of flights during the POLARCAT–GRACE campaign above the polar region. Figure 4.6 shows one of these POLARCAT–GRACE flights on 15 July 2008 from Kangerlussuaq (Greenland) toward Lonyearbyen (Spitsbergen). The TIL was detected during most of the POLARCAT–GRACE flights. Thus POLARCAT–GRACE also gives a picture of the TIL and the mixing layer during the polar summer. The mixing layer is also associated with a very high static stability above the polar regions. The flight introduced in Figure 4.6 would originally contain some tropospheric values with $\mathrm{O_3} < 75\,\mathrm{ppbv}$. But due to the calculation of trajectories to noon time data are missed when backward trajectories intersect the surface before 12 UTC.

4.2.2 Tropospheric Fresh Mixing (TFM branch)

The low values of static stability in the lower branch of the mixing layer during the flight on 27 April 2003 (Figure 4.5) were observed in the vicinity of the subtropical jet stream, i.e, on the cyclonic side of the jet stream in the LS. The jet streams are generally characterized by a break in the thermal tropopause together with a distortion of the dynamical tropopause. This dynamical situation is associated with a fast quasi–isentropic exchange of trace gases between the troposphere and the stratosphere.

The exact position of the measurements associated with a low static stability (Figure 4.5, box 2 in panel(b)) relative to the dynamical and thermal tropopause is investigated in the following. Therefore the mixing layer observed on 27 April 2003 is divided into different parts. Relative to the dynamical tropopause, which is assigned by the 2 PVU isoline, all measurements within the mixing layer on this day are analyzed (Figure 4.7, upper right–hand panel, black line). The distance to the dynamical tropopause $\mathrm{DTP_{dyn}}$ is given in potential temperature. The extent of the mixing layer is largely above the dynamical tropopause. A few measurements are also observed up to –10 K below the dynamical tropopause. Fur-

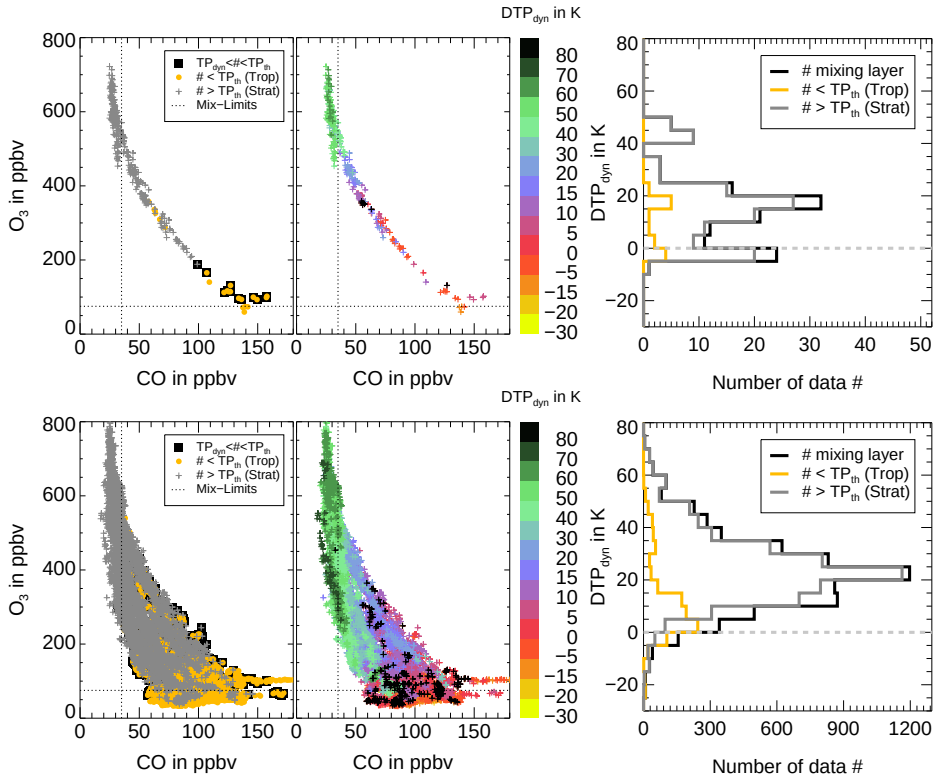

Figure 4.7: Top panels: O_3 and CO tracer correlation during the SPURT flight on 27 April 2003 (two left–hand panels). Measurements above the thermal tropopause in gray crosses, below the thermal tropopause in orange crosses and the measurements between the thermal and the dynamical tropopauses are additionally highlighted by black squares. The correlation is also colored with the distance to the dynamical tropopause $\mathrm{DTP_{dyn}}$ in K (middle panel). In this plot the 1 K distance between the dynamical tropopause is marked by the black crosses. The number of data points within the mixing layer are also shown relative to the dynamical tropopause (right–hand panel). Bottom panels: The same analysis as above but for all SPURT flights together.

thermore, the mixing layer is divided into parts containing measurements above the thermal tropopause (gray line) and below (orange line). Thus many data points are both above the thermal tropopause and above the dynamical tropopause. There is a maximum around 20 K above the dynamical tropopause. These measurements are within the TIL or within the stratosphere above. There are also some measurements which are above the dynamical tropopause, but below the thermal tropopause. These are within a layer of around 30 K above the dynamical tropopause. In a O_3 and CO tracer correlation plot these measurements between the dynamical and thermal tropopause are exactly those measurements in the lower

part of the mixing layer (Figure 4.7, upper left–hand panel, black squares), which are related to a low static stability (Figure 4.5, box 2 in panel(b)). There are also some measurements up to 10 K below the dynamical tropopause which are above the thermal tropopause.
In an analysis of all SPURT flights together (Figure 4.7, lower panels), the part between the thermal and dynamical tropopause extends up to 40 K above the dynamical tropopause (lower right–hand panel, orange line) and the maximum of the measurements above the thermal tropopause around 20 K above the dynamical tropopause is enhanced. The mixing layer as observed during all SPURT flights lies mainly above the dynamical tropopause (lower right–hand panel, black line). This is also expressed in the O_3–CO tracer correlation, which is colored according to the distance to the dynamical tropopause (Figure 4.7, bottom middle panel). The black crosses represent values close to the dynamical tropopause within $\mathrm{DTP_{dyn}} = \pm 1\,\mathrm{K}$, which are mainly below or in the lower branch of the mixing layer around the mixing–limit line toward the tropospheric reservoir.
The measurements between the dynamical and thermal tropopause are also related to dynamical situations in the vicinity of the jet streams related to a break of the thermal tropopause. Then the tropical tropopause partly penetrates the midlatitude region. Tropospheric intrusions of trace gases from the upper troposphere at low latitudes to the lower troposphere at high latitudes are likely related to these secondary tropopauses during SPURT. These intrusions are characterized by a low O_3 concentration, a low equivalent latitude and a static stability lower than in the stratosphere, but higher than in the troposphere (Pan et al., 2009b). These air masses in the vicinity of the jet streams are also between the dynamical and thermal tropopause and are transported from lower toward higher latitudes. In the following, these air masses are referred to as TFM branch, i.e., the 'Tropospheric Freshly Mixed' branch.

4.2.3 A new measure of mixing degree in the extratropical UT/LS

To investigate the relationship between static stability N^2 and mixing in the UT/LS during all SPURT flights, a measure for quantifying the mixing degree deduced from tracer correlations is proposed. This parameter f_{mix} depends on the location of the mixing points in a tracer correlation plot and is shown for all SPURT flights in Figure 4.8 (left–hand panel). f_{mix} is designed to measure both the distance to the undisturbed stratospheric ($CO < 34\,\mathrm{ppbv}$) and tropospheric ($O_3 < 75\,\mathrm{ppbv}$) reservoirs (gray colored) and the distance to the intersection point (red point) of the mixing–limit lines in the tracer space. This point is identical to the so–called 'chemopause' (Pan et al., 2004), here in the idealized 'L–shaped' tracer correlation.

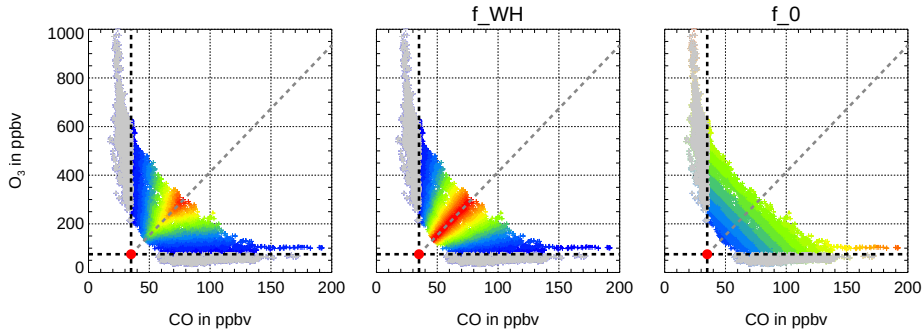

Figure 4.8: O_3 and CO correlation of all SPURT measurements colored with the dimensionless measure f_{mix} to quantify mixing (left–hand panel), which depends on f_{WH} (middle panel) and f_0 (right–hand panel). The intersection point of mixing–limit lines is marked by the red point and the bisecting line is gray dashed. Stratospheric and tropospheric reservoirs in gray for all panels.

Thus, the functional relationship f_{mix} depends on two different terms according to

$$f_{mix}(x,y) = f_{WH}(x,y) \cdot f_0(x,y)\,, \tag{4.3}$$

with dimensionless variables x for CO and y for O_3. The trace gases are normalized by their respective maxima ($O_3 = 1000$ ppbv, CO $= 192$ ppbv) as observed during SPURT and by the limits of the mixing layer according to $\mathrm{x} = (\mathrm{CO} - 34\,\mathrm{ppbv})/192\,\mathrm{ppbv}$ and $\mathrm{y} = (\mathrm{O_3} - 75\,\mathrm{ppbv})/1000\,\mathrm{ppbv}$. f_{mix} is valid within the mixing area in the correlation plot (color–coded in Figure 4.8, left–hand panel), i.e., the original reservoirs (gray colored) are considered to be unmixed with $f_{mix} = 0$. The two terms $f_{WH}(x,y)$ and $f_0(x,y)$ are described in detail in the following.

In a correlation plot, the mixing degree depends on the distance to the original undisturbed reservoirs of the troposphere and stratosphere. Thus, the distance to the bisecting line (dashed gray line) between the two original reservoirs must be accounted for to find the strongest mixing degree in the vicinity of this line and the lowest one close to the original reservoirs. This can be described by the function

$$f_{WH}(x,y) = \begin{cases} \frac{y}{x} & \text{if} \quad y < x \\ \\ \frac{x}{y} & \text{if} \quad x < y \end{cases}\,, \tag{4.4}$$

which is shown in Figure 4.8 (middle panel). The function $f_{WH}(x,y)$ is also motivated by the entropy–based measure of mixing at the tropopause introduced by Patmore and Toumi

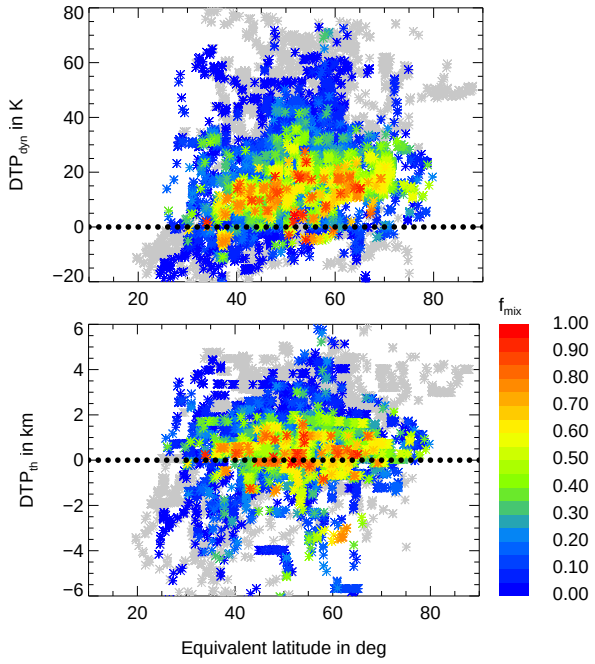

Figure 4.9: Mixed region of all SPURT measurements (color coded with f_{mix}) dependent on the distance to the dynamical tropopause ($\mathrm{DTP_{dyn}}$) in K, defined as $\mathrm{PV} = 2\,\mathrm{PVU}$ surface, and the equivalent latitude (top panel). The same mixed region relative to the thermal tropopause ($\mathrm{DTP_{th}}$) in km (bottom panel). Stratospheric and tropospheric reservoirs in gray for both panels.

(2006), who divided the tracer space into five mixing states to quantify the mixing degree. These divisions are similar to the function $f_{WH}(x, y)$ with the most mixed air mass furthest away from the original reservoirs.

Using $\mathrm{O_3}$–CO correlations mixing can be represented by straight lines between the two non–mixed reservoirs of the stratosphere and troposphere in an idealized manner (Hoor et al., 2002; Pan et al., 2007b). The mixing degree further depends on the distance of these mixing lines to the intersection point of both mixing–limit lines (red point in Figure 4.8), i.e., the greater the distance of a particular mixing line from this point the more strongly the corresponding stratosphere–troposphere exchange event is dominated by mixing. This mixing feature is described by the second functional relationship

$$f_0(x, y) = x + y\,, \tag{4.5}$$

which assigns a mixing degree relative to the intersection point of mixing–limit lines (Figure 4.8, right–hand panel). The resulting dimensionless measure of the mixing degree $f_{mix}(x, y)$ according to Equation (4.3) is largest in the vicinity of the bisecting line between the two reservoirs (gray dashed) and decreases both toward the unmixed reservoirs (gray colored) and toward the intersection point (Figure 4.8, left–hand panel). $f_{mix}(x, y)$ is scaled by its local maximum value $f_{mix}^{max} \approx 0.45$ at the bisecting line for SPURT measurements to receive values of $f_{mix}(x, y)$ between 0 and 1. Thus, the mixing degree $f_{mix}(x, y)$ is designed as a measure of how much the air mass deviates from the background stratosphere and troposphere due to the mixing in its history.

Mixing, as it is diagnosed in the CO–O_3 tracer space by $f_{mix}(x, y)$, is a very simple representation of a full three–dimensional process. Different mixing scenarios can leave the same signature in the CO–O_3 tracer space, i.e., for a given point in the CO–O_3 tracer space, it is not possible to reconstruct the mixing line along which mixing of air masses has occurred. Thus, $f_{mix}(x, y)$ as proposed here is an empirical attempt to quantify the mixing degree by using only the measurable quantities (CO and O_3). In particular, the highest function scores for CO–O_3 tracer values far away from the undisturbed reservoirs and far away from the intersection point of mixing–limit lines represent mixing lines which connect those parts of the troposphere and stratosphere which in an undisturbed atmosphere are also geometrically far away from each other. Thus, a high mixing degree expected in such 'strong mixing events' is measured by high values of f_{mix}. An advantage of this simple function $f_{mix}(x, y)$ compared with the approach of Patmore and Toumi (2006) is the fact that no further physical parameters have to be introduced and the mixing degree is characterized by a continuous variable.

Figure 4.9 (top panel) shows the meridional distribution of $f_{mix}(x, y)$. The equivalent latitude is used as meridional coordinate, which is inferred from the PV distribution on isentropes (see also Chapter 5). The vertical coordinate $\mathrm{DTP_{dyn}}$ is the distance to the dynamical tropopause $\mathrm{TP_{dyn}} = 2\,\mathrm{PVU}$ in potential temperature space. The meridional distribution of $f_{mix}(x, y)$ peaks for strongly mixed air masses just above the dynamical tropopause. When the distribution is calculated relative to the thermal tropopause (bottom panel), the largest $f_{mix}(x, y)$ is around the thermal tropopause. This shows the location of the mixing layer, for the most time above the dynamical tropopause, but around the thermal tropopause.

4.2.4 Static stability and mixing degree in the TIL and TFM branch

The case study in Figure 4.5 reveals that the mixing layer contains air masses within the TIL above the thermal tropopause $\mathrm{TP_{th}}$ (box 1) and air masses freshly mixed from the troposphere with a lower N^2 (box 2).

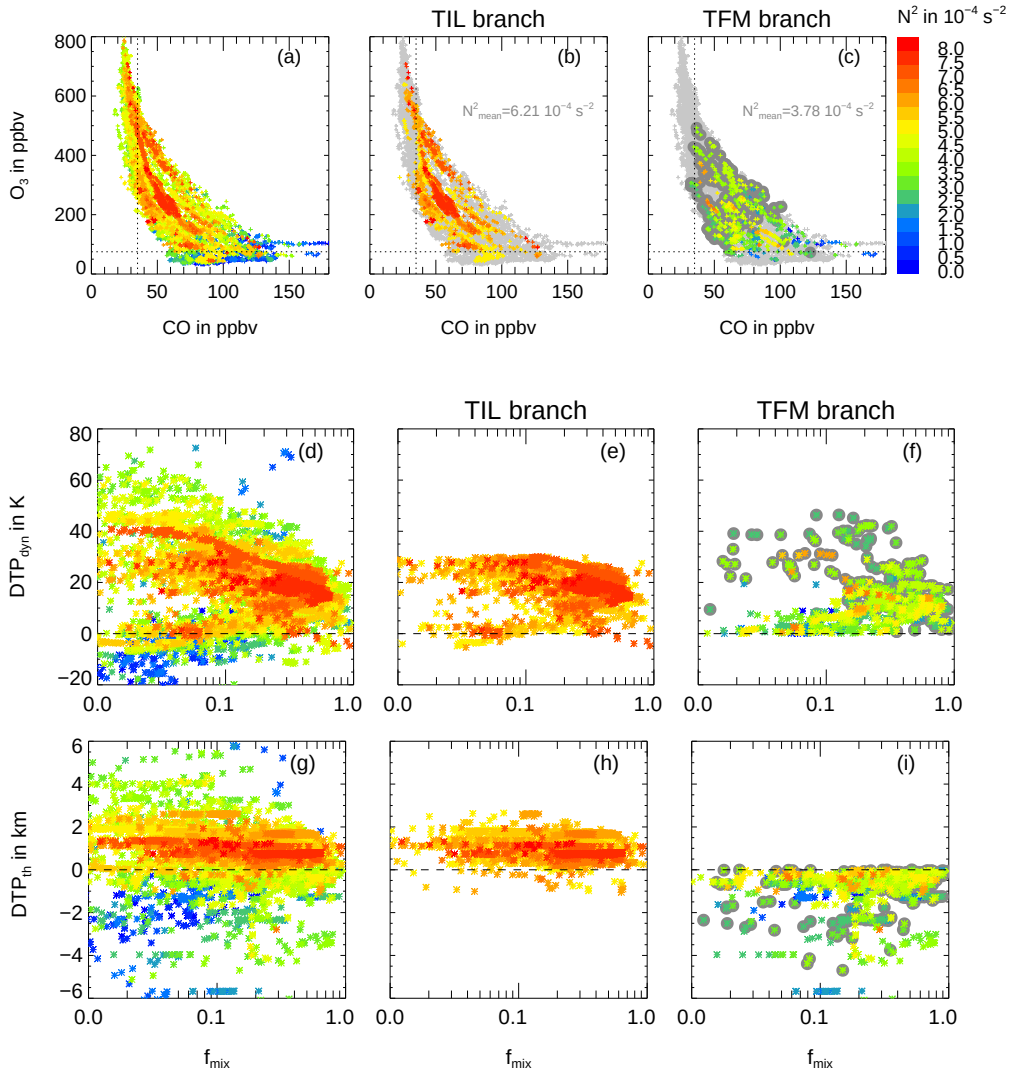

Figure 4.10: Top panels: O_3 and CO tracer correlation colored with the static stability N^2 in $10^{-4}\mathrm{s}^{-2}$ for all SPURT measurements (panel (a)), those within the TIL branch (panel (b)) and the tropospheric freshly mixed (TFM) branch (panel (c)). Middle panels: Dependency of N^2 on the distance to the dynamical tropopause $\mathrm{DTP_{dyn}}$ in K and f_{mix} for the entire mixing layer (panel (d)), the TIL (panel (e)) and the TFM branch between $\mathrm{TP_{dyn}}(2\,\mathrm{PVU})$ and $\mathrm{TP_{th}}$ (panel (f)). Bottom panels: N^2 dependent on the distance to the thermal tropopause $\mathrm{DTP_{th}}$ in km. Data between $\mathrm{TP_{dyn}}(4\,\mathrm{PVU})$ and $\mathrm{TP_{th}}$ are bordered in dark gray (panels (c), (f) and (i)).

Figure 4.10 (a) shows the corresponding correlation of all SPURT O_3 and CO measurements colored according to the static stability N^2. To identify air masses within the TIL all the data are selected according to the criteria:

- above the thermal tropopause $\mathrm{TP_{th}}$
- high static stability ($\mathrm{N^2} > 5 \cdot 10^{-4}\,\mathrm{s^{-2}}$)
- close distance to the dynamical tropopause ($\mathrm{DTP_{dyn}} < 30\,\mathrm{K}$)

In the following, these observations are denoted as *'TIL branch'*. The second selection criterion is motivated by the definition of the TIL in Bian and Chen (2008) and the value of 30 K seems appropriate considering the thickness of the layer above the tropopause with enhanced mixing degree f_{mix} (Figure 4.9, top panel). On the other hand, the mixing layer also consists of freshly mixed air masses from the troposphere that can be identified as those data points between the dynamical tropopause $\mathrm{TP_{dyn}}$ and the thermal tropopause $\mathrm{TP_{th}}$, the so–called TFM branch (see section 4.2.2).
The corresponding plots in Figure 4.10 (b) and (c) show a mean static stability of $N^2_{mean} = 6.21 \cdot 10^{-4}\,\mathrm{s^{-2}}$ within the TIL branch and a lower mean static stability of $N^2_{mean} = 3.78 \cdot 10^{-4}\,\mathrm{s^{-2}}$ in the TFM branch of the mixing layer. There is a clear difference in mean static stability for these two branches as expected due to the selection of data above and below the thermal tropopause. Furthermore, the lower boundary of the TFM branch is defined by the dynamical tropopause $\mathrm{TP_{dyn}} = 2\,\mathrm{PVU}$ (colored in panels (c)). This PV value representing the dynamical tropopause is to some extent arbitrary as we discuss this point in Chapter 5. The mean potential vorticity value at the thermal tropopause locations during all SPURT flights is calculated to $\mathrm{PV} \approx 4\,\mathrm{PVU}$. A selection of the TFM branch according to a dynamical tropopause $\mathrm{TP_{dyn}} = 4\,\mathrm{PVU}$ is additionally shown as gray bordered dots (Figure 4.10, panel (c)). Air masses between the dynamical and thermal tropopause on average have PV values roughly between $2\,\mathrm{PVU}$ to $4\,\mathrm{PVU}$, which from a PV dynamics point of view supports the notation of 'freshly mixed'. Both the TFM and the TIL branch lie well within the mixing layer, with the TIL branch partly penetrating the stratospheric reservoir.
Figure 4.10 panel (d) shows the relation between N^2 and f_{mix} within the entire mixing layer dependent on the distance to the dynamical tropopause $\mathrm{TP_{dyn}} = 2\,\mathrm{PVU}$. At a mixing degree of $f_{mix} > 0.2$, a high N^2 is observed and the vertical extension of the mixing layer is close to the tropopause. At a very low mixing degree of $f_{mix} = 0.05$, the mixing layer extends between $-20\,\mathrm{K}$ to $60\,\mathrm{K}$ around the dynamical tropopause, at a high mixing degree of $f_{mix} = 0.60$ mainly up to $30\,\mathrm{K}$ above the tropopause. A figure using the distance to the thermal tropopause in km as vertical coordinate (panel (g)) shows that the high N^2 values at low

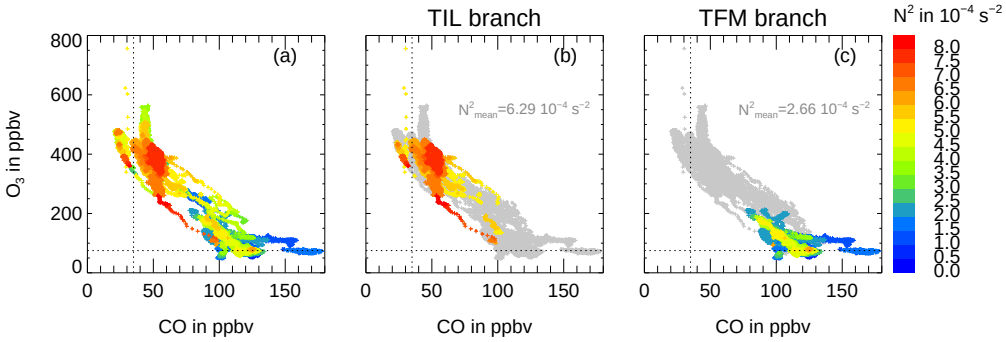

Figure 4.11: O_3 and CO tracer correlation colored with the static stability N^2 in $10^{-4}s^{-2}$ for POLARCAT measurements (panel (a)), those within the TIL branch (panel (b)) and below the thermal tropopause (panel(c)).

mixing degree $f_{mix} < 0.1$ more than $30\,K$ above the dynamical tropopause are within $2\,km$ above the thermal tropopause. These values are i.a. observed in the vicinity of secondary tropopauses related to a jet stream, when the distance relative to TP_{dyn} may be larger than relative to TP_{th}. The region of high N^2 identified by high f_{mix} lies within the TIL (panel (e)). The TFM branch with a lower N^2 extends up to $DTP_{dyn} = 40\,K$ (panel (f)). Values above $DTP_{dyn} = 20\,K$ are associated with mixing events in the vicinity of secondary tropopauses, when the distance between TP_{dyn} and TP_{th} becomes very large. Due to a strongly disturbed dynamical situation, the PV isolines are deformed and thus TP_{dyn} and TP_{th} diverge.

Figure 4.11 shows the correlation of all POLARCAT O_3 and CO measurements colored according to the static stability N^2. The high static stability within the mixing layer (panel (b)) is also a feature of the polar region. Nevertheless, the definition of the TFM branch is difficult to use at higher latitudes due to the lower limit of the dynamical tropopause TP_{dyn}. The 2 PVU isoline is used as threshold for the dynamical tropopause, which may be for the polar region not as appropriate as for the midlatitude region. This is a disadvantage of the TFM branch as defined above. Thus, in POLARCAT all measurements below the thermal tropopause are defined as TFM branch (panel (c)). One possibility to use the same definition of the TFM branch at midlatitudes and the polar regions is to use a dynamical tropopause, which is not based on a particular PV value, but rather on the PV gradient dependent on the time and the geographical location. This method to define a tropopause will be discussed in Chapter 5.

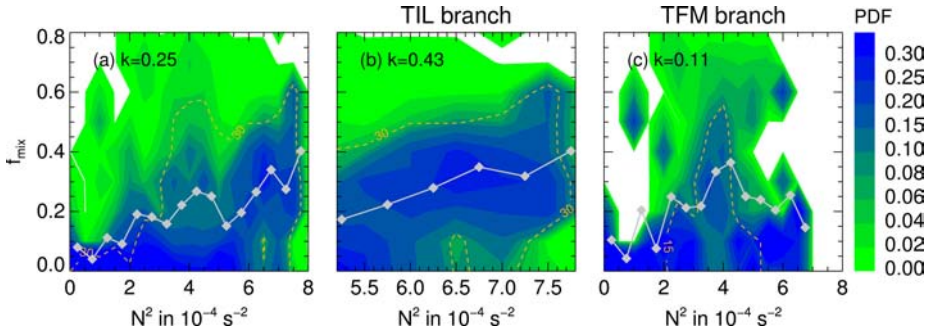

Figure 4.12: Correlation between the mixing degree f_{mix} and N^2 as probability distribution function for the entire mixing layer (panel (a)), TIL branch (panel (b)) and TFM branch (panel (c)). The bin size is $0.5 \cdot 10^{-4}\mathrm{s}^{-2}$ for N^2 and 0.1 for f_{mix}. Each N^2 bin is normalized, i.e., the probability (color coding) reflects the percentage of the mixing degree f_{mix} in a particular N^2 interval. The solid gray line shows the mean f_{mix} in each N^2 interval and the area with a bin size larger than 30 (15 in the case of TFM branch) is bordered by the orange line. Spearman's rank correlation coefficients k are additionally shown (top left).

4.2.4.1 Correlation between static stability and mixing degree

The relation between N^2 and the mixing degree described by f_{mix} is also shown as a probability distribution function (Figure 4.12). For this purpose $0.5 \cdot 10^{-4}\mathrm{s}^{-2}$ bins for N^2 and 0.1 bins for f_{mix} are calculated. Each N^2 bin is normalized, i.e., the probability (color coding) reflects the percentage of the mixing degree f_{mix} in a single N^2 interval. There is a positive correlation between the two quantities in the entire mixing layer (panel (a)). The Spearman's rank correlation is around $\mathrm{k} = 0.25$. When the mixing layer is split into the TIL branch (panel (b)) and TFM branch (panel (c)) again, a lower correlation coefficient of $\mathrm{k} = 0.11$ is found for the relation within the TFM branch and a higher one of $\mathrm{k} = 0.43$ in the TIL branch. Especially in the TIL branch, the mean f_{mix} (gray lines) per N^2 bin increases with N^2 and most data points are located around this mean f_{mix}. This is demonstrated by the bordered bins with more than 30 data points (orange line). There is no clear relationship between f_{mix} and N^2 in the TFM branch and there is a negative correlation for $N^2 > 4 \cdot 10^{-4}\,\mathrm{s}^{-2}$. The higher correlation $\mathrm{k} = 0.43$ within the TIL branch suggests a connection between the TIL with enhanced N^2 and the mixing layer above the tropopause.

4.2.4.2 Significance and strength of the correlation

To test the significance of the correlation $\mathrm{k} = 0.43$ between N^2 and f_{mix} within the TIL branch one has to estimate the effective number of degrees of freedom. That means, that the correlation will not be significantly different from zero, if the number of data points are not

independent of each other and are partly autocorrelated. The determination of this autocorrelation is difficult because the data within the TIL branch are not equidistantly selected. The data set is not distributed homogeneously in time. Therefore, the use of methods to examine the effect of autocorrelation like those described by Quenouille (1952) and Kristjannsson et al. (2002) or Ebisuzaki (1997) is not advisable in this case. Instead the significance of the correlation within the TIL branch is tested with two different methods, both with the bootstrap method (Press et al., 2002) and with simulated data sets reproducing the observed time scale analysis of N^2 (shown in Figure 4.14) and f_{mix} (not shown), which are described in the following.

The sample size of measurements within the TIL branch is $n = 2858$ and therefore the theoretical error of the correlation $\mathrm{k} = 0.43$ between N^2 and f_{mix} is estimated to

$$\sigma_{theo} = \frac{1}{\sqrt{n}} = 0.018705481\,. \tag{4.6}$$

The number of effective data points n_{eff} has to be very close to the total sample size n for a correlation significantly different from zero. For this reason one has to test the reproducibility of the correlation. This is done on three ways:

1. Two random samples x and y with a sample size of $n = 2858$ are generated and the correlation coefficient, which should be close to zero, is calculated. This procedure is repeated 1000 times and a mean correlation coefficient $k = 0.000512050$ of the 1000 single correlation coefficients is calculated. Its standard deviation, which corresponds to the reproducibility of this correlation, is $\sigma = 0.0182716$. This calculation serves as an example, showing the dependence of the effective number of data points on the behavior of the random samples. If both statistical samples are smoothed about 30 data points, the standard deviation will increase at $\sigma = 0.080013081$ and only $n_{\mathrm{eff}} = \frac{1}{\sigma^2} = 156$ effective data points will be left. In this case the reproducibility would be lowered. If the samples are doubled, the effective number of data points will still be very close to $n = 2858$. A significant decrease of the effective number of data points can be achieved by a multiple of 13 samples. In this case only 165 independent data points are left.

2. For the bootstrap method the actual data sets of N^2 and f_{mix} with a sample size of $n = 2858$ data points are used to generate any number of synthetic data sets b_{N^2} and $b_{f_{mix}}$, also with n data points. The procedure of this test is simply to draw $1/\mathrm{e} \approx 37\,\%$ data points of these samples and replace the gaps with the same number of data points still containing to the data set. So the replaced data points are duplicated original data

points and thus the original data set is not get back at any time. This replacement is performed $i = 100$ times and the correlation coefficient k_i is calculated for the i new generated data sets. The mean correlation coefficient of these i new data sets is $k_{boot} = 0.42427782$ and its standard deviation is $\sigma_{boot} = 0.014789961$.

This value of the error is improved compared to the theoretical value (see equation 4.6). This is due to the duplication of the original data points, which leads to an underestimation of the respective error. For this reason a scale factor σ_{scale} has to be determined. Therefore, 100 different pairs of random samples of the size n are again generated. The bootstrap method is applied on each sample pair 100 times as described above and the standard deviation is $\sigma_{random} = 0.018586635$ of all 100 mean correlation coefficients. The scale factor is the ratio between σ_{random} and σ_{theo} and is determined to $\sigma_{scale} = 1.00639$. This scale factor is multiplied by σ_{boot} and the correct amount of the reproducibility estimated by the bootstrap method is $\sigma^*_{boot} = 0.0148845$, which corresponds to a very high effective number of data points $n_{\text{eff}} = \frac{1}{\sigma^2_{boot}}$.

3. Data sets are now generated to reproduce the observed time scale analysis of N^2 and f_{mix} within the TIL branch. Two examples of such simulated data sets, x_{sim} and y_{sim}, with the same sample size as the observed data sets are shown in Figure 4.13 (right–hand panels). They represent approximately the same time scale behavior as the original data sets of N^2 and f_{mix} (left–hand panels) and correspond to approximately the same correlation coefficient of $k = 0.4$. This is achieved by the following equations

$$z = \sin\left(\frac{z_{random}}{1.25} \cdot \pi\right)^3 + 3 \cdot \sin\left(\frac{z_{random}}{1.25} \cdot \pi\right) \tag{4.7}$$

$$x_{sim} = x_{random} + z \cdot 8 \tag{4.8}$$

$$y_{sim} = y_{random} + z \cdot 0.34 \tag{4.9}$$

with x_{random} and y_{random} as random samples with a sample size n as the observed data set, and the sample $z_{random} = \frac{i}{n-1}$ with $i = 1, \ldots n$. The first summand of Equation 4.7 contains the noise of data on each time scale and the second summand accounts for the noise of data on small time scales. Equations 4.8 and 4.9 modify the correlation between the two simulated data sets x_{sim} and y_{sim}, which is the same as for the observed data sets.

The variance analysis of x_{sim} (bottom panel, dashed orange line) is similar to that of N^2 within the TIL branch (solid orange line). Further, the variance analysis of the correlation between x_{sim} and y_{sim} at each time scale (dashed black line) is also similar to that of the observed data sets N^2 and f_{mix} (solid black line). The variance of the cor-

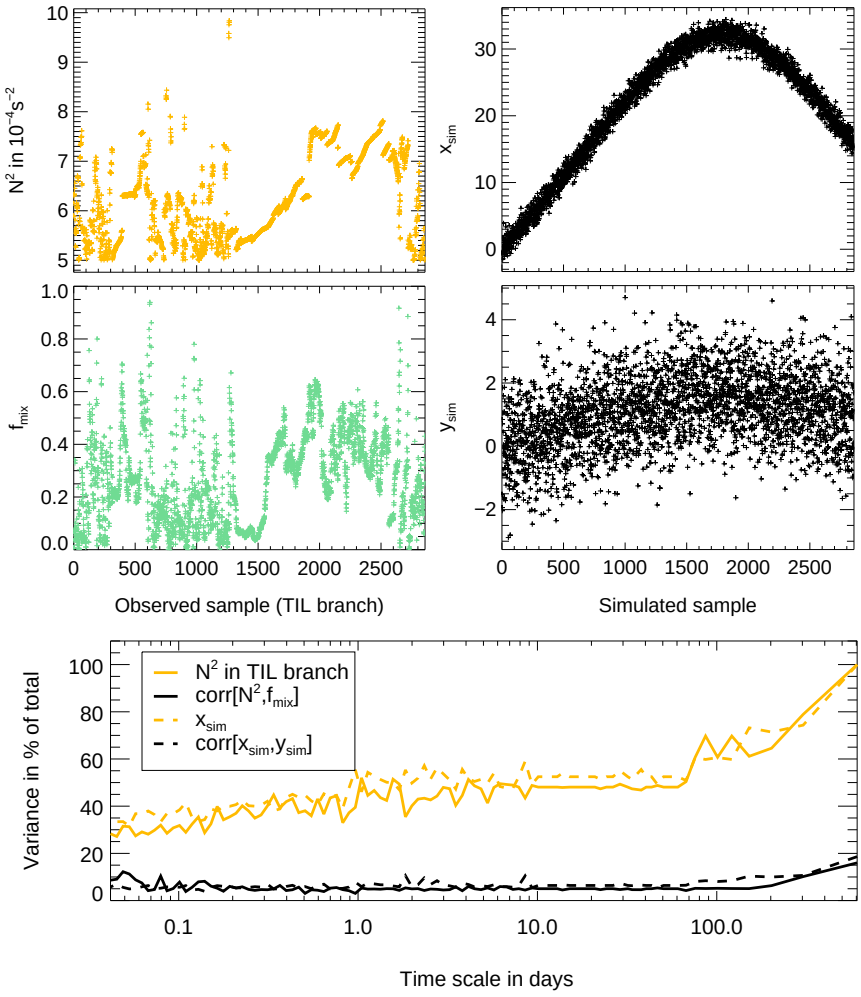

Figure 4.13: The two observed data samples of N^2 and f_{mix} within the TIL branch (left–hand panels, orange and green color, respectively) and the two simulated samples x_{sim} and y_{sim} (right–hand panels, black color) with a time scale behavior approximated to the observed time scale of N^2 and f_{mix} within the TIL branch and an approximated correlation coefficient of $k = 0.4$. The bottom panel shows the variance analysis of these simulated data samples (orange dashed curve) and of the observed data samples (orange solid curve) together with the respective variance analysis of the correlation between both simulated samples (black dashed curve) and both observed samples (black solid curve).

relation enhances especially at time scales larger than 100 days. Thus, the correlation between both samples is mainly achieved on seasonal time scales. The variance analysis demonstrates that x_{sim} and y_{sim} are samples with the same time scale behavior as the original data sets.

To test the reproducibility of the correlation between N^2 and f_{mix} in the TIL branch, the samples x_{sim} and y_{sim} are generated for 1000 times and the standard deviation of the mean correlation coefficient is $\sigma_{var} = 0.01520449$. It is also very close to the theoretical error of the correlation (see equation 4.6) and corresponds to a high effective number of data points n_{eff} close to the observed sample size n, whereas theoretically n_{eff} can also be larger than n.

Therefore, the reproducibility of the correlation, derived by the bootstrap method and the reproduction of data sets with the same observed time scale analysis, is consistent with an effective number of degrees of freedom close to the number of data points. On these grounds the level of significance for the null hypothesis that the correlation is equal to zero, is estimated to $3\sigma_{theo} \approx 0.06$ at an error probability of 0.01. Therefore, the null hypothesis has to be rejected and the correlation $\mathrm{k} = 0.43$ in the TIL branch is significant.

Nevertheless, a correlation coefficient of r=0.43 implicates that the dominant amount of variance of one variable is caused by processes not common with the other variable. These might be physical processes or systematic differences caused by instrumental noise etc. The correlation between N^2 and f_{mix} involves systematic differences as for example the method to derive N^2. Here, the position of the aircraft in space and time is calculated to 12 UTC with the help of CLaMS trajectories. Then, N^2 is interpolated from ECMWF data for this position at noon time. At least three problems arise by this procedure: The ECMWF data might represent N^2 on a larger grid than appropriate for the aircraft, the trajectories are subject to errors, and N^2 might change on the course of several hours. The amount of variance generated by the latter two points is estimated by calculating both to 12 UTC and to 18 UTC (two of the four ECMWF time scales per day) for several comparable flights. The mean of the difference of static stability between 12 UTC and 18 UTC is $N^2_{mean} = 0.08 \cdot 10^{-4}\,\mathrm{s}^{-2}$ and the standard deviation of this difference is $N^2_{stdev} = 0.5 \cdot 10^{-4}\,\mathrm{s}^{-2}$. This standard deviation corresponds to a variance of $N^2_{variance} = 0.25 \cdot 10^{-8}\,\mathrm{s}^{-4}$. This variance of the difference between both approaches for N^2 is on the order of $33\,\%$ of its total variance $0.71 \cdot 10^{-8}\,\mathrm{s}^{-4}$ (see Figure 4.14). Together, this artificial source of variance in N^2 and the correlation of r^2=0.18 explain the major part of observed variance. Thus, the correlation between N^2 and f_{mix} including this artificial source of variance might be enhanced.

According to Toenges-Schuller et al. (2006) the linear correlation coefficient r_{ij} of two data

sets x_i and x_j is connected to the relative error variances e_{ii}, e_{jj} and the covariances e_{ij} of the two data sets, i.e.,

$$r_{ij}^2 = \frac{(1-e_{ii})(1-e_{jj})}{(1-e_{ij})^2}\,. \tag{4.10}$$

The relative error variances are defined by $e_{ii} = \frac{\mathrm{var(\eta_i)}}{\mathrm{var(x_i)}}$ and $e_{ij} = \frac{\mathrm{cov}(\eta_\mathrm{i},\eta_\mathrm{j})}{\mathrm{cov}(\mathrm{x_i},\mathrm{x_j})}$. The standard deviation of the respective data sets is η.

In the case of the correlation between f_{mix} and N^2 within the TIL branch the relative covariance of the errors e_{ij} is expected to be zero. The measuring instruments of both data sets are independent of each other and thus the errors of both data sets are not correlated and $e_{ij} = 0$. Including the relative error due to the trajectory calculation to 12 UTC or 18 UTC respectively, the maximum correlation can be estimated to

$$r_{max}^2 = 1 - \frac{0.25}{0.71} = 0.65\,. \tag{4.11}$$

For these reasons the correct amount of correlation might be achieved only by synchronous measurements of both variables together with a reliable estimate of experimental noise. Thus, an improved correlation can be expected if these more artificial sources of variance were removed.

4.3 Time scales of processes within the TIL and TFM branch

4.3.1 Variance analysis

In order to investigate the different time scales of atmospheric processes which play a role within the TIL and TFM branch (Figure 4.10), the temporal N^2 variances in these branches are shown in Figure 4.14 (green and orange lines, respectively). A temporal variance analysis (Rohrer and Berresheim, 2006; Kunz et al., 2008) provides information on the atmospheric processes which influence the variability of specific atmospheric parameters such as N^2 (see also section 3.3). Around 80% of the total N^2 variance within the TFM branch is already achieved after 8 days (gray–green dot), the same fraction of total N^2 variance in the TIL branch is achieved after 360 days (gray–orange dot). The analysis suggests that fresh mixing from the troposphere in the TFM branch plays a role on a synoptic time scale of up to 8 days (green dashed, Figure 4.14). Processes which contribute to the formation of the TIL may occur rather on a seasonal time scale up to 360 days (dashed orange line, Figure 4.14). The N^2 variance increases on the seasonal time scale and there is no enhancement on the synoptic time scale within the TIL branch. The seasonal time scale is required for radiative adjustment in the atmosphere. The N^2 variance within the TIL branch starts to increase on a time scale

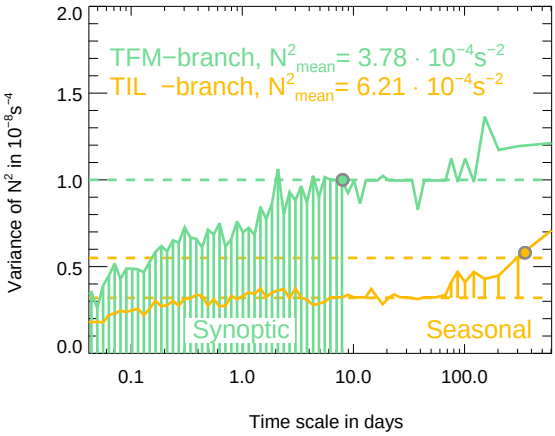

Figure 4.14: Temporal variance analysis of N^2 in $10^{-8}\,\mathrm{s}^{-4}$ within the TIL branch (orange line) and TFM branch (green line). The time scale is shown from several minutes to 600 days. 80% of the total N^2 variance within the TFM branch and TIL branch is marked by the gray–green or gray–orange dot, respectively. The mean values of N^2 in $10^{-4}\,\mathrm{s}^{-2}$ in both branches are denoted in the legend. The greatest increase of the variance within the TIL branch is achieved on the seasonal time scale (orange dashed), that of the variance in the TFM branch is strongest on the synoptic time scale (green dashed).

of more than 60 days. The problem of under–represented data bins roughly between 10 and 90 days was already discussed in section 3.3.4. The variance remains unchanged on the inter–seasonal time scales. For smaller time scales, which are represented by sufficient measurement data, the variance changes. Thus, the exact seasonal time scale when the variance increases again may be influenced.

4.3.2 CLaMS trajectory calculations

The temporal and also the spatial development of the static stability N^2 is now investigated with the help of CLaMS trajectory calculations. The trajectories are initiated at the location of the flight path and a backward trajectory calculation on a typical synoptic 10 day time scale is done. The data output is hourly. Figure 4.15 shows the horizontal distribution of trajectories calculated backward from the SPURT flight on 27 April 2003 (top panels) and the POLARCAT flight on 15 July 2008 (bottom panels). The trajectories are selected according to the initial position within the TIL branch (left–hand panels) and within the TFM branch (right–hand panels). A clear distinction between both branches is apparent in the static stability, which is higher on all trajectories in the TIL branch at initial time than on trajectories in the TFM branch. For the midlatitude SPURT flight the 10 day trajectories from the TIL and TFM branches are at midlatitudes between 35° N to 70° N (Figure 4.16, left–hand top

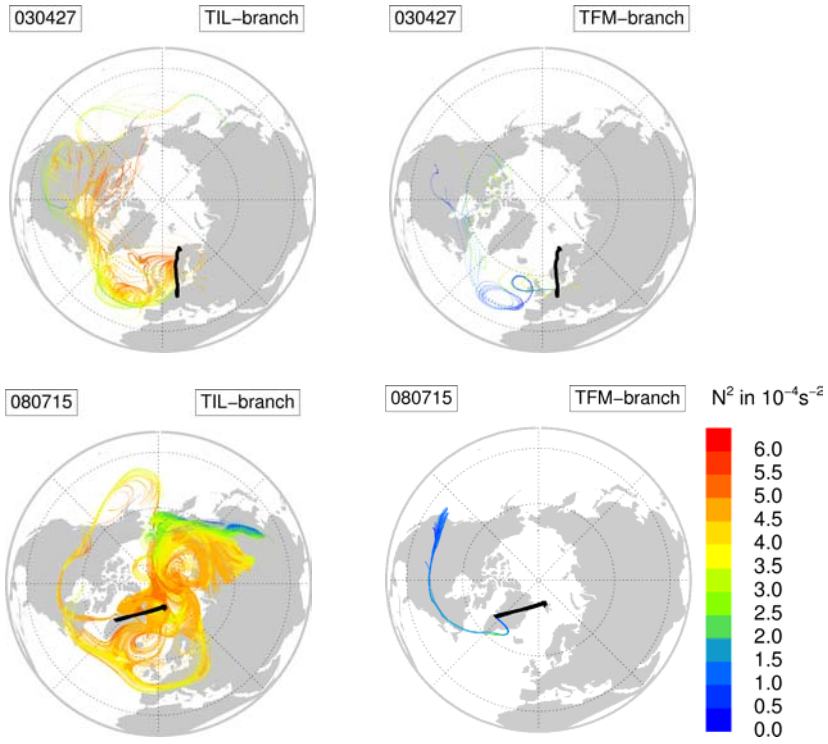

Figure 4.15: Static stability on 10 day backward trajectories for the SPURT flight on 27 April 2003 (top panels) and the POLARCAT flight on 15 July 2008 (bottom panels). The trajectories are selected for the TIL branch (left–hand panels) and the TFM branch (right–hand panels) at initial time.

panel). Trajectories resulting both in the TIL branch and in the TFM branch move nearly isentropically (Figure 4.16, left–hand middle panel), with higher isentropes around 330 K–340 K in the TIL branch than in the TFM branch around 310 K–320 K. The static stability is around $N^2 = 3.5 - 5.5 \cdot 10^{-4}\,\mathrm{s}^{-2}$ during the 10 day calculation (Figure 4.16, left–hand bottom panel). The mean static stability is around $4.5 \cdot 10^{-4}\,\mathrm{s}^{-2}$ during the 10 day calculation. This supports the result of the temporal variance analysis in Figure 4.14 with the variance of the static stability being nearly constant on a synoptic time scale. In contrast, the static stability within the TFM branch on the 10 day backward trajectories shows a larger variability between $N^2 = 1.0 - 4.0 \cdot 10^{-4}\,\mathrm{s}^{-2}$ as the increasing variance of N^2 on the synoptic time scale predicts (Figure 4.14). The mean static stability is decreasing up to 5 days before the initial time, and then increasing before entering the TFM branch. The nearly isentropic trajectories within the TIL branch also motivate the TIL as dynamically well mixed layer above the the

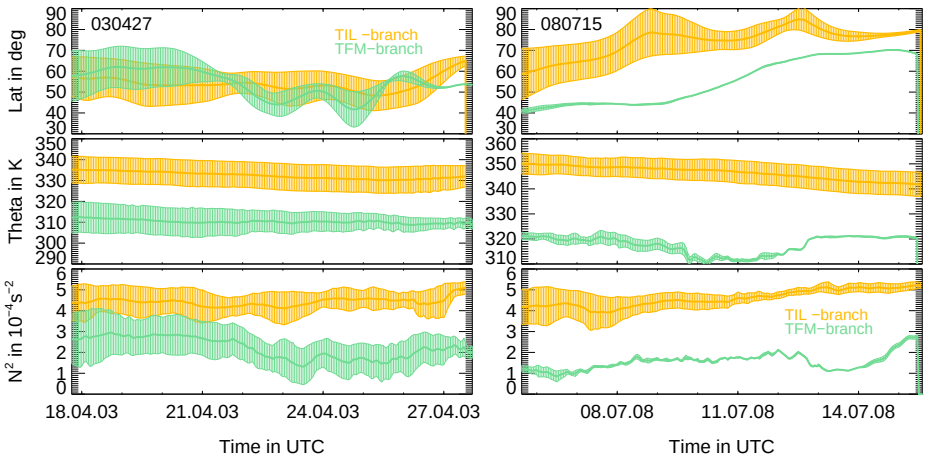

Figure 4.16: Mean latitude (top panels), potential temperature (middle panels) and static stability (bottom panels) on the 10 day backward trajectories (solid line) for the SPURT flight on 27 April 2003 (left–hand panels) and the POLARCAT flight on 15 July 2008 (right–hand panels). The standard deviation is shaded. Trajectories initiated in the TIL branch are orange colored and those initiated in the TFM branch are green colored.

tropopause as suggested by Birner (2006). Due to the strong thermal stratification within the TIL and the large–scale horizontal mixing within the TIL air masses once entering the TIL are forced to stay there and are mixed quasi–isentropically over large horizontal distances. According to this the mixing layer seems not as result of frequent vertical mixing alone but rather by subsequent horizontal redistribution of the air masses.

The trajectories for the POLARCAT flight (Figure 4.15, bottom panels) result from the polar regions in the TIL branch, but they originated at midlatitudes 10 days before. Trajectories from the TFM branch are from the midlatitudes. This is also shown by the mean latitude at the 10 day backward trajectories (Figure 4.16, right–hand top panel). The trajectories resulting in the TIL branch for the POLARCAT flight are not isentropic (Figure 4.16, right–hand middle panel), the mean potential temperature is slightly decreasing within the 10 days. This suggests, that additionally to the isentropic transport in the extratropics, the TIL branch may also be effected by a large scale downward transport of air masses. The air masses within the TFM branch from the midlatitudes are transported upward 3 days before reaching the TFM branch of the POLARCAT flight. Shortly before entering the TFM branch the transport is also on isentropes similar to the midlatitude SPURT flight. N^2 on the 10 day backward trajectories is also nearly homogeneous, with a slight enhancement during this time. This may be due to the different large scale dynamics in the polar regions compared to the midlatitudes.

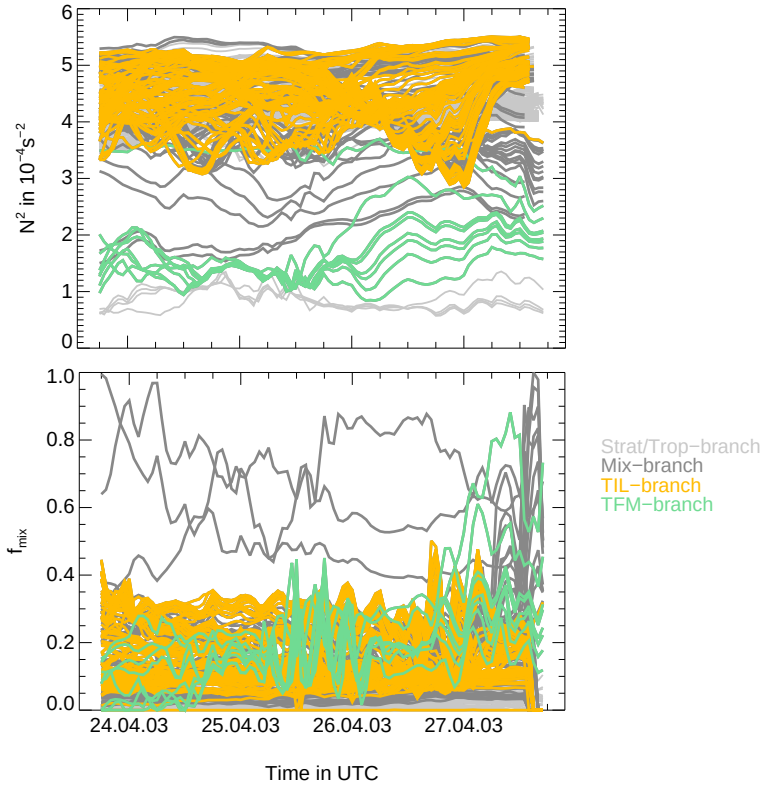

Figure 4.17: Static stability (top panel) and mixing degree (bottom panel) on the 4 day backward trajectories from the SPURT flight on 27 April 2003. Trajectories initiated in the TIL branch (TFM branch) are orange (green) colored, those from the entire mixing region are dark gray and those from the entire troposphere and stratosphere are light gray.

Figure 4.17 shows the static stability (top panel) and the mixing degree f_{mix} on the 4 day backward trajectories resulting in the TIL branch (orange colored) and the TFM branch (green colored) at initial time. The mixing degree is calculated from the ECMWF water vapor and ozone concentrations at the single time steps. The measure is also effected by the accuracy of the ECMWF model in regard to the numerical diffusion in this Eulerian model. Nevertheless, there is also a difference between f_{mix} in both branches, with a relative homogeneous distribution within the TIL branch during 4 days before and an increasing f_{mix} before entering the TFM branch. At the same time, there is also a high nearly constant distribution of the static stability on the trajectories from the TIL branch, while those from the TFM branch increase two days before entering the TFM branch.

4.4 Radiative transfer calculations

The change of N^2 caused by different mixing states and thus different trace gas gradients in the tropopause region is now investigated with radiative transfer calculations similar to those of Randel et al. (2007b). They assumed certain perturbations of the O_3 and H_2O profiles in the tropopause region and calculated the radiative response of the atmosphere regarding the impact on the temperature distribution. Here, the work of Randel et al. (2007b) is extended by deducing the perturbed O_3 and H_2O profiles from differently mixed states determined in O_3–H_2O tracer correlations. Using the Reading radiative transfer model the impacts on the vertical temperature gradient and thus the N^2 structure in the vicinity of the tropopause is studied. In contrast to Randel et al. (2007b), here O_3 and H_2O are consistently perturbed in the same altitude region by taking into account their correlation in the UT/LS.

4.4.1 Radiative transfer in the UT/LS

Radiative transfer in the atmosphere is characterized by an exchange of shortwave and longwave radiation energy between the atmosphere and the Earth surface. Radiation processes have a great influence on the behavior of the atmosphere because they govern the amount of energy entering and leaving the Earth atmosphere system and the amount of energy available for a heating and movement of air masses. The troposphere is heated by the absorption of outgoing terrestrial radiation by greenhouse gases, e.g., CO_2 or H_2O and is in radiative equilibrium between latent heating and radiative cooling by greenhouse gases. In the stratosphere increased greenhouse gases lead to a net cooling due to emitting more infrared radiation out to space than they absorb (Mohanakumar, 2008).

There is a balance between the incoming shortwave solar and outgoing longwave terrestrial radiation in the atmosphere (IPCC, 1996), which results in a stable mean global temperature. This balance is disturbed by any change in radiatively active trace gas concentrations, such as H_2O or O_3. Radiative forcing is conventionally given as the net change in radiative fluxes at the tropopause, which also can be a reasonable indicator of the surface temperature response. An increase in O_3 in the LS causes an instantaneous decrease of the shortwave flux at the tropopause and a slight increase of longwave radiation. The net instantaneous effect is a positive radiative forcing. The increase in ozone causes more absorption of solar and terrestrial radiation leading to a local warming. The maximum sensitivity of surface temperatures to ozone changes peaks near the tropopause (Forster and Shine, 1997). In contrast, an increase in H_2O in the LS causes an instantaneous decrease of the longwave flux at the tropopause. More longwave radiation is emitted into the space and this leads to a local cooling (Forster and Shine, 1999, 2002).

4.4.2 The Reading radiative transfer model

Atmospheric mixing related to an increase of climate–relevant trace gases H_2O or O_3 impacts the net change in radiative fluxes at the tropopause. In the following, the radiative forcing in the UT/LS due to a perturbation of H_2O or O_3 is examined, to analyze the radiative impact on mixing and the consequent change in thermal stratification and thus the influence on the TIL. For this purpose the 2D Reading radiative transfer model is used, which was developed by Shine (1991) to simulate atmospheric radiative processes due to the emission and scattered radiation of solar and terrestrial sources. This model simulates the latitude and height dependent characteristics of the most important absorbing trace gases such as H_2O, O_3, CO_2, CO, CH_4 and N_2O. It is a narrowband model, i.e., the longwave IR–spectrum is divided into bins with a wavenumber $\nu = 10\,\mathrm{cm}^{-1}$ and the radiative transfer is not calculated for each single spectral line. The spectral range of this model contains wave numbers between $\nu = 0 - 3000\,\mathrm{cm}^{-1}$. This model has been used for a number of scientific publications (e.g., Forster, 1999; Forster and Shine, 1999, 2002) and for the doctoral thesis by Feck (2009), who also analyzed the temperature response in the polar vortex due to a change of stratospheric H_2O. A detailed description of the model and the respective calculation of the radiative forcing and thus the net radiative fluxes is given in Feck (2009).

The temperature response in this model is determined using radiative forcing based on the approximation of fixed dynamical heating (FDH) as developed by Ramanathan and Dickinson (1979) and Fels et al. (1980), i.e., the dynamical contribution to heating is assumed to be the same for the background and perturbation calculations. The temperature T in an atmospheric region depends both on radiation processes and on dynamical processes, which tend to warm or cool the atmosphere. In an unperturbed atmosphere ($^\circ$) the rate of change of temperature in the region is given by

$$\frac{dT^\circ}{dt} = Q^\circ_{dyn} + Q^\circ_{rad}\,, \tag{4.12}$$

i.e., as sum of dynamical Q°_{dyn} and radiative Q°_{rad} heating rates (see e.g., Forster et al., 1997). In the thermodynamical equilibrium with a constant stratospheric temperature both contributions to the temperature rate of change compensate, i.e.,

$$Q^\circ_{dyn} + Q^\circ_{rad} = 0\,. \tag{4.13}$$

The radiative heating rate Q_{rad} changes when the radiative balance of the atmosphere is perturbed due to a change in greenhouse gases. In the FDH approximation the stratospheric temperature response is calculated according to Equation 4.13 making two assumptions: 1) The dynamical heating Q_{dyn} must be unchanged following a perturbation to the radiative

heating Q_{rad}. 2) The stratosphere should have time to reach an equilibrium state. According to these assumptions in the perturbation calculation the stratospheric temperatures are computed such that

$$Q^{\circ}_{dyn} + Q'_{rad} = 0\,, \tag{4.14}$$

with Q'_{rad} is the perturbed radiative heating rate. The dynamical contribution of heating is kept constant when the atmosphere is perturbed, i.e., $Q^{\circ}_{dyn} = -Q^{\circ}_{rad}$, and the temperature change in the stratosphere can be estimated according to

$$\frac{dT'}{dt} = Q^{\circ}_{dyn} + Q'_{rad} \tag{4.15}$$

and with the help of Equation 4.12

$$Q^{\circ}_{dyn} = \frac{dT^{\circ}}{dt} - Q^{\circ}_{rad}\,. \tag{4.16}$$

The assumption of fixed dynamical heating is only an approximation to the actual stratospheric response to the perturbation, because the change in the net radiative fluxes also implicates a change in dynamical processes. Despite this simplification, the FDH assumption reveals similar model results to full global climate models (Forster and Shine, 1999) and generally, most of the model calculations in regard to the temperature and climate change within the IPCC report are based on this assumption.

4.4.3 Impact of trace gas perturbations on the thermal stratification

The temperature response due to a change in trace gases in the UT/LS according to mixing is calculated with the FDH approximation, but as Forster et al. (1997) the stratosphere is not assumed to be in equilibrium, but rather in a seasonally evolving state. Thus, the left hand side of Equation 4.12 is estimated from climatological data. The radiative heating rate is also calculated from climatological data and then the dynamical heating rate is calculated as residual.

Tropopause–based zonal and time mean ECMWF vertical profiles of O_3, H_2O and temperature for all SPURT flight days at 60°N are used. The means of all other relevant trace gases for the calculation are taken from the climatological data from HALOE (Grooß and Russell, 2005) and the Mainz 2D model (Grooß, 1996). This geographical latitude is chosen as reference lying well within the TIL and the mixing layer. Figure 4.18 panel (a) shows these mean O_3 and H_2O profiles as black lines both for potential temperature in K and geometric altitude in km vertical coordinates. The tracer correlation (black dots, panel (b)) reveals a pronounced mixing layer for these ECMWF trace gas profiles. A temperature inversion up to

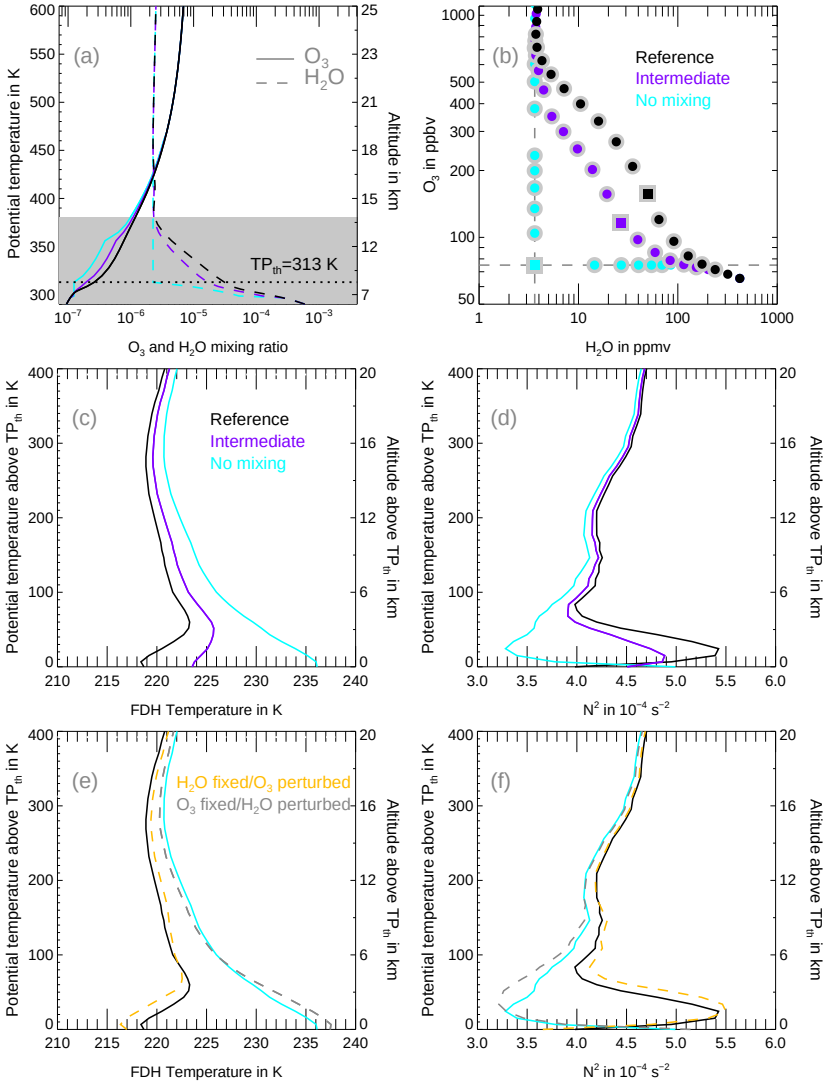

Figure 4.18: Panel (a): ECMWF mean vertical profiles of O_3 (solid lines) and H_2O (dashed lines) at 60^{o}N respective to different states of the atmosphere, i.e., non–mixed (cyan), mixed (black) and intermediate case (purple). Both the potential temperature in K and the altitude in km are shown with respect to the thermal tropopause ($\mathrm{TP_{th}} = 313\,\mathrm{K}\,, 9.09\,\mathrm{km}$). **Panel (b)**: Tracer correlations for profiles in different mixing states from panel (a). SPURT area is marked by gray shading (a) and dots bordered in gray (b). **Panel (c)**: Based on fixed dynamical heating (FDH) calculations resulting temperature profiles for the different mixing states above $\mathrm{TP_{th}}$. **Panel (d)**: Static stability N^2 according to the temperature profiles from panel (c). **Panels (e) and (f)**: FDH calculations, if one of the two trace gases is kept constant (O_3 (gray dashed) or H_2O (yellow dashed)).

$3.5\,\mathrm{km}$ ($60\,\mathrm{K}$) above the thermal tropopause is also evident in the mean ECMWF temperature (black line, panel (c)) together with a maximum in the static stability of $N^2 = 5.4 \cdot 10^{-4}\,\mathrm{s}^{-2}$ around $1.5\,\mathrm{km}$ ($25\,\mathrm{K}$) above the tropopause (black line, panel (d)). The area with the available SPURT data in the UT/LS is bordered in gray in panels (a) and (b). Hypothetical profiles for non–mixed conditions (cyan lines or dots) are constructed assuming the so–called 'L–shaped' tracer correlation (Pan et al., 2007b). The non–mixed H_2O profile decreases in the troposphere and is constant in the stratosphere ($\approx 4\,\mathrm{ppmv}$, consistent with the minimum of the mean H_2O vertical profile at $18\,\mathrm{km}$). The non–mixed O_3 profile is constant in the troposphere ($\approx 75\,\mathrm{ppbv}$) and increases in the stratosphere. The corresponding tracer correlation forms an 'L–shape' (cyan dots, panel (b)). Intermediate H_2O and O_3 profiles (purple lines, panel (a)) exhibit a mixing line in the area between the non–mixed and mixed reference profiles (purple dots, panel (b)). The intermediate and non–mixed profiles (purple and cyan lines) agree with the reference profiles (black line) in the stratosphere above $18\,\mathrm{km}$ and in the troposphere below 6 km.

The radiative effects due to the change of O_3 and H_2O from non–mixed (cyan line) to mixed reference concentrations (black line) are investigated. Sensitivity tests with the perturbed profiles of panel (a) are performed with the Reading narrowband radiative transfer model. The related FDH temperature profiles above the thermal tropopause $\mathrm{TP_{th}}$ are shown in panel (c). Above the tropopause the temperature increases throughout the column when the mixing degree is reduced. At the same time the temperature inversion decreases. An enhanced temperature above the tropopause remains as a net effect of the simultaneous perturbation of H_2O and O_3 according to a transition from a mixed to a non–mixed state. Panel (d) shows N^2 for the newly adjusted temperature profiles corresponding to non–mixed (cyan line) and intermediate mixed (purple line) H_2O and O_3 profiles. The perturbation of trace gas profiles in the tropopause region according to a transition from a mixed (black line) to non–mixed (cyan line) state reveals a successive decrease of N^2 the more strongly mixing is reduced. The TIL just above the tropopause vanishes in the case of non–mixed profiles. Above the tropopause where SPURT flights were performed the non–mixed profiles show a temperature increase of $18\,\mathrm{K}$ and an N^2 reduction of $2.1 \cdot 10^{-4}\,\mathrm{s}^{-2}$ compared to realistic mixed profiles.

A sole reduction of O_3 (H_2O) from the mixed to the non–mixed 'L–shaped' profile above the tropopause leads to a cooling (warming) in this region (panel (e)). The contribution of H_2O to the temperature change ($\approx 5 - 15\,\mathrm{K}$ up to $4 - 5\,\mathrm{km}$ above the tropopause) is larger than that of O_3 ($\approx 1 - 2\,\mathrm{K}$). The temperature decrease due to the O_3 perturbation is nearly the same up to $4 - 5\,\mathrm{km}$. The temperature lapse rate remains almost unchanged and there is nearly the same N^2 profile above the tropopause, especially up to $1.5\,\mathrm{km}$. A temperature inversion is also present for non–mixed O_3 profiles (dashed yellow line). In the case

of non–mixed H_2O profiles (dashed gray line) there is no inversion at all. The temperature inversion becomes stronger the more H_2O is enhanced toward the mixed reference profile. This suggests that H_2O plays a larger role in establishing the temperature inversion and the TIL structure than O_3. Panel (f) shows that the N^2 distribution in the case of non–mixed profiles (cyan line) up to $1.5\,\mathrm{km}$ above $\mathrm{TP_{th}}$ is mainly created by the change in H_2O (dashed gray line). This result contrasts with the conclusion of Randel et al. (2007b), who suggested that O_3 and H_2O play comparable roles in creating the inversion with opposing radiative effects in heating and cooling at slightly different altitude levels. The differences between these results and those of Randel et al. (2007b) are probably due to the differences in perturbing the trace gas profiles above the tropopause. This result underlines the importance of a consistent perturbation of O_3 and H_2O.

4.5 Upper–tropospheric dynamics related to the TIL and TFM branch

Within this thesis, so far, the TIL has been discussed in connection to the radiative forcing mechanisms in the UT/LS. However there are studies which motivate the TIL by dynamic mechanisms (see, Wirth, 2003; Birner, 2006; Son and Polvani, 2007). With model simulations based on the dry primitive equations without any radiation, Son and Polvani (2007) also obtained a TIL albeit it is not as sharp as in observations. They concluded that synoptic–scale balanced dynamics alone may not be sufficient to explain the quantitative features of the observed TIL and suggested that radiative processes can play an additional role for the maintenance of the TIL.

Wirth (2003) proposed the enhanced stability above the tropopause as a feature of anticyclonic upper–tropospheric flow expected from large–scale balanced dynamics. He analyzed profiles of N^2 in idealized axisymmetric baroclinic vortices, which were produced with the help of a PV inversion technique. His anticyclones were characterized by a sharp peak of N^2 above the tropopause, which implies a large sharpness of the tropopause. His cyclones showed only a smooth transition of N^2 across the tropopause. Wirth and Szabo (2007) argued that these features could be related to partitioning of a given PV anomaly into a static stability anomaly and a vorticity anomaly, which differ between cyclonic and anticyclonic anomalies. The extended studies of Wirth (2004) and Wirth and Szabo (2007) also show the TIL related to a primarily anticyclonic flow. The possible underlying mechanism for the tropopause sharpening related to anticyclones is described in Wirth (2004). Thus, the TIL could be the result of this anticyclonic influence in a time–averaged statistics.

Randel et al. (2007b) investigated the connection between upper–tropospheric anticyclonic activity and N^2 above the tropopause using high resolution GPS data. As expected from balanced dynamics they found a stronger TIL with a higher N^2 related to anticyclones than to cyclones. The TIL was present for all circulation types. Radiative transfer calculations led them to conclude that strong vertical gradients in both O_3 and H_2O near the tropopause contribute to the inversion.

The relationship between the tropopause structure, i.e., the sharpness of the tropopause, and the upper–tropospheric circulation is now explored for the time period of the SPURT campaigns. In particular, the upper tropospheric flow is divided into anticyclonic and cyclonic systems which are analyzed in connection to the TIL branch and for the first time to the TFM branch as observed during SPURT.

4.5.1 The relative vorticity

The cyclonic and anticyclonic systems in the upper troposphere can be identified with the relative vorticity ζ. The relative vorticity is a measure of the rotation of air in the atmosphere. For large–scale atmospheric flows the vertical component of the relative vorticity is important (Mohanakumar, 2008). It depends on the horizontal vorticity and in Cartesian coordinates it is given by

$$\zeta = \frac{\partial v}{\partial x} - \frac{\partial u}{\partial y}\,. \tag{4.17}$$

The meridional wind is given by v and the zonal wind by u. The derivative of v is determined in the meridional direction x and that of u in zonal direction y. In the northern hemisphere the regions of positive relative vorticity ($\zeta > 0$) are associated with cyclonic disturbances, those with negative relative vorticity ($\zeta < 0$) with anticyclonic activities. These relations are reversed in the southern hemisphere.

Similar as Randel et al. (2007b) the near–tropopause circulation is classified, i.e., the relative vorticity derived from the ECMWF data on the 200 hPa level is calculated. Figure 4.19 shows ζ in $10^{-5}\,\mathrm{s}^{-1}$ at 200 hPa on 27 April 2003. Largest positive (red color) and negative relative vorticity (blue color) is found at midlatitudes on both hemispheres associated with the cyclonic and anticyclonic weather systems, respectively. Poleward of 30° N, a typical coordinate for the location of the subtropical jet stream, cyclonic systems are dominant correspondent to the cyclonic side of the jet stream. Toward the equator on the anticyclonic side of the jet stream anticyclones are prevalent in the northern hemisphere.

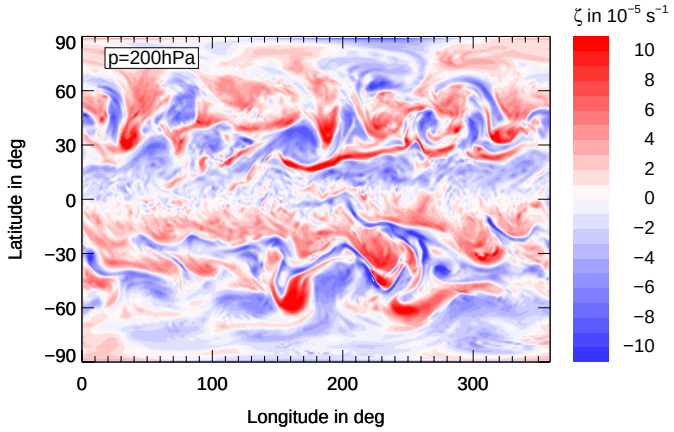

Figure 4.19: Relative vorticity ζ in $10^{-5}\,\mathrm{s}^{-1}$ at 200 hPa on 27 April 2003, calculated from ECMWF operational analysis at 12 UTC.

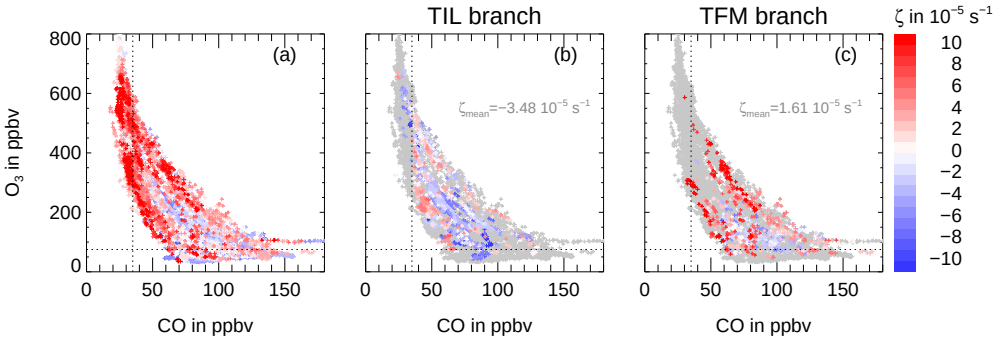

Figure 4.20: Relative vorticity ζ in $10^{-5}\,\mathrm{s}^{-1}$ at 200 hPa for the SPURT measurement positions within the mixing layer (panel (a)), the TIL branch (panel (b)) and the TFM branch (panel (c)). The mean values of the relative vorticity ζ_{mean} within the different branches are given in the respective panels.

4.5.2 Anticyclones and cyclones related to the TIL– and TFM branch

Within the mixing layer, the TIL– and TFM branch during SPURT (see section 4.2.4 for the definition of the branches), the relative vorticity at 200 hPa is calculated and interpolated on the latitudinal and longitudinal position of the measurements (Figure 4.20). Both the TIL–branch (panel (b)) and the TFM–branch (panel (c)) are not exclusively related to anticyclonic (blue color) or to cyclonic circulation systems (red color). The TIL branch is associated with

frequent anticyclonic activities and the TFM branch to frequent cyclonic activities. This is demonstrated by the negative mean value $\zeta_{mean} = -3.48 \cdot 10^{-5}\,\mathrm{s}^{-1}$ within the TIL branch and the positive value $\zeta_{mean} = 1.61 \cdot 10^{-5}\,\mathrm{s}^{-1}$ within the TFM branch. The mean values indicate that the TIL branch is related to substantially stronger anticyclones than the TFM branch to cyclones.

The relative vorticity is binned according to cyclonic and anticyclonic activities between –9 to $9 \cdot 10^{-5}\mathrm{s}^{-1}$ (Figure 4.21, top panels). Within the mixing layer a shift in the distribution of relative vorticity toward anticyclonic structures with a maximum data density around $\zeta = -5.0 \cdot 10^{-5}\,\mathrm{s}^{-1}$ is evident. This shift is even more pronounced within the TIL branch (panel (b)). The distribution of the relative vorticity within the TFM branch (panel c) is more homogeneous and a high data density is present over a large range of cyclonic values. Nevertheless, there is a bimodal distribution within the TFM branch, i.e., a peak at around $\zeta = -4 \cdot 10^{-5}\mathrm{s}^{-1}\,\mathrm{to}\,-6 \cdot 10^{-5}\mathrm{s}^{-1}$ and a second peak at $\zeta = 4 \cdot 10^{-5}\mathrm{s}^{-1}\,\mathrm{to}\,6 \cdot 10^{-5}\mathrm{s}^{-1}$. The high data density for strong anticyclonic structures within the TIL branch supports the hypothesis of Wirth (2003) that the inversion is related to anticyclonic activities. Nevertheless, there is an additional contribution of cyclonic structures associated with the TIL branch, albeit with a lower frequency compared to anticyclonic structures.

Figure 4.21 (middle panels) shows the mean height of the thermal tropopause (large filled diamonds), its corresponding standard deviation (small filled diamonds) and the mean height of the dynamical tropopause ($\mathrm{TP_{dyn}} = 2\,\mathrm{PVU}$) (large open diamonds) within each relative vorticity bin in the entire mixing layer (panel (d)), the TIL–branch (panel (e)) and the TFM–branch (panel (f)). The mean height of thermal tropopause is higher than the mean height of the dynamical tropopause at each relative vorticity bin within the entire mixing layer (panel (d)). The height of both tropopauses is decreasing from strong anticyclonic structures $\zeta = -9.0 \cdot 10^{-5}\,\mathrm{s}^{-1}$ toward zero relative vorticity and the distance between the two tropopauses is very small. With increasing cyclonic activity the height of $\mathrm{TP_{th}}$ remains nearly constant, almost slightly increasing, while the height of $\mathrm{TP_{dyn}}$ is still decreasing. Thus, the distance between both tropopauses is larger for cyclonic structures than for anticyclonic structures within the entire mixing layer. Similar to Randel et al. (2007b) an increasing height of the mean thermal tropopause with increasing strength of anticyclonic structures is evident. A selection of the mixing layer into the TFM branch and TIL branch shows that the height of $\mathrm{TP_{dyn}}$ and $\mathrm{TP_{th}}$ is decreasing both for anticyclonic and cyclonic structures within the TIL branch (panel (e)) and the TFM branch (panel (f)). The distance between $\mathrm{TP_{dyn}}$ and $\mathrm{TP_{th}}$ is larger within the TFM branch than within the TIL branch, where both tropopauses are very close to each other both for cyclonic and for anticyclonic structures. The distance between both tropopauses becomes larger with increasing relative vorticity within the TFM branch.

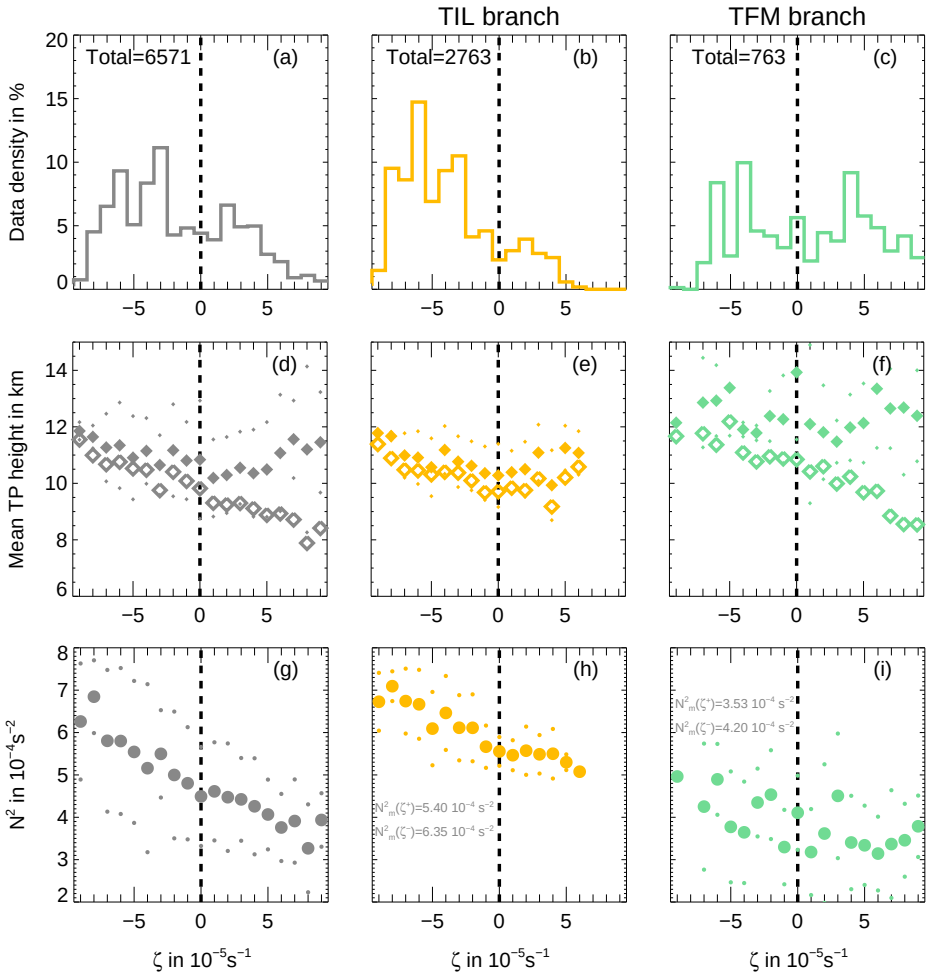

Figure 4.21: Data density of the relative vorticity ζ in $10^{-5}\,\mathrm{s}^{-1}$ at 200 hPa in the entire mixing layer (panel (a)), the TIL branch (panel (b)) and the TFM branch (panel (c)). The mean height of the thermal tropopause (large filled diamonds), the standard deviation (small filled diamonds) and the mean height of the dynamical tropopause (large open diamonds) (panels (d)–(f)) are shown. The mean static stability N^2 in $10^{-4}\,\mathrm{s}^{-2}$ at the SPURT measurement location within the three branches is also shown (panels (g)–(i)).

The reason for the higher thermal tropopause within the TFM branch than within the TIL branch may be due to sampling issues. Here, the TFM branch is most probably sampled by the SPURT flights in the vicinity of the jet streams. On the anticyclonic side of the subtropical jet stream a higher thermal tropopause is observed than at midlatitudes, where the TIL

branch is sampled during the SPURT flights. The jet streams are further related to secondary tropopauses, with a higher tropical thermal tropopause above a lower midlatitude tropopause (Randel et al., 2007a; Pan et al., 2009b). These double tropopauses are further related to a large difference between the thermal tropopause and the dynamical tropopause on the anticyclonic side of the jet stream. The mean distance between the thermal and dynamical tropopause is very small within the TIL–branch and is very large within the TFM–branch for each relative vorticity bin. This supports the definition of the TFM branch to select atmospheric areas, e.g., in the vicinity of jet streams, where the distance between the dynamical and thermal tropopause is largest. The large difference between the dynamical and thermal tropopause for strong cyclonic structures in the entire mixing layer but also in the TFM branch supports the separation of both tropopauses in strong cyclonic systems as discussed by Wirth (2000, 2001). They found a substantially larger difference between both tropopauses for cyclonic than for anticyclonic systems. In contrast, the TIL branch is associated with a smaller distance between the thermal and dynamical tropopause. This is also demonstrated by case studies shown in Figure 4.5 and Figure 4.6.

In the analysis of Randel et al. (2007b) anticyclones are related to a stronger inversion than cyclones. In order to analyze the SPURT data for this feature, Figure 4.21 (bottom panels) shows the mean static stability N^2 at the measurement positions within each relative vorticity bin (large dots) and the corresponding standard deviation (small dots) within the TIL–branch (panel (h)) and the TFM–branch (panel (i)). The mean static stability within the TIL branch is for each relative vorticity bin at 200 hPa higher than within the TFM branch. Within the TIL branch the static stability is decreasing with increasing relative vorticity for anticyclonic structures, for cyclonic structures the relative vorticity remains approximately constant and the mean value is lower than for anticyclonic structures. Within the TFM branch no clear relationship between static stability and relative vorticity at 200 hPa is observed, but the mean static stability for anticyclonic structures is also higher than for cyclonic structures within the TFM branch.

The mean height of thermal tropopause is higher than the mean height of dynamical tropopause both for each cyclonic and for each anticyclonic relative vorticity bin in the TFM and TIL branch (see panels (e) and (f)). This stands partly in contrast to Wirth (2000), who suggests that the dynamical tropopause lies above or below the thermal tropopause dependent on the upper tropospheric flow. In particular, the dynamical tropopause would be below the thermal tropopause in cases of smaller N^2 for cyclonic anomalies. Vice versa, for anticyclonic anomalies the dynamical tropopause would be above the thermal tropopause associated with a higher N^2. According to the analysis in Figure 4.21 a high mean static stability is related to a strong negative mean relative vorticity, i.e., it is related to anticyclonic

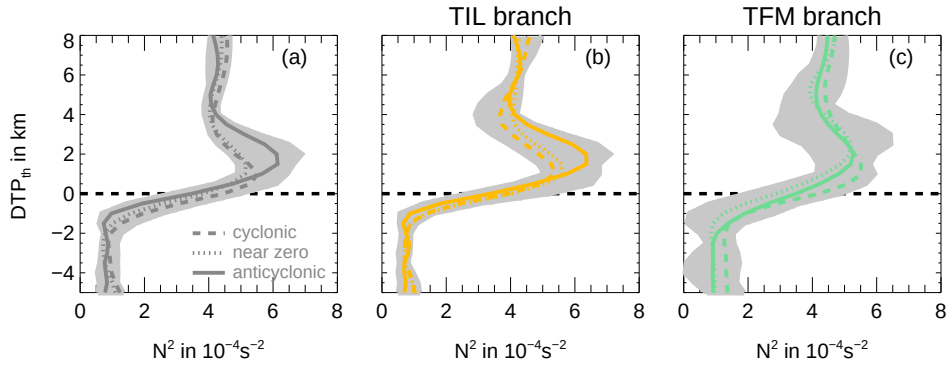

Figure 4.22: Mean vertical profiles of static stability N^2 relative to the thermal tropopause $\mathrm{DTP_{th}}$ in km for strong anticyclonic structures ($\zeta < -3 \cdot 10^{-5}\,\mathrm{s}^{-1}$), strong cyclonic structures ($\zeta > 3 \cdot 10^{-5}\,\mathrm{s}^{-1}$) and near–zero relative vorticity ($-3 \cdot 10^{-5}\,\mathrm{s}^{-1} < \zeta < 3 \cdot 10^{-5}\,\mathrm{s}^{-1}$) for the three different branches, mixing layer (panel (a)), TIL branch (panel (b)) and TFM branch (panel (c)). The shaded area marks the maximum and minimum mean relative vorticity at each vertical bin.

structures. At the same time there is a larger mean height of the dynamical tropopause for these anticyclonic structures compared to cyclonic structures in the respective branches. In connection to the static stability and the upper tropospheric flow the height of the dynamical tropopause may be understood with the definition of the dynamical tropopause. A single PVU value is used as global static value of the dynamical tropopause. The potential vorticity PV is the product of the absolute vorticity and the static stability, i.e., $PV \approx (\zeta + f) \cdot \frac{1}{\rho}\frac{\partial\theta}{\partial z}$. Thus, the dynamical tropopause contains changes in the dynamics, represented by the relative vorticity ζ, and in the thermal stratification, represented by the vertical potential temperature gradient $\frac{\partial\theta}{\partial z}$. Thus, an increase of ζ due to an intensification of cyclonic and anticyclonic activity at the dynamical tropopause must be balanced by a decrease in thermal stratification N^2 to keep the potential vorticity constant.

In Figure 4.21 (panels (g)–(i)) N^2 at the measurement positions is analyzed with the associated ζ at 200 hPa in that regions where the TIL was detected. In contrast, Randel et al. (2007b) selected their data according to cyclonic and anticyclonic systems and compared the vertical profiles of static stability for both circulation types. Especially the unclear relationship within the TFM branch between the static stability and the relative vorticity motivates the analysis of the full vertical profile of N^2 across the tropopause. In other words, panels (h) and (i) represent only one single level of these vertical profiles of static stability, where the measurement was performed. Consequently, the maximum of static stability in the vertical column may not be detected. Therefore, the mean vertical profiles of static stability relative

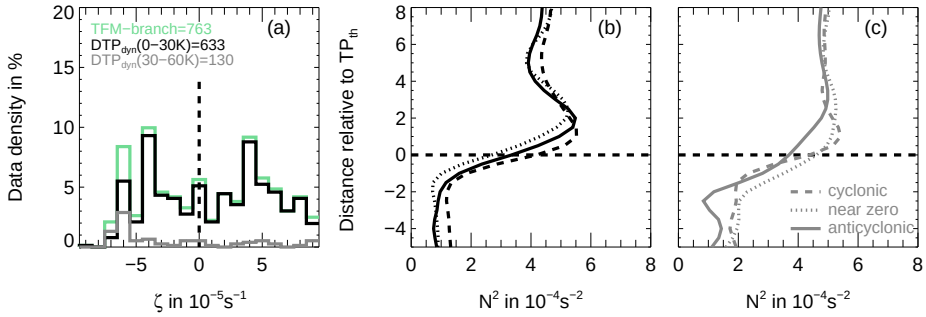

Figure 4.23: Selection of the TFM branch within 30 K above the dynamical tropopause (black lines) and between 30 to 60 K above the dynamical tropopause (gray lines). The data density within each relative vorticity bin (panel (a)) and the mean vertical profiles of static stability relative to the thermal tropopause for strong anticyclonic structures, strong cyclonic structures and near–zero relative vorticity ($\mathrm{DTP_{dyn}} = 0 - 30\,\mathrm{K}$ panel (b), $\mathrm{DTP_{dyn}} = 30 - 60\,\mathrm{K}$ panel (c)) are shown. The number of data points is given in the legend.

to the thermal tropopause are calculated for three different relative vorticity branches (Figure 4.22):

- strong anticyclonic structures ($\zeta < -3 \cdot 10^{-5}\,\mathrm{s}^{-1}$) (solid lines)
- near–zero relative vorticity ($-3 \cdot 10^{-5}\,\mathrm{s}^{-1} < \zeta < 3 \cdot 10^{-5}\,\mathrm{s}^{-1}$) (dotted lines)
- strong cyclonic structures ($\zeta > 3 \cdot 10^{-5}\,\mathrm{s}^{-1}$) (dashed lines)

Within the mixing layer (Figure 4.22, panel (a)) a stronger inversion is evident for anticyclonic structures than for cyclonic structures. The maximum of static stability above the thermal tropopause related to anticyclonic structures is around $1 \cdot 10^{-4}\,\mathrm{s}^{-2}$ higher than the maximum related to cyclonic structures with a slight difference in the height of the maximum N^2. Within the TIL branch (Figure 4.22, panel b) there is a stronger tropopause inversion for strong anticyclonic structures (solid line) than for strong cyclonic structures (dashed line). This feature is also observed with the help of high resolution GPS data by Randel et al. (2007b) and with ERA data by Birner et al. (2006). For anticyclonic structures the sharp maximum of static stability above the thermal tropopause is around $6.5 \cdot 10^{-4}\,\mathrm{s}^{-2}$ and larger than for cyclonic structures. The mean vertical static stability profile for near–zero relative vorticity (dotted line) also exhibits a sharp maximum above the tropopause which is similar to that of strong cyclonic structures. This implies that the TIL is also pronounced to vanishing or very low upper tropospheric circulation. In contrast, the TFM branch (Figure 4.22, panel c) exhibits a stronger inversion in the case of cyclonic structures (dashed line)

compared to anticyclonic structures (solid line). The strength of the inversion associated with the near–zero relative vorticity is also close to the strength of the inversion related to the strong anticyclonic structures.

Figure 4.23 shows the analysis of the relative vorticity for two different parts of the TFM branch. On the one hand, the part with a small distance between the thermal and dynamical tropopause, i.e., the SPURT measurement is taken close to the dynamical tropopause $\mathrm{DTP_{dyn}} = 0 - 30\,\mathrm{K}$ (black lines, panel (b)) and on the other hand, a larger distance between the two tropopauses, i.e., $\mathrm{DTP_{dyn}} = 30 - 60\,\mathrm{K}$ (gray lines, panel (c)). The strength of the temperature inversion is comparable for cyclonic structures and for anticyclonic structures within the $\mathrm{DTP_{dyn}} = 0 - 30\,\mathrm{K}$ part (panel (b)). However, the temperature inversion is still higher for cyclonic than for anticyclonic structures within the $\mathrm{DTP_{dyn}} = 30 - 60\,\mathrm{K}$ part (panel (c)). In particular, the inversion for the $\mathrm{DTP_{dyn}} = 0 - 30\,\mathrm{K}$ part is very similar to the entire TFM branch in Figure 4.22 (panel (c)). This is due to the large number of measurements close to the dynamical tropopause. In the case of the $\mathrm{DTP_{dyn}} = 30 - 60\,\mathrm{K}$ part, when the distance between the dynamical and thermal tropopause is largest, the strength of the inversion for cyclonic structures is similar to that of a smaller distance between the tropopauses, i.e., $\mathrm{DTP_{dyn}} = 0 - 30\,\mathrm{K}$. The analysis shows that strength of the inversion due to anticyclonic activities decreases with an increasing distance between the dynamical and the thermal tropopause. There is no sharp maximum and the static stability is very smooth and high over a larger vertical region up to 3 km above the thermal tropopause for anticyclonic structures (solid gray line, panel (c)). The inversion extends over a larger vertical distance and is very smooth. The distance between the two tropopauses is larger than 30 K most probably near secondary tropopauses associated with a jet stream. The weaker temperature inversion over a large vertical extension for anticyclonic structures (solid line, panel (c)) may result from an averaging over two different parts of high static stability on the anticyclonic side of the jet stream toward the equator. In that case the mean vertical profile of N^2 contains high static stability above the first thermal tropopause, associated with tropospheric intrusions as presented by Pan et al. (2009b). Above this layer an intermediate layer of lower N^2 is followed by a second layer of high N^2 above the secondary tropopause some kilometers above the first thermal tropopause. These two layers also contribute to the smooth vertical profile of N^2 in the case of anticyclonic activities for the $\mathrm{DTP_{dyn}} = 30 - 60\,\mathrm{K}$ part. The layered structure results in a larger vertical extent of the region with high static stability and there is no sharp maximum at a single altitude (Figure 4.22, panel (c)). On the cyclonic side an inversion still remains.

In contrast, the part of the TFM branch close to the dynamical tropopause, i.e., $\mathrm{DTP_{dyn}} = 0 - 30\,\mathrm{K}$ (panel (b)), reveals a sharp maximum of static stability for anticy-

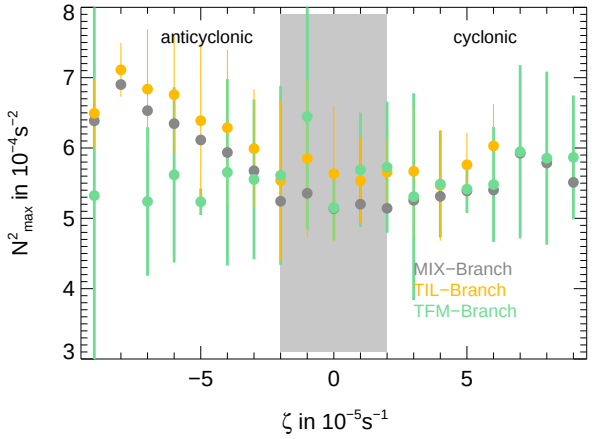

Figure 4.24: Maximum of the mean static stability at each relative vorticity bin for the entire mixing layer (gray symbols), the TIL branch (orange symbols) and the TFM branch (green symbols). The standard deviation is shown as vertical bars around the mean and the near–zero area of relative vorticity is marked by the gray shaded area.

clonic and cyclonic structures. There is a difference in the height of this maximum, which is close to the thermal tropopause in the case of cyclonic structures and farther away in the case of anticyclonic structures. A reason for the strength of the inversion also for cyclonic structures may be the structure of static stability in the vicinity of jet streams. The static stability is higher on the cyclonic (poleward) side of the jet streams than on the anticyclonic (equatorward) side of the jet streams at the same height. The high static stability on the poleward side of the jet streams is associated with the TIL, which extends from the midlatitudes to the subtropics probably related to tropopause breaks in the vicinity of jet streams. An example for such an event is given by Pan et al. (2007b) (their Figure 1).

As a measure of the strength of the inversion and thus of the sharpness of the tropopause the maximum of the static stability for each vertical N^2 profile is calculated. The mean of the maximum per relative vorticity bin is shown in Figure 4.24. Within the TIL branch (orange symbols) the strength of the inversion is larger for anticyclonic structures than for cyclonic structures. The strength of the inversion is decreasing with increasing relative vorticity for anticyclonic structures and remains approximately constant for cyclonic structures. This finding agrees with the results of Randel et al. (2007b) and supports the importance of anticyclones compared to cyclones for the strength of the TIL. Further, the behavior of the N^2_{max} in Figure 4.24 coincides with the behavior of N^2 within the TIL branch at the SPURT measurement positions (Figure 4.21 panel (h)). This suggests that the SPURT measurements

were largely performed within the TIL branch close to its maximum strength of N^2. Within the TFM branch (Figure 4.24, green symbols) no definite relationship between N^2 and ζ is observed. A fluctuating strength of the inversion around $N^2_{max} = 5.5 \cdot 10^{-4}\,\mathrm{s}^{-2}$ is evident for both cyclonic and anticyclonic structures.

4.6 Discussion of possible TIL maintenance processes

The link between the TIL and the mixing layer can be understood in the light of the activity of radiative and baroclinic forcing. Synoptic–scale baroclinic eddies in the extratropical tropopause region might lead to an isentropic transport of low O_3 and high H_2O mixing ratios from lower to higher latitudes (Figure 4.25, poleward yellow arrow). This isentropic transport from the troposphere at lower latitudes toward the stratosphere at higher latitudes across the tropopause causes mixing of tropospheric and lower stratospheric air at midlatitudes. Freshly mixed air masses near the subtropical jet stream (Figure 4.25, gray shaded area), are not necessarily related to high N^2 values. Lower N^2 are associated with the mixed regions in the vicinity of the jet stream (see Figure 4.5 and also 4.10 (c)). The atmospheric processes relevant for this fresh mixing are processes on the synoptic–scale, up to about 8 days (Figure 4.14). This estimate of the relevant time scale is similar to that by Dethof et al. (2000) who quantified the isentropic mass transport across the tropopause and found that the isentropic stratosphere to troposphere exchange is a fast process occurring on a daily time scale. This time scale is too short for radiative effects to have an impact which may lead to an enhanced N^2. This also may be the reason for the very low correlation between the mixing degree f_{mix} and a large N^2 within the TFM branch. After passing the TFM branch (Figure 4.25, gray shaded area) the freshly mixed air masses are transported isentropically (wavy black arrow) into the midlatitude lowermost stratosphere. At the same time, they are transported downward by the large scale Brewer–Dobson circulation (downward yellow arrow). Near the thermal tropopause (solid red line) an adjustment of the temperature occurs to the new trace gas concentrations because of the radiative balance in the atmosphere. A contribution to the temperature inversion and the TIL branch (orange shaded) may well be a consequence.

Thus, the TIL contains mixed air masses which have been a longer time in the lowermost stratosphere than the mixed air masses in the TFM branch. The temporal variance analysis suggests a rather seasonal time scale (Figure 4.14). Backward trajectory calculations with CLaMS from measurement points within the TIL show that the static stability 10 days before the measurement was also very high with no significant variability. These analyses suggest

a seasonal time scale necessary for the atmospheric radiative response to mixing of stratospheric and tropospheric air masses. Due to the radiative balance in the atmosphere the temperature has already adjusted to the new trace gas concentrations near the tropopause and a temperature inversion has developed with time (Figure 4.18 (c), black line). This demonstrates the evolution of N^2 from the non–mixed case to the intermediate case and finally to the mixed reference case (Figure 4.18 (d)). This hypothesized mechanism also closes the loop to the discussion by Birner (2006) according to which the strong stratification within the TIL and the large–scale horizontal mixing forces the air that has entered the TIL to stay within the TIL and to be mixed isentropically over large distances. This may provide the basis for the mixing layer to become a climatological feature and for the radiatively active tracers to force the TIL.

So far it has not been possible to identify a particular atmospheric process as the sole contributor to the formation and maintenance of the TIL. The fact that the temperature inversion is present for all circulation types, and also for near zero relative vorticity which implicates a very weak upper tropospheric circulation (see section 4.5.2), suggests an important additional forcing beyond balanced dynamics. This motivates the radiative study of this thesis and that of Randel et al. (2007b) that the radiation may be an important forcing mechanism in maintaining the TIL. Nevertheless, dynamic mechanisms (see e.g., Wirth, 2003; Birner, 2006; Son and Polvani, 2007) have also been proposed and may also be important for the TIL structure. To quantify the exact contributions of radiation and dynamics to the TIL, further model studies are needed in future, which need to consider both dynamics and radiation at the same time.

4.7 Results of this chapter

Based on aircraft measurements of CO and $\mathrm{O_3}$ during SPURT a new dimensionless parameter f_{mix} to quantify the mixing degree in the extratropical tropopause region is introduced. Using this parameter the relationship between the static stability N^2 and the mixing degree is investigated and a positive relation between these two above the tropopause is found, particularly in the TIL. This is consistent with the hypothesis that mixing contributes to the formation of the TIL as suggested by Birner (2006) and Randel et al. (2007b). The studies demonstrate that the TIL is detectable in high resolution ECMWF fields. This finding is in contrast to Birner et al. (2002) who argued that the TIL is not well represented in ERA–40 reanalysis data. This can be a consequence of different assimilation procedures used in the operational (4DVAR) and ERA–40 (3DVAR) data and of the different horizontal resolution of both data sets (T511 versus T159 for operational and reanalysis data, respectively).

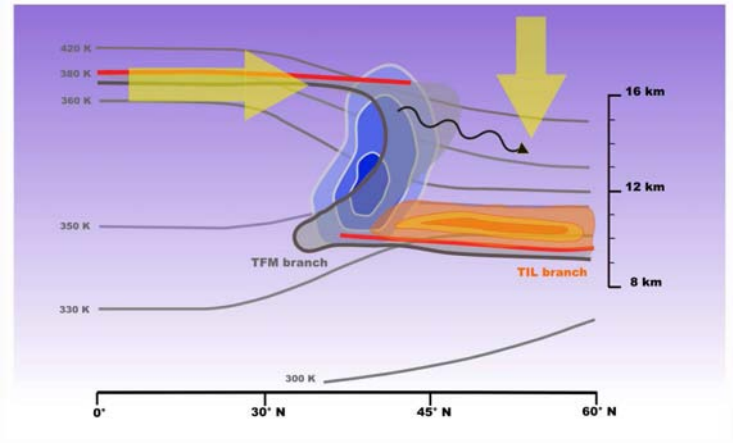

Figure 4.25: Instantaneous schematic of the possible dynamics and processes within the UT/LS between the equator and the pole leading to the formation of the TFM branch (gray shaded) and the TIL branch (orange shaded). The thermal tropopause (solid red line), the dynamical tropopause (solid gray line), the isentropes (light–gray lines) and the zonal velocity (blue shaded) are shown. Isentropic transport before the fresh mixing event in the TFM branch is indicated by the yellow horizontal arrow together with the isentropic transport of 'mixed air masses' as the wavy black arrow. The downward transport due to the Brewer–Dobson circulation is marked by the downward yellow arrow.

Studies with a radiation transport model confirm the hypothesis of Randel et al. (2007b) that radiative effects of O_3 and H_2O may contribute to the formation and maintenance of the mixing layer and the TIL. The new aspect of the analysis here is to emphasize the change in fixed dynamical heating (FDH) temperature and N^2 for profiles, which are perturbed consistently to represent a vanishing mixing (L–shaped O_3 and H_2O tracer correlation) in the UT/LS. The temperature inversion and the structure of the TIL do not appear for non–mixed mean vertical profiles of O_3 and H_2O. The temperature inversion is strengthened if the concentrations of O_3 and H_2O are enhanced because of mixing above the extratropical tropopause. Here, the influence of H_2O is more important than that of O_3 for the development of the temperature inversion and the TIL structure. There is only a small shift in temperature profile if O_3 is enhanced from a non–mixed to a mixed reference case at the tropopause. The same analysis applied to the POLARCAT–GRACE measurements yields the same results.

The analysis of this chapter suggests that the mixing layer contains, on the one hand, older air masses (TIL branch, Figure 4.10), with high values of N^2 possibly due to radiative adjustment. This part represents the TIL. On the other hand, there are freshly mixed air masses with lower N^2 values within the mixing layer (TFM branch, Figure 4.10), because of recent

intrusion processes due to the permeability or so–called midlatitude breaks associated with the jet streams.

The analysis of the relative vorticity ζ at 200 hPa associated with the TIL branch and the TFM branch during SPURT reveals that both branches are related to both anticyclonic and cyclonic upper tropospheric dynamics. The TIL branch is biased to the anticyclonic activity and is characterized by a sharper tropopause and a larger N^2 maximum above the tropopause in connection to this anticyclonic activity. This feature supports earlier studies of Randel et al. (2007b) and Birner et al. (2002), but also the use of ECMWF operational data to represent the observed relation between anticyclonic activity and the TIL in the tropopause region. In contrast, the TFM branch is related to a larger sharpness of the tropopause and thus a larger maximum of N^2 above the tropopause in the case of cyclonic activity compared to anticyclonic activity. The maximum of N^2 within the TFM branch is smaller and the sharpness of the tropopause is decreased for a subsample of the TFM branch with measurements in regions with a large difference between the thermal and the dynamical tropopause ($\mathrm{DTP_{dyn}} = 30 - 60\,\mathrm{K}$).

Chapter 5

A new diagnostic for the location of the jet cores

The thermal tropopause and the dynamical tropopause are not identical and in specific situations there may be significant differences. The dynamical tropopause is defined as a surface of constant potential vorticity, which is used instead of the vertical temperature gradient as the defining variable. The potential vorticity (PV) is a quantity proportional to the product of the vertical component of absolute vorticity and static stability, i.e.,

$$PV = (\zeta + f) \cdot \left[-g \frac{\partial \theta}{\partial p} \right] \tag{5.1}$$

with ζ the relative vorticity and f the planetary vorticity. The PV contains both dynamic (vorticity) and thermodynamic (potential temperature) properties and is a conserved quantity in the absence of diabatic heating or cooling and frictional forces (Ertel, 1942). The PV threshold between the troposphere and the stratosphere which defines the dynamical tropopause is taken as a positive or a negative value, giving surfaces located in the northern or southern hemisphere, respectively. To define a global tropopause, these two PV surfaces are connected by another type of surface near the equator, where the PV is close to zero. A constant potential temperature surface (Mohanakumar, 2008) is well suited for this purpose. Usually the 380 K isentropic surface is taken as tropopause in the tropics (see, e.g. Konopka et al., 2007; Fueglistaler et al., 2009).

There is no universally used PV value for the dynamical tropopause, but the most common choice is the 2 PVU surface (1 PVU=$10^{-6}\,\mathrm{m^{-2}\,s^{-1}\,K\,kg^{-1}}$, standard potential vorticity unit) (e.g., Holton et al., 1995; Wirth, 2000; Hoor et al., 2005; Pan et al., 2007a; Kunz et al., 2008). This value is also employed in this thesis for the dynamical tropopause. Hoerling et al. (1991) suggested the 3.5 PVU isoline as the optimal value for tropopause analysis outside the tropics.

The dynamical tropopause in Birner et al. (2002) was defined by this value. However, a particular value may not be appropriate for the entire extratropics. Figure 5.1 shows the zonal and meridional variability of the potential vorticity at the thermal tropopause on 27 April 2003. Here, the PV varies roughly between 0.5 PVU and 7 PVU at the thermal tropopause between the equator and the pole. The typical values of the PV at the thermal tropopause increase toward the equator and are definitely larger than 2 PVU at lower latitudes (e.g., $30^\circ\,\mathrm{N}$, black dots). As an alternative, Randel et al. (2007a) used a series of PV isolines (1–4 PVU) in their studies to indicate the approximate location of the dynamical tropopause. Kunz et al. (2009) deduced the mean PV at all thermal tropopause heights at the SPURT measurement locations to $\mathrm{PV}_{\mathrm{dyn}}^{\mathrm{mean}} \approx 4\,\mathrm{PVU}$ (see also Chapter 4.2.4). This mean value is definitely greater than the often used value of $\mathrm{TP}_{\mathrm{dyn}} = 2\,\mathrm{PVU}$.

One possibility of generalizing and determining the dynamical tropopause in a more physical manner, instead of using an ad hoc fixed PV value for the entire hemisphere, is the use of the isentropic gradient of PV (Hoskins et al., 1985). Here, the distribution of the extratropical PV on isentropic surfaces is of interest. The quasi–latitudinal gradient of PV on these isentropic surfaces is sharpest across the jet streams separating the troposphere from the stratosphere. These PV gradients are maximized near the jet cores and serve as barriers to cross–tropopause eddy transport (McIntyre and Palmer, 1984; Juckes and McIntyre, 1987; Holton et al., 1995). Haynes and Shuckburgh (2000b) used this transport barrier characteristic and defined a new tropopause using the minimum value of effective diffusivity on each isentropic surface. Thus, it is intended to use the horizontal isentropic PV gradients as an indicator for the transport barriers and the extratropical tropopause which is a more fundamental and general definition than one based on a particular value of PV or a particular value of lapse rate.

An analysis of the PV gradient on isentropic surfaces and thus a definition of an alternative tropopause based on these isentropic PV gradients is performed concerning the following questions:

- What is the PV distribution at the location of the sharpest isentropic PV gradient associated with the jet streams? To answer this question the zonal and time mean PV distribution at the maximum gradient of PV with equivalent latitude will be presented to indicate which PV value may represent the dynamical tropopause.

- Is there any seasonal dependence of the thermal stratification, i.e., the static stability N^2, on isentropes across the jet streams? Is the thermal stratification also an indicator of the barrier concerning a mixing across the jet streams? For this purpose, N^2 will be analyzed on isentropes relative to the jet cores in connection with $\mathrm{O_3}$–$\mathrm{H_2O}$ trace gas correlations.

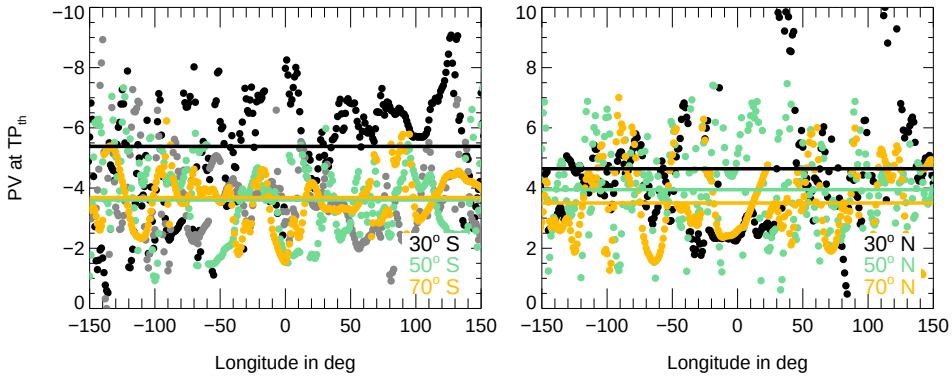

Figure 5.1: Meridional and zonal variability of the PV at the thermal tropopause depending on different geographical latitudes, i.e., 30° (black), 50° (green) and 70° (orange) in the southern hemisphere (left–hand panel) and in the northern hemisphere (right–hand panel) on 27 April 2003. The mean PV at $\mathrm{TP_{th}}$ is marked by solid lines for the different latitudes.

5.1 The isentropic potential vorticity gradient

The isentropic gradient of the PV distribution is established as a diagnostic to determine the edge of the polar vortex (Nash et al., 1996; Steinhorst et al., 2005). Nash et al. (1996) developed an objective criterion to find the location of the edge of the polar vortex as well as the dates of its onset or breakup. The PV distribution is determined on equivalent latitudes and the gradient of PV with equivalent latitude is calculated. They define the vortex edge to be located at the maximum of the product between the gradient of PV and the zonal wind velocity on isentropes. The boundary region of the vortex is defined between the convex and concave curvature in the PV distribution surrounding the edge. In the following, a method similar to the so–called Nash–criterion is developed to determine the core of the jet stream as well as its boundaries on isentropes. These boundaries include the meandering shape of the jet stream associated with breaking and splitting into different parts.

5.1.1 Determination of the jet core and boundaries

On an isentropic surface the gradient of PV is strongest across the jet streams separating the troposphere at lower latitudes from the stratosphere at higher latitudes. In both hemispheres, the absolute value of PV increases from the equator toward the pole. Similar to the polar vortex diagnostic of Nash et al. (1996), the PV values are projected onto an equivalent latitude area. The latitudes on this map are referred to as equivalent latitudes φ_e, which are inferred from the PV distribution on isentropes (Butchart and Remsberg, 1986). First, the ECMWF

data on pressure levels are interpolated on isentropic vertical levels θ between $300\,\mathrm{K}$ and $380\,\mathrm{K}$. For each isentrope the area enclosed by a PV contour in a hemisphere is calculated and transformed to a circle with the same area centered at the pole. Here, the equivalent latitude is the distance in degrees of latitude from the equator to this circle, and is given by

$$\varphi_e = \arcsin\left(\frac{1 - A(PV)}{2\pi \cdot r^2}\right) . \tag{5.2}$$

The quantity r is the radius of the Earth and $A(PV)$ is the area enclosed by the PV contour. The equivalent latitudes φ_e calculated according to Equation 5.2 have to be projected onto the original $1^\circ\,\mathrm{lat} \times 1^\circ\,\mathrm{lon}$ grid on the particular isentropes. The determination of the jet core $J_c(\theta)$ and the poleward and equatorward jet boundaries $J_b(\theta)$ on the isentropic surfaces θ is described in the following and is discussed for the case study on 27 April 2003 as an example (Figure 5.2).

1. For each isentrope θ, the equivalent latitudes $\varphi_e(\phi, \lambda, \theta)$, with ϕ the geographical latitude and λ the geographical longitude, are binned. The bin size of $\varphi_e(\phi, \lambda, \theta)$ is 1°, which is identical to the horizontal resolution of the ECMWF data used. The zonal mean in the φ_e–space of all desired atmospheric variables, e.g., potential vorticity PV and horizontal wind velocity $|\mathrm{u}| = \sqrt{u^2 + v^2}$, is calculated. Note that according to the definition of the equivalent latitudes, PV is the same for each equivalent latitude bin. Figure 5.2 shows the PV distribution (panel (a)) and the horizontal velocity $|\mathrm{u}|$ (panel (e)) for four different isentropes (300 K–360 K) against the equivalent latitude φ_e in the northern hemisphere on 27 April 2003. The PV distribution on the single isentropes has an 'S' shape. Despite an offset in the absolute values the PV distribution roughly resembles the distribution of the mathematical function $\mathrm{f(x)} = \arctan(\mathrm{x})$ (Figure 5.3, black line), which increases from negative values x toward positive values x with a point of inflection at $\mathrm{x} = 0$.

2. The gradient of the potential vorticity with equivalent latitude $\frac{\partial PV(\varphi_e,\theta)}{\partial \varphi_e}$ as well as the product with the horizontal wind velocity $\frac{\partial PV(\varphi_e,\theta)}{\partial \varphi_e} \cdot |\mathrm{u}|$ are calculated for each isentrope and hemisphere (Figure 5.2, panels (b) and (f)). The gradient $\frac{\partial PV(\varphi_e,\theta)}{\partial \varphi_e}$, i.e., the first derivative of PV, is shown in panel (b). Figure 5.3 shows the first derivative $\mathrm{f^I(x)}$ (orange line) of the function $\mathrm{f(x)}$, which shows a maximum where $\mathrm{f(x)}$ has its point of inflection. $\frac{\partial PV(\varphi_e,\theta)}{\partial \varphi_e}$ has a maximum at the point of inflection of the PV distribution. All fields are smoothed with a $\varphi_e = 5^\circ$ wide running mean to remove multiple peaks which do not represent the real jet core.

3. For each isentrope and hemisphere the jet core $J_c(\theta)$ is defined as the location of the

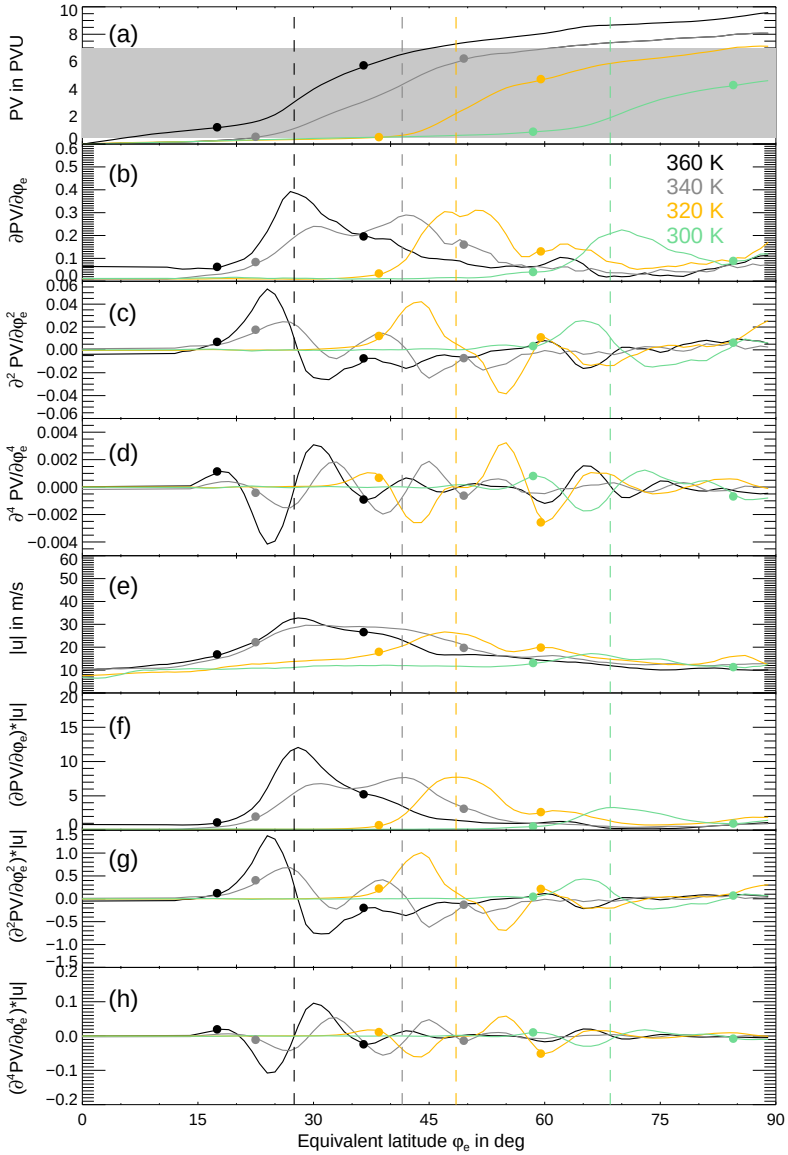

Figure 5.2: Distribution of the PV on four different isentropes 300 K (green), 320 K (gold), 340 K (gray) and 360 K (black) against the equivalent latitude in the northern hemisphere for 27 April 2003 (panel (a)). The gradient of PV, i.e., the first derivative of the PV, on these isentropes (panel (b)), the second derivative of the PV (panel (c)), the fourth derivative of the PV (panel (d)) and the horizontal velocity (panel (e)) are shown. The product of the horizontal velocity with the gradient of PV (panel (f)), with the second derivative (panel (g)) and the fourth derivative (panel (h)) are also shown. The jet cores $J_c(\theta)$ are shown as vertical dashed lines and the boundaries $J_b(\theta)$ as the two dots in the same color for each isentrope.

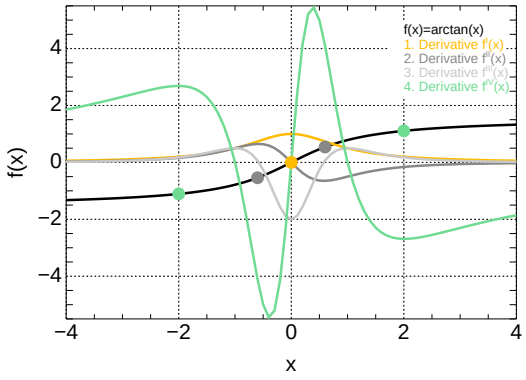

Figure 5.3: Distribution of $\mathrm{f(x) = arctan(x)}$ (black line) and the first four derivatives $\mathrm{f^{I}(x)}$ (orange line), $\mathrm{f^{II}(x)}$ (dark–gray line), $\mathrm{f^{III}(x)}$ (light–gray line) and $\mathrm{f^{IV}(x)}$ (green line). The slope of $\mathrm{f(x)}$ is largest where $\mathrm{f^{I}(x)}$ has a maximum. This maximum as representing the jet core $J_c(\theta)$ (orange dot at $\mathrm{f(x)}$). The slope of $\mathrm{f(x)}$ monotonically decreases in both directions of the jet core toward zero. The slope is sufficiently steep where $\mathrm{f^{IV}(x)}$ has local extrema which are defined as representing the jet boundaries $J_b(\theta)$ (green dots at $\mathrm{f(x)}$).

highest potential vorticity gradient, constrained to the vicinity of the jet streams where the wind velocity is very high. In this definition, the jet core $J_c(\theta)$ on the different isentropes is given by

$$J_c(\theta) = \max\left(\frac{\partial PV(\varphi_e,\theta)}{\partial \varphi_e} \cdot |\mathrm{u}|(\varphi_e,\theta)\right) \tag{5.3}$$

This means that the jet core $J_c(\theta)$ is defined as the maximum of the product between the PV gradient and the horizontal velocity (Figure 5.2, panel (f)). In contrast to Nash et al. (1996), who used the zonal wind velocity u for the determination of the vortex edge, the horizontal velocity $|\mathrm{u}|$ is used for the determination of the jet core. This horizontal velocity contains both the meridional and the zonal velocity components and thus represents the meandering shape of the jet streams. Figure 5.2 shows the jet core $J_c(\theta)$ as a vertical dashed line for each isentrope. There may be multiple peaks in the distribution of the PV gradient and the horizontal wind velocity, e.g., the distribution of both fields on the 320 K isentrope (orange lines, panels (b) and (e)). Some of these other peaks, which do not correspond to the real jet core, may also be large, but usually they appear only in one distribution and not in both. However, at the true jet core both distributions have strong peaks and the product of the two distributions reveals a clear maximum (panel (f)). This motivates the use of the product between the horizontal wind velocity and the PV gradient as a criterion for the determination of the jet core.

4. The jet core $J_c(\theta)$ is determined for each isentrope θ, whereby the following restrictions are implied:

   - Middle world isentropes, i.e., isentropes partly within the troposphere and stratosphere, intersecting the thermal tropopause: $300\,\mathrm{K} < \theta < 380\,\mathrm{K}$. These surfaces lie in the troposphere at lower latitudes and in the stratosphere at higher latitudes.
   - Non–realistically large gradients may exist in the vicinity of the poles and at the equator. Thus, the equivalent latitude space for the determination of $J_c(\theta)$ is restricted to: $5^\circ < |\varphi_e| < 85^\circ$
   - There is a large variability of potential vorticity at the thermal tropopause (Figure 5.1). Therefore, the PV range where the jet cores are diagnosed is restricted to: $0.5\,\mathrm{PVU} < |PV(\varphi_e, \theta)| < 7\,\mathrm{PVU}$ (see gray shaded area in Figure 5.2, panel (a)).

5. Jet streams are neither continuous nor circumpolar. They may start, stop, split into two or more parts, combine into one stream, or flow in various directions. Thus, the jet stream typically has a meandering shape. Therefore, jet boundaries $J_b(\theta)$ poleward and equatorward of the jet core are defined for each isentrope and hemisphere. The original Nash–criterion (Nash et al., 1996) defines the boundary region between the local maximum convex and concave curvature of the PV distribution surrounding the vortex edge. These extrema are defined by the second derivative of the PV distribution, see also $\mathrm{f^{II}(x)}$ (dark–gray line in Figure 5.3). For this purpose, the second derivative of the PV is calculated (Figure 5.2, panel (c)) and the maximum convex or concave curvature is determined by its product with the horizontal velocity, i.e,

$$\frac{\partial^2 PV(\varphi_e, \theta)}{\partial \varphi_e^2} \cdot |\mathrm{u}|(\varphi_e, \theta)\,. \tag{5.4}$$

   The distribution of the second derivative multiplied by the horizontal velocity on each isentrope is also shown in Figure 5.2 (panel (g)). After the determination of the exact latitude of the extrema of the second derivative, the fourth derivative of the PV distribution is also calculated (panel (d)) and is again multiplied by the horizontal wind velocity (panel (h). The local maximum convex and concave curvature of this fourth derivative of the PV multiplied by the wind velocity, i.e.,

$$\frac{\partial^4 PV(\varphi_e, \theta)}{\partial \varphi_e^4} \cdot |\mathrm{u}|(\varphi_e, \theta)\,, \tag{5.5}$$

   defines $J_b(\theta)$, the jet boundaries on isentropes. The fourth derivative $\mathrm{f^{IV}(x)}$ of the function $\mathrm{f(x)}$ (green line in Figure 5.3) shows these extrema at the locations where the slope

of $\mathrm{f(x)}$ approaches zero (see green dots in Figure 5.3). The jet boundaries $J_b(\theta)$ determined by the distribution of the fourth derivative of the PV distribution are highlighted as the two dots poleward and equatorward of the jet core $J_c(\theta)$ (dashed lines) in Figure 5.2. The jet boundaries $J_b(\theta)$ are searched outside an interval of $\varphi_e = \pm 3^\circ$ around the jet core $J_c(\theta)$.

In the following, the jet boundaries on isentropes are determined according to this fourth derivative of the PV (see Equation 5.5), which matches the meandering shape of the jet streams at the midlatitudes and subtropics in a more appropriate manner than the second derivative of the PV (see Equation 5.4) as used by Nash et al. (1996). Further, the extrema of the fourth derivative of the gradient of PV with equivalent latitude are in the regions where the PV and the gradient of PV with equivalent latitude are quite high enough. This is also demonstrated by the arcus tangens example in Figure 5.3. The extrema of the fourth derivative of $\mathrm{f(x)}$ (green dots, Figure 5.3) are in regions with a sufficiently steep first derivative $\mathrm{f^I(x)}$.

Figure 5.4 (top panels) shows the horizontal velocity together with the jet cores $J_c(\theta)$ (white) and the boundaries $J_b(\theta)$ (black) as determined through the procedure outlined above for different isentropes between 300 K and 340 K. The jet cores move toward the equator with increasing height of the isentropes. The jet cores matches the part of the largest wind velocity combined to a large PV gradient on this isentrope and the meandering shape of the jet stream is bordered by the jet boundaries. It is possible that two different jet streams, e.g., the subtropical jet stream and the polar jet stream, are combined on a particular isentrope. In such a case, the jet core represents the stronger jet stream of the two, but the weaker one is contained in the region within the jet boundaries.

The static stability N^2 (middle panels) on the different isentropes differs between the tropospheric part at lower latitudes and stratospheric part at higher latitudes of the isentrope. Toward the equator outside the first jet boundary there are typical tropospheric values of a low static stability around $N^2 = 1.0 \cdot 10^{-4}\,\mathrm{s}^{-2}$. Poleward of the jet boundary a typically high static stability of the entire stratosphere is evident around $N^2 = 4.0 \cdot 10^{-4}\,\mathrm{s}^{-2}$. This different behavior in thermal stratification supports the ability of the present method to determine the jet cores and their boundaries and thus to separate the troposphere from the stratosphere. Even the TIL is seen at $\theta = 320\,\mathrm{K}$ and $\theta = 340\,\mathrm{K}$ poleward of the jet boundary $J_b(\theta)$, with values around $\mathrm{N^2} = 6.0 \cdot 10^{-4}\,\mathrm{s}^{-2}$. The TIL is part of the stratospheric area, i.e., mainly outside the branch between the two jet boundaries. This area between the jet boundaries contains air masses of intermediate static stabilities around $\mathrm{N^2} = 3.0 \cdot 10^{-4}\,\mathrm{s}^{-2}$. These are the typical values of the freshly mixed air masses within the so–called TFM branch

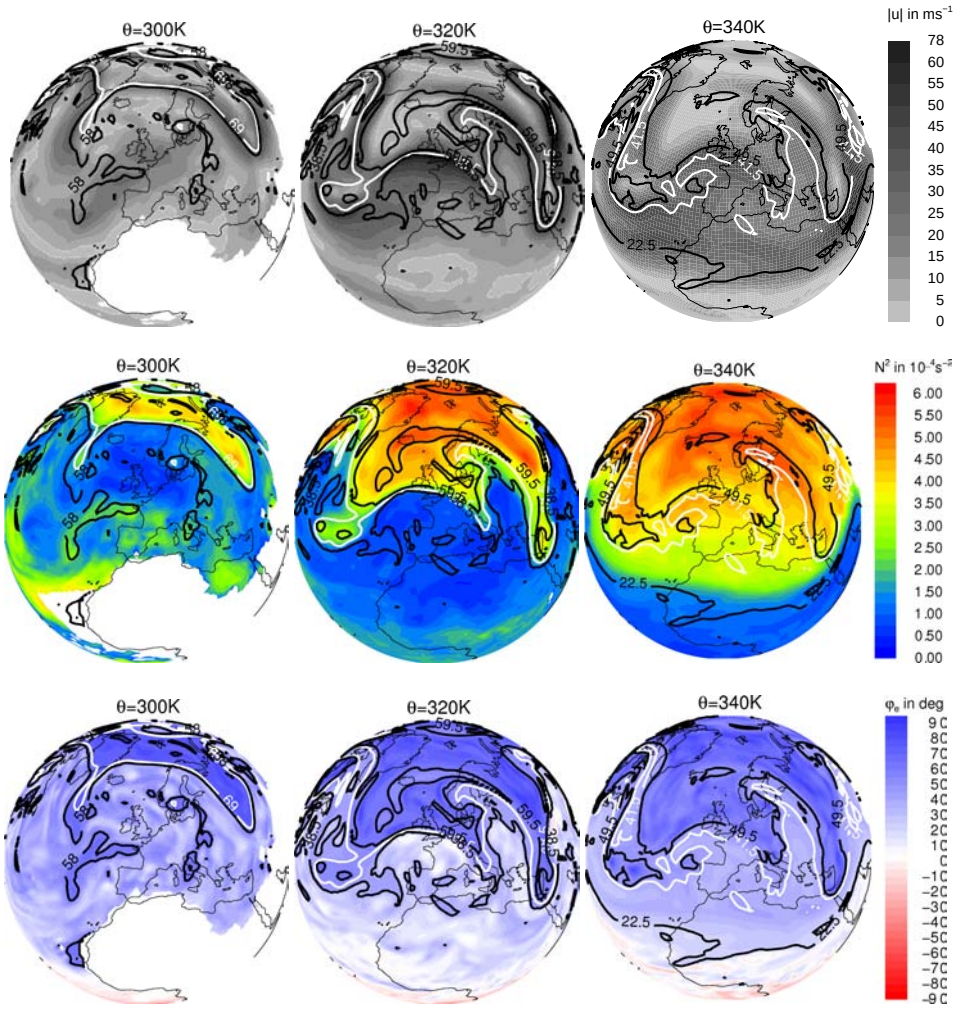

Figure 5.4: Horizontal wind velocity $|\mathrm{u}|$ in $\mathrm{m\,s^{-1}}$ (top panels), static stability N^2 in $10^{-4}\,\mathrm{s^{-2}}$ (middle panels) and equivalent latitude φ_e (bottom panels) on 27 April 2003 for the 300 K isentrope (left–hand column), the 320 K isentrope (middle column) and the 340 K isentrope (right–hand column). The jet core $J_c(\theta)$ (white) and the jet boundaries $J_b(\theta)$ (black) are shown.

(see Figure 4.9). Therefore, this gives additional support for the determined jet cores and the corresponding boundaries. The location of the jet cores (Figure 5.4, white lines) supports the idea that transport processes between the troposphere and the stratosphere occur within the TFM branches in the vicinity of the jet streams related to a static stability lower than within

the entire stratosphere, but at the same time higher than within the entire troposphere. The jet boundaries $J_b(\theta)$ divide the isentropic surface into three areas, a stratospheric area, a tropospheric area and into an area close to the jet stream, which is especially influenced by fresh mixing events. The equivalent latitude φ_e map projection shows three different air masses relative to the jet boundaries $J_b(\theta)$ (see Figure 5.4, bottom panels). The area between the jet boundaries contains air masses specific to the geographical region of the jet stream. Toward the pole the equivalent latitude is higher and describes the stratospheric air masses and toward the equator the equivalent latitude is lower typical for tropical air masses.

5.1.2 The PV gradient tropopause

The gradient of PV on isentropes is maximized across the jet streams and separates the troposphere from the stratosphere with different characteristics in thermal stratification (Figure 5.4). Therefore, the gradient of PV makes it possible to propose an alternative definition of the tropopause, the location of the 'tropopause barrier', which is not based on a particular value of the PV. PV values for defining the location of the dynamical tropopause are often chosen in an ad hoc manner and different values are used in the literature. In contrast, the definition of the dynamical tropopause as proposed in the following depends on the isentropic gradient and represents the tropopause as a dynamical transport barrier at the jet streams. In the following, this new tropopause is introduced and referred to as the *PV gradient tropopause* $\mathrm{TP}_{\mathrm{gradPV}}$. The determination of $\mathrm{TP}_{\mathrm{gradPV}}$ is performed using the locations of the jet cores $J_c(\theta)$ and the jet boundaries $J_b(\theta)$, originally calculated as a function of equivalent latitude φ_e and potential temperature θ. The height of $\mathrm{TP}_{\mathrm{gradPV}}$ in potential temperature is calculated for each latitude and longitude as described in the following:

1. The jet core $J_c(\theta)$ and the corresponding jet boundaries $J_b(\theta)$ have to be determined on each isentrope and hemisphere as described above in subsection 5.1.1.

2. For each latitude ϕ and longitude λ position the equivalent latitude on all isentropes θ is compared with the respective equivalent latitude of the jet cores $J_c(\theta)$ representative of the isentropes. For this purpose, the difference between the equivalent latitude at a latitude–longitude position with the equivalent latitude of $J_c(\theta)$ is calculated for each isentrope. Then the PV gradient tropopause $\mathrm{TP}_{\mathrm{gradPV}}$ within the latitude ϕ and longitude λ column containing all isentropes (denoted as '$\cdot$' in the following formula) is defined as the isentropic level θ, where the difference is minimal, i.e.,

$$\mathrm{TP}_{\mathrm{gradPV}}(\phi,\lambda) = \min(|\varphi_e(\phi,\lambda,\cdot) - J_c(\cdot)|) \tag{5.6}$$

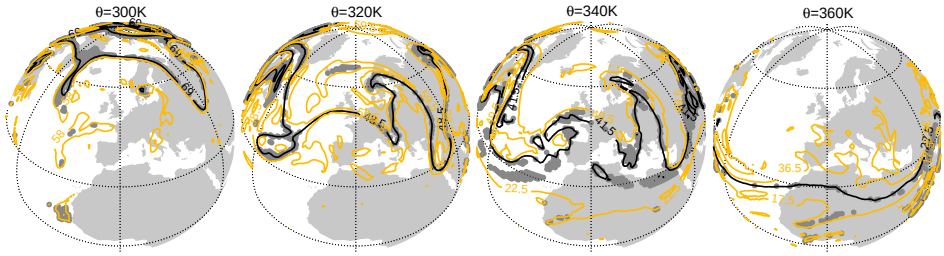

Figure 5.5: The PV gradient tropopause $\mathrm{TP}_{\mathrm{gradPV}}$ (dark gray dots) on different isentropes between 300 K and 360 K on 27 April 2003 over the European region. The jet cores $J_c(\theta)$ (black line) and the jet boundaries $J_b(\theta)$ (orange lines) are additionally shown.

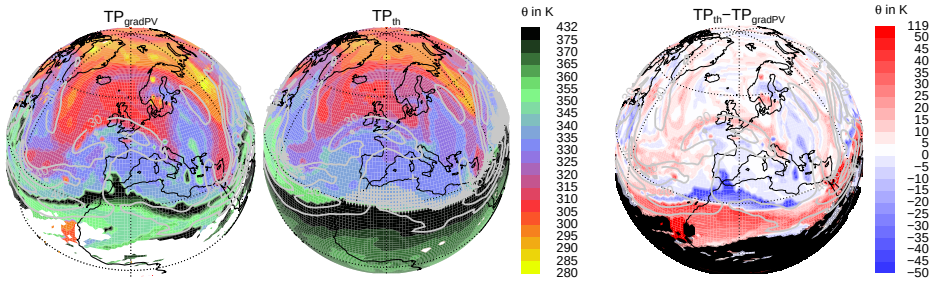

Figure 5.6: Potential temperature at the PV gradient tropopause $\mathrm{TP}_{\mathrm{gradPV}}$ (left–hand panel) and at the thermal tropopause $\mathrm{TP}_{\mathrm{th}}$ (middle panel) in K on 27 April 2003 and the potential temperature difference between both tropopauses (right–hand panel). The horizontal velocity on the 340 K isentrope is gray solid and the double tropopauses are marked with gray crosses (middle panel). Areas with missing $\mathrm{TP}_{\mathrm{gradPV}}$ are black (right–hand panel).

Here, the equivalent latitude $\varphi_e(\phi, \lambda, \theta)$ is restricted to the area between the jet boundaries $J_b(\theta)$ on the single isentropes to find the correct PV gradient tropopause. The poleward jet boundary for isentropes $\theta < 300\,\mathrm{K}$ is sometimes not resolved. In this case, the $\varphi_e(\phi, \lambda, \theta)$ is restricted to the equatorward jet boundary $J_b(\theta)$ and the jet core $J_c(\theta)$.

Figure 5.5 shows this PV gradient tropopause $\mathrm{TP}_{\mathrm{gradPV}}$ (gray area) on different isentropes on 27 April 2003 above the European region. The $\mathrm{TP}_{\mathrm{gradPV}}$, which lies on each isentrope θ within the jet boundaries $J_b(\theta)$, moves toward the equator with increasing height of the isentropes. For each isentrope a good agreement with the jet core (solid black line) is found, thus supporting the method presented here of determining the PV gradient tropopause as a function of the geographical latitudes and longitudes from the equivalent latitudes of the jet cores on the isentropes.

Figure 5.6 shows the height of $\mathrm{TP}_{\mathrm{gradPV}}$ (left–hand panel) in comparison to the thermal tropopause $\mathrm{TP}_{\mathrm{th}}$ (middle panel) for the same day. The difference (right–hand panel) between both tropopauses is greatest in the subtropics. Especially in the vicinity of the double

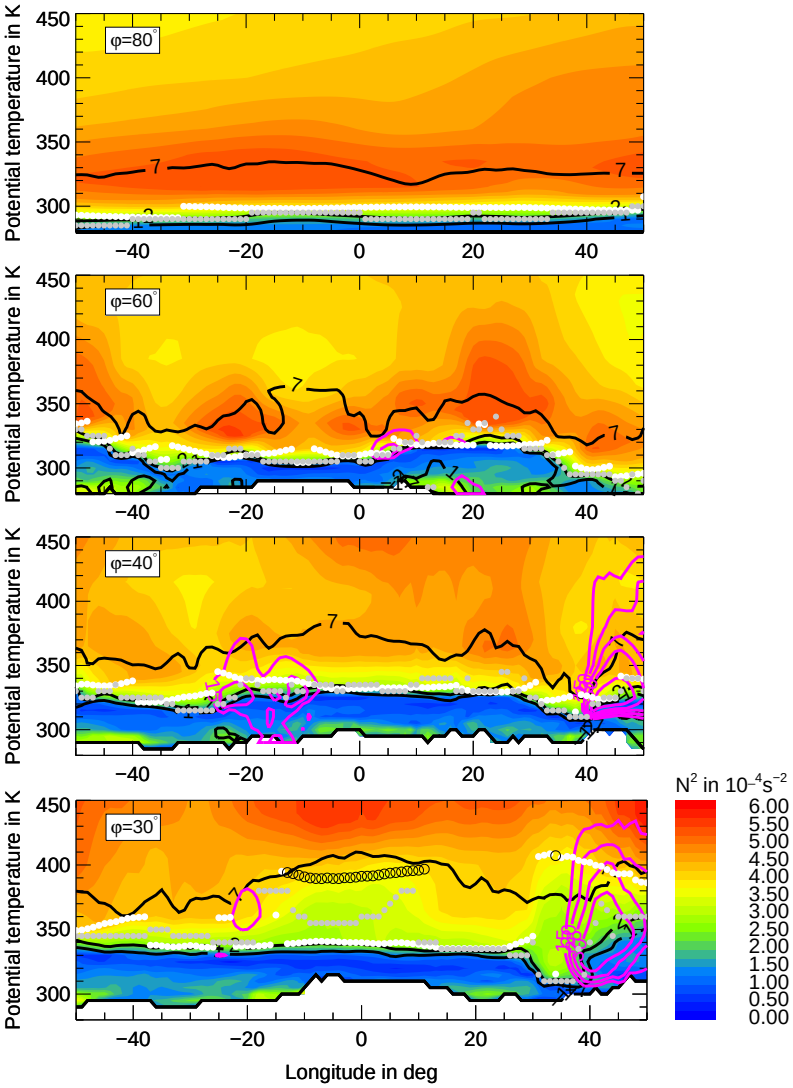

Figure 5.7: Static stability in $10^{-4}\,\mathrm{s}^{-2}$ on different latitudes between 30° N and 80° N on 27 April 2003. The $\mathrm{TP_{th}}$ (white dots), the $\mathrm{TP_{gradPV}}$ (gray dots), the 1 PVU, 2 PVU and 7 PVU isolines (solid black lines) and the meridional wind velocity (solid pink lines) are shown. Double tropopauses are indicated by open black circles.

tropopauses (gray crosses, middle panel) the difference is very large. In the polar regions both tropopauses coincide very well, and the difference increases toward the equator. Here the tropopauses diverge especially in regions of troposphere to stratosphere exchange in the vicinity of jet streams or tropopause folds. This behavior is similar to the dynamical

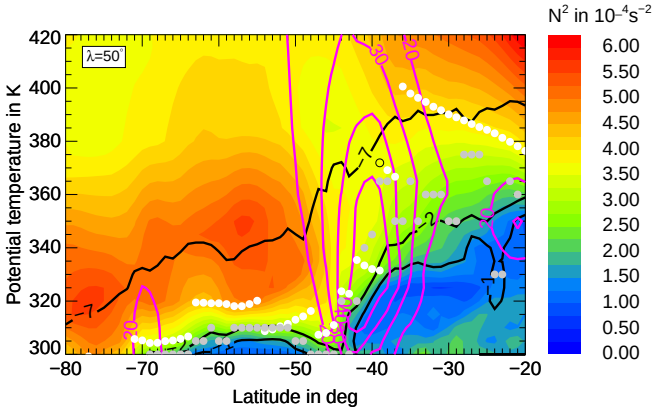

Figure 5.8: Static stability in $10^{-4}\,\mathrm{s}^{-2}$ at the longitude $\lambda = 50°$ W on 27 April 2003. The $\mathrm{TP_{th}}$ (white dots), the $\mathrm{TP_{gradPV}}$ (gray dots), the PV isolines (1 PVU, 2 PVU and 7 PVU as solid black lines) and the zonal wind velocity (solid pink lines) are shown.

tropopause $\mathrm{TP_{dyn}}$, which frequently deviates from the thermal tropopause in many cases of troposphere and stratosphere exchange processes.

The dependence of the PV gradient tropopause $\mathrm{TP_{gradPV}}$ on different latitudes in the northern hemisphere is shown in Figure 5.7. This figure shows the static stability on 27 April 2003 (colored contours) together with $\mathrm{TP_{th}}$ (white dots), $\mathrm{TP_{gradPV}}$ (gray dots) and $\mathrm{TP_{dyn}}$ as black solid PV=2 PVU isoline. At 80° N a good agreement between the three tropopauses $\mathrm{TP_{gradPV}}$, $\mathrm{TP_{th}}$ and $\mathrm{TP_{dyn}}$ is evident. The tropopause region seems very stable, which is also evident from the stable tropopause inversion layer (TIL) above the thermal tropopause. The height of the TIL increases together with the height of the tropopauses toward lower latitudes, e.g., 30° N (bottom panel). At the same time, the difference between $\mathrm{TP_{gradPV}}$ and $\mathrm{TP_{th}}$ increases in regions with double tropopauses (open black circles) or near the subtropical jet stream (pink contours) at 30° N or 40° N (bottom panels). Overall, there is a good agreement between the 2 PVU isoline, which is frequently used as the dynamical tropopause, and the PV gradient tropopause $\mathrm{TP_{gradPV}}$. However, this is not generally valid in the vicinity of the jet streams. Figure 5.8 shows a similar representation of the static stability together with the three tropopauses at a longitude of $\lambda = 50°$ W. The jet stream (pink contours) is characterized by a break in the thermal tropopause (white dots) and the PV gradient tropopause (gray dots) is different from the thermal tropopause. In the vicinity of the jet stream the height of $\mathrm{TP_{gradPV}}$ is sometimes identical to the height of the 2 PVU isoline, but sometimes the height of $\mathrm{TP_{gradPV}}$ follows different PV isolines.

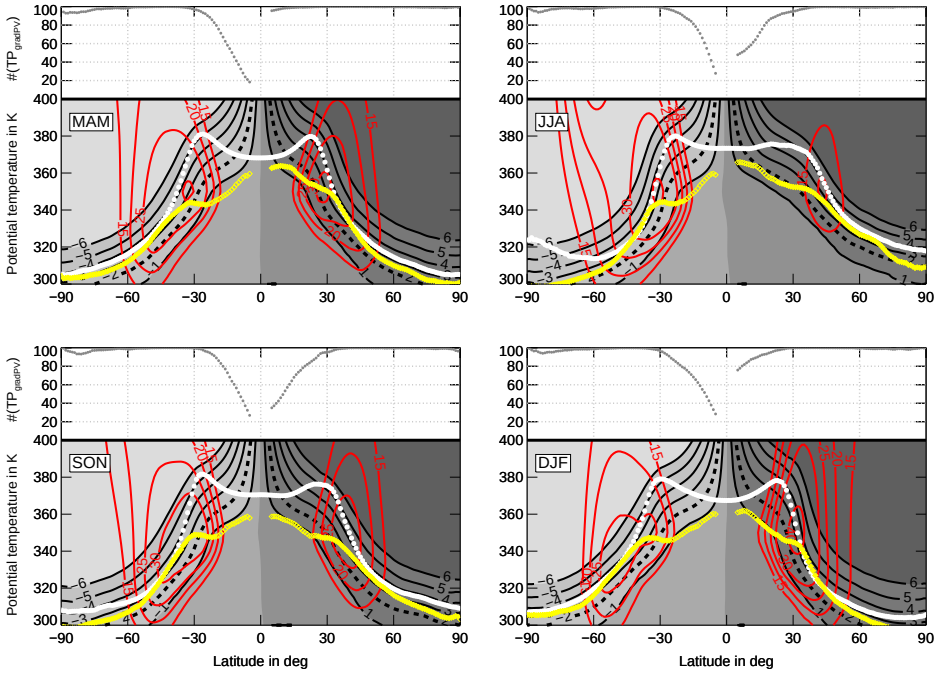

Figure 5.9: Zonal and time mean potential temperature height of the PV gradient tropopause $\mathrm{TP_{gradPV}}$ (yellow dots) and of the thermal tropopause $\mathrm{TP_{th}}$ (white dots) for different northern hemisphere seasons: spring (MAM) and summer (JJA) 2002 (top panels), autumn (SON) and winter (DJF) 2002 (bottom panels). The potential vorticity is gray shaded (-30,-6,-1,1,6 and 30 PVU contours) and the PV isolines between $|1|$ and $|6|$ PVU are additionally highlighted by black lines. The 2 PVU isoline is a black dashed line. The zonal wind is shown in red. The percentage of valid $\mathrm{TP_{gradPV}}$ values per latitude bin is shown in the top panels, respectively. The zonal and time mean height of $\mathrm{TP_{gradPV}}$ is marked by open yellow diamonds for bins near the equator including less than 90% valid $\mathrm{TP_{gradPV}}$ values per latitude bin.

5.1.3 Climatology of PV at the PV gradient tropopause

The PV gradient tropopause $\mathrm{TP_{gradPV}}$ is proposed here as an alternative to the dynamical tropopause $\mathrm{TP_{dyn}}$, a surface which is based on a fixed value of the PV for the entire hemisphere. $\mathrm{TP_{gradPV}}$ is based on dynamical quantities and contains a dependence on the geographical location. This implies a variable PV value at the height of the PV gradient tropopause. Thus, the PV distribution at the level of the PV gradient tropopause is of interest and is analyzed in the following.

Figure 5.9 shows the zonal and time mean of the PV for the different northern hemisphere seasons of spring and summer (top panels) or autumn and winter (bottom panels) in 2002 as a function of the potential temperature. In all seasons the PV gradient tropopause $\mathrm{TP_{gradPV}}$

(yellow diamonds) deviates from the dynamical tropopause $\mathrm{TP_{dyn}} = \pm 2\,\mathrm{PVU}$ (dashed black lines) for most latitudes. Near the subtropical jet streams, both tropopauses are very close to each other. Toward the poles $\mathrm{TP_{th}}$ lies below $\mathrm{TP_{gradPV}}$ (white dots), but for most of the time it is above $\mathrm{TP_{dyn}} = \pm 2\,\mathrm{PVU}$ (dashed black line). For seasons DJF and MAM, the height of $\mathrm{TP_{gradPV}}$ (yellow diamonds) corresponds rather well the height of the thermal tropopause $\mathrm{TP_{th}}$ in the extratropics in both hemispheres between the jet cores and the poles. During seasons JJA and SON, both tropopauses $\mathrm{TP_{gradPV}}$ and $\mathrm{TP_{th}}$ deviate near the poles, especially at the south pole during the southern hemisphere winter (JJA). The height of the $\mathrm{TP_{th}}$ increases toward the south pole, which may well be due to the onset and build up of the polar vortex. At that time, the south pole region cools and the isentropes ascend toward the pole relative to the pressure levels. Ascending isentropes near the south pole during southern hemisphere winter can also be seen in Figure 4.1 (left–hand panel) or in Figure 2 of Birner et al. (2006). In all seasons, the heights of $\mathrm{TP_{gradPV}}$ and $\mathrm{TP_{th}}$ deviate especially in the tropics equatorward of the subtropical jet streams (red contours). The latitude and the longitude position of the PV gradient tropopause $\mathrm{TP_{gradPV}}$ is determined from the equivalent latitude position of the jet core $J_c(\theta)$ within the equivalent latitude range between the two jet boundaries $J_b(\theta)$ on the different isentropes. Hence, there are also some $\mathrm{TP_{gradPV}}$ determined equatorward of the subtropical jet streams, which result from the equivalent latitude isolines, especially those of the jet boundaries $J_b(\theta)$, moving equatorward in specific regions. Figure 5.4 (right–hand bottom panel) shows an example of the jet core and its jet boundaries on the 340 K isentrope. Above Western Africa the valid range for $\mathrm{TP_{gradPV}}$ is confined to the $\varphi_e = 22.5^\circ$ isoline, which is partly located equatorward of the latitude $\varphi = 20^\circ$. These equatorward deformations of the jet boundaries have an influence on the determination of $\mathrm{TP_{gradPV}}$ equatorward of the jet cores. However, the frequency of determining the PV gradient tropopause $\mathrm{TP_{gradPV}}$ per 1° latitude bin decreases rapidly from around 100% at the cores of the subtropical jet streams toward the equator (see Figure 5.9, dotted gray line in the top panels, respectively). The zonal and time mean height of $\mathrm{TP_{gradPV}}$ at latitudes with a frequency of less than 90% of an occurrence of $\mathrm{TP_{gradPV}}$ is marked by the open yellow diamonds. The frequency of finding $\mathrm{TP_{gradPV}}$ per latitude bin decreases roughly from the geographical location of the subtropical jet streams (red contours) toward the equator. For that reason, in the following the exact value of the PV at $\mathrm{TP_{gradPV}}$ is analyzed poleward of $\phi = \pm 20^\circ$, where the frequency of finding $\mathrm{TP_{gradPV}}$ per latitude bin is greater than 90%.

Figure 5.10 shows the seasonal probability distribution functions of the PV at $\mathrm{TP_{gradPV}}$ (gray shaded) both for the southern hemisphere (left–hand panels) and the northern hemisphere (middle panels), respectively. Here, the daily ECMWF data for 2002 within the different seasons are used to calculate the time mean of the PV at $\mathrm{TP_{gradPV}}$ in meridional 5° latitude

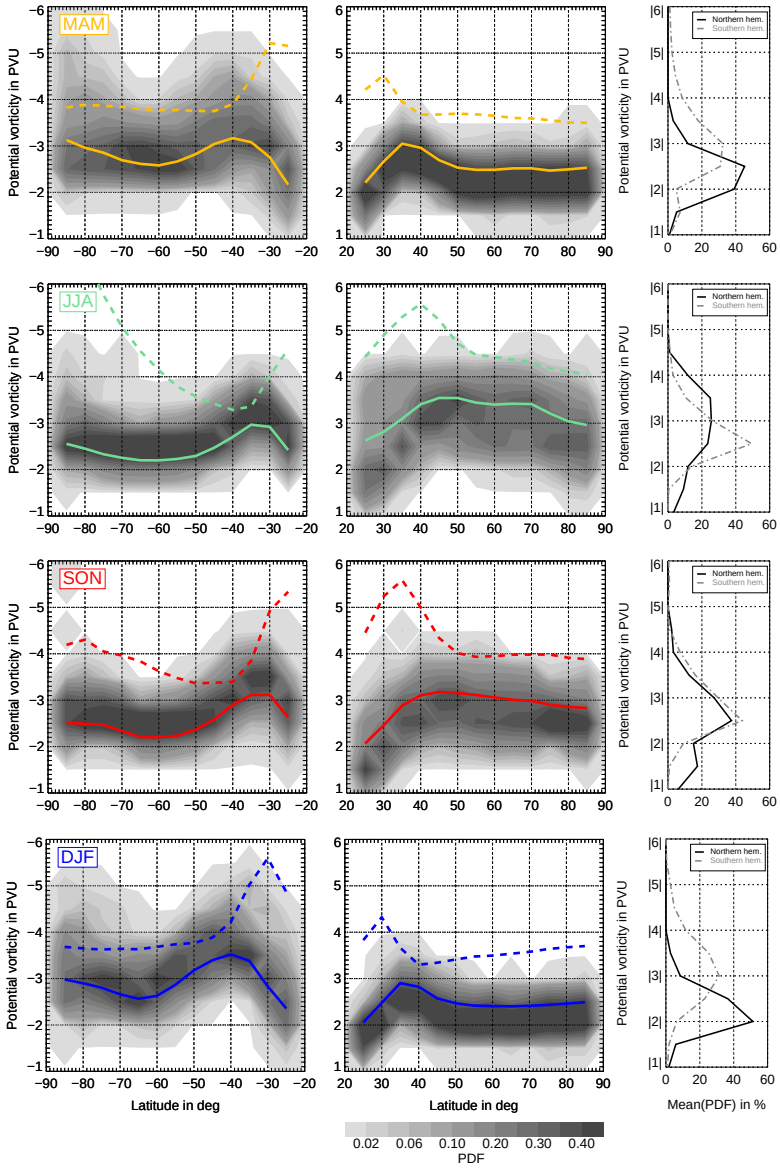

Figure 5.10: Probability distribution functions of PV in PVU at $\mathrm{TP}_{\mathrm{gradPV}}$ (gray shaded) for northern hemisphere spring (MAM), summer (JJA), autumn (SON) and winter (DJF) 2002 (from top to bottom) in the southern hemisphere (left–hand panels) and in the northern hemisphere (middle panels). The mean PV at $\mathrm{TP}_{\mathrm{gradPV}}$ (solid lines) together with the mean PV at $\mathrm{TP}_{\mathrm{th}}$ (dashed lines) per 5° latitude bins are shown. The right–hand panels show the mean PDF of PV at $\mathrm{TP}_{\mathrm{gradPV}}$ both for the southern hemisphere (dashed grey line) and for the northern hemisphere (solid black line). The respective PV bins are given in absolute values.

bins. There is a decrease of the mean PV at $\mathrm{TP}_{\mathrm{gradPV}}$ from the subtropics to the midlatitudes (solid lines). This decrease is more pronounced in the southern hemisphere than in the northern hemisphere in all seasons. The seasonal cycle in the height of the tropopause is apparent with a higher tropopause in summer (JJA for northern hemisphere, DJF for southern hemisphere) associated with a higher mean PV at $\mathrm{TP}_{\mathrm{gradPV}}$ than in winter (DJF for northern hemisphere, JJA for southern hemisphere). During northern hemisphere summer the mean PV at $\mathrm{TP}_{\mathrm{gradPV}}$ in the extratropics is between 3.0 and $3.5\,\mathrm{PVU}$ and during northern hemisphere winter it is between 2.5 and $3\,\mathrm{PVU}$. The mean PV at the thermal tropopause $\mathrm{TP}_{\mathrm{th}}$ (dashed lines) also decreases toward the midlatitudes in both hemispheres, but for each latitude bin it is higher than the PV at the $\mathrm{TP}_{\mathrm{gradPV}}$. Here, the discrepancy between the two tropopauses is largest on the anticyclonic side of the subtropical jet stream core, a dynamically active region with a troposphere to stratosphere exchange of air masses (Pan et al., 2009b). This discrepancy is also apparent in the respective panels of Figure 5.9. The distance between $\mathrm{TP}_{\mathrm{th}}$ and $\mathrm{TP}_{\mathrm{gradPV}}$ is closest on the cyclonic side of the jet core on lower isentropic surfaces than on the anticyclonic side of the jet core.

In both hemispheres, the PV increases for $\mathrm{TP}_{\mathrm{th}}$ and $\mathrm{TP}_{\mathrm{gradPV}}$ at higher latitudes toward the poles except for the northern hemisphere summer (JJA) and autumn (SON). This increase is again sharper in the southern hemisphere compared to the northern hemisphere and at the same time extends farther equatorward. During winter (DJF for northern hemisphere, JJA for southern hemisphere) this increase in PV is sharpest at both tropopauses toward the poles, especially the increase of the PV at $\mathrm{TP}_{\mathrm{th}}$. The difference between the PV at both tropopauses near the poles is also largest during winter in the respective hemisphere, albeit more pronounced in the southern hemisphere. This may be due to the occurrence of the polar vortex during winter, which is substantially stronger in the southern hemisphere than in the northern hemisphere. Radiative cooling and the decrease of the temperature during polar night in the southern hemisphere leads to the formation of the polar vortex. A typical vortex is marked by strong circumpolar winds and cold temperatures in the interior. As these circumpolar winds begin to increase in autumn (MAM for southern hemisphere, SON for northern hemisphere), the polar vortex consequently spins up, the isentropes rise and the values of the PV rise at the pole (e.g. Nash et al., 1996). Thus there is a sharp increase of PV at $\mathrm{TP}_{\mathrm{gradPV}}$ toward the pole in autumn. The increase of the PV can be explained by the subsequent downward transport of air masses within the polar vortex (Schoeberl et al., 1992), which may also affect the distribution of the PV at $\mathrm{TP}_{\mathrm{gradPV}}$ and $\mathrm{TP}_{\mathrm{th}}$ in spring (SON for southern hemisphere, MAM for northern hemisphere). In the northern hemisphere the descent of air masses within the polar vortex during winter (DJF) is different compared to the descent within the polar vortex in the southern hemisphere during winter (JJA). This may

be the reason for the less sharp increase in PV at $\mathrm{TP}_{\mathrm{gradPV}}$ and $\mathrm{TP}_{\mathrm{th}}$ toward the pole in the northern hemisphere. Haynes and Shuckburgh (2000a) characterized the transport structure of the polar vortex with the help of the isentropic eddy diffusivity field k_{eff}. They observed stronger polar vortex barriers associated with a minimum k_{eff} in the southern hemisphere compared to the northern hemisphere pole, which is consistent with the different distribution of the PV at $\mathrm{TP}_{\mathrm{gradPV}}$ toward the poles in the two hemispheres.

The difference in the location of the subtropical maximum PV at $\mathrm{TP}_{\mathrm{gradPV}}$ between the two hemispheres in all seasons can be explained by the mean location of the subtropical jet stream. This location is slightly different in both hemispheres following the sun as it moves northward during the warm seasons (spring and summer) and southward during the cold seasons (autumn and winter). The subtropical jet stream, which also separates the troposphere from the stratosphere on an isentropic surface, has a stronger meandering shape in the northern hemisphere and spans a larger meridional range. In the southern hemisphere, the subtropical jet stream has a more stable and continuous position, which is also due to the lack of land masses in this hemisphere. This may also be the reason for the larger gradient of PV at $\mathrm{TP}_{\mathrm{gradPV}}$ between the subtropics and the polar regions in the southern hemisphere.

The gradient of PV at $\mathrm{TP}_{\mathrm{gradPV}}$ between the subtropics and the polar regions is highest during winter in the respective hemisphere. The maximum PV at $\mathrm{TP}_{\mathrm{gradPV}}$ in the northern hemisphere summer is smoother compared to the southern hemisphere summer possibly due to the meandering shape, the weaker wind velocity and larger horizontal extension due to the meandering shape of the northern hemisphere subtropical jet stream. In the southern hemisphere, the maximum PV at $\mathrm{TP}_{\mathrm{gradPV}}$ close to the subtropical jet core is very persistent throughout the year, while in the northern hemisphere this maximum is shifted poleward depending on season and is weaker in summer. Haynes and Shuckburgh (2000a) also characterized the tropopause barrier close to the jet streams with the help of the effective diffusivity on isentropes. They observed a generally stronger barrier in the southern hemisphere than in the northern hemisphere during the same season. This finding is consistent with the maximum PV at $\mathrm{TP}_{\mathrm{gradPV}}$ in the vicinity of the subtropical jet streams, which is sharper in the southern hemisphere compared to the northern hemisphere for the same season.

Figure 5.10 may be considered as a climatology of the PV at the PV gradient tropopause $\mathrm{TP}_{\mathrm{gradPV}}$. It can be used to decide which PV value should be taken as the dynamical tropopause depending on the meridional geographical region. The zonal and time mean meridional PV distribution at $\mathrm{TP}_{\mathrm{gradPV}}$ (solid colored lines) is larger in both hemispheres than the commonly used PV=2 PVU. There may rather sporadically be a dynamical tropopause associated with PV=2 PVU. Table 5.1 contains the mean PDF of the PV at $\mathrm{TP}_{\mathrm{gradPV}}$ taken from Figure 5.10 (right–hand panels) for different seasons in the northern

Table 5.1: Mean percentage of PV between 2 PVU and 4 PVU at the PV gradient tropopause $\mathrm{TP}_{\mathrm{gradPV}}$ for different seasons in the northern hemisphere in 2002. These values are taken from Figure 5.10 (right–hand panels) and represent the mean probability distribution (PDF) per PV bin. Bold red values denote the highest percentage of PV at $\mathrm{TP}_{\mathrm{gradPV}}$ within the respective seasons.

PV at $\mathrm{TP}_{\mathrm{gradPV}}$	spring (MAM)	summer (JJA)	autumn (SON)	winter (DJF)
2.0 PVU	38%	11%	15%	**51%**
2.5 PVU	**45%**	23%	**37%**	36%
3.0 PVU	11%	**25%**	27%	8%
3.5 PVU	3%	**25%**	12%	27%
4.0 PVU	0%	12%	32%	0%

hemisphere. The table thus reflects the frequency and percentage of different PV values at $\mathrm{TP}_{\mathrm{gradPV}}$ between 2 PVU to 4 PVU in the northern hemisphere. In the northern hemisphere midlatitudes and polar region, the PV gradient tropopause $\mathrm{TP}_{\mathrm{gradPV}}$ is related to the 2 PVU isoline during spring (MAM) and winter (DJF) with a probability of around 38% and 51%, respectively (see Figure 5.10, top and bottom right–hand panels). During summer (JJA) and autumn (SON), when the tropopause is higher compared to the other seasons, the probability of a $\mathrm{TP}_{\mathrm{gradPV}}$ at the 2 PVU isoline decreases to 11% and 15%, respectively. $\mathrm{TP}_{\mathrm{gradPV}}$ is most probably related to a PV=2.5 PVU isoline during spring and autumn. In winter, the mean percentage is highest for PV=2.0 PVU. In summer, the most probable PV values at $\mathrm{TP}_{\mathrm{gradPV}}$ are between PV=3.0−3.5 PVU, although the mean percentage is comparatively high for the entire PV range between PV=2.0−4.0 PVU.

5.2 Static stability relative to the jet streams

Figure 5.4 (middle panels) shows the distribution of the static stability on isentropes together with the variation of the jet streams (defined by its jet core $J_c(\theta)$ and jet boundaries $J_b(\theta)$). The static stability increases on isentropes from the equator toward the pole. At higher latitudes the static stability is lowest on the 300 K isentrope compared to the isentropes above for the case of 27 April 2003.

In addition to the proposed link between the static stability and mixing in the extratropics in Chapter 4 the mixing on isentropic surfaces across the jet streams will be analyzed. Relative to the jet cores $J_c(\theta)$ and the jet boundaries $J_b(\theta)$, as determined in section 5.1.2, the permeability of the jet streams on different isentropes is analyzed below.

5.2.1 Seasonal permeability of the jet streams

The seasonal dependence of the jet streams concerning their behavior as so–called transport barriers in the winter months compared to the summer months on three typical isentropes crossing the jet cores, e.g., 320 K, 340 K and 360 K isentropes, is analyzed. The northern hemisphere air masses on these isentropes are divided into three different regions:

- Region I = Troposphere, between the equatorward jet boundary and the equator
- Region II = Between the equatorward and poleward jet boundary
- Region III = Stratosphere, between the poleward jet boundary and the North pole

Using tracer correlations the seasonal permeability of the jet stream is shown on the three different isentropes within the three different regions. For that reason the ozone and water vapor data from the ECMWF operational analysis on the 18 different SPURT flight days between 2001 and 2003 are selected. The focus is on the European region between 50° W and 50° E. The data are binned according to the different seasons (2 flight days for summer, 5 flight days for winter). Further the static stability N^2 is calculated for each data point in the tracer correlation.

Figure 5.11 shows the ECMWF ozone and water vapor tracer correlation during summer colored with the static stability for the three regions. Within Region I, the tropospheric part of the isentropes (left–hand panels), a relative low ozone concentration up to 200 ppbv is related to a high water vapor concentration. The water vapor concentration decreases with height. While on the 320 K and 340 K isentropes a well pronounced lower part of the 'L–shaped' correlation is observed, the 360 K isentrope is related to low ozone and to low water vapor concentrations. The static stability related to this tropospheric part of the isentropes in Region I is very low for each of the three isentropes.

The stratospheric part in the extratropics during summer, i.e., Region III (Figure 5.11, right–hand panels), shows a large mixed region on the 340 K isentrope, which is related to a very high static stability. The high static stability within Region III on each isentrope belongs to the tropopause inversion layer (TIL), which is discussed in Chapter 4 as a part of the mixing layer. Dethof et al. (2000) analyzed the isentropic surfaces from 330 K to 360 K between the troposphere and the stratosphere and found these isentropic fluxes to be strongest on the 330 K isentrope throughout the year and decreases in magnitude with height. Consistent with the study of Dethof et al. (2000) the tracer correlation in Region III is constrained increasingly to the upper branch of a nearly 'L–shaped' tracer correlation from the 320 K isentrope toward the 360 K isentrope. The mixing region is close to the stratospheric reservoir and the corresponding mixing degree f_{mix} is very low. At the same time, the static stability on the 340 K

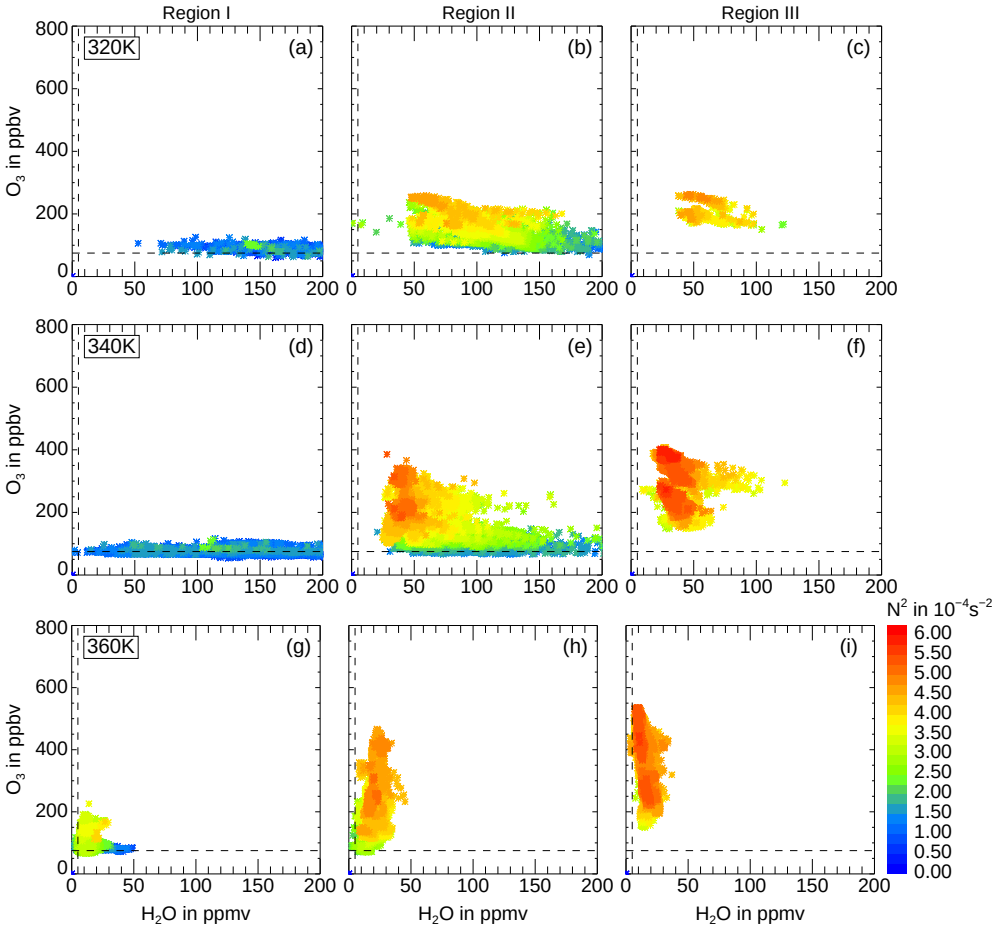

Figure 5.11: Summer ECMWF water vapor and ozone tracer correlation on different isentropes 320 K (top), 340 K (middle) and 360 K (bottom) based on all SPURT flight days between 2001 and 2003. Data are selected for each isentrope in the troposphere (Region I, left–hand column), between the jet boundaries (Region II, middle column) and the stratosphere (Region III, right–hand column). The color code reflects the static stability N^2 in $10^{-4}\,\mathrm{s}^{-2}$.

and 360 K isentropes is higher than on the lower 320 K isentrope.

Air masses between the jet boundaries in Region II (Figure 5.11, middle panels) can be characterized by a large mixing degree and a large extent of the mixing layer on the 340 K isentrope during summer, i.e., the air masses are farthest away from the two original tropospheric and stratospheric reservoirs. The lower 320 K isentrope is dominated by a mixing region near the tropospheric reservoir, the upper 360 K isentrope by a mixing region near

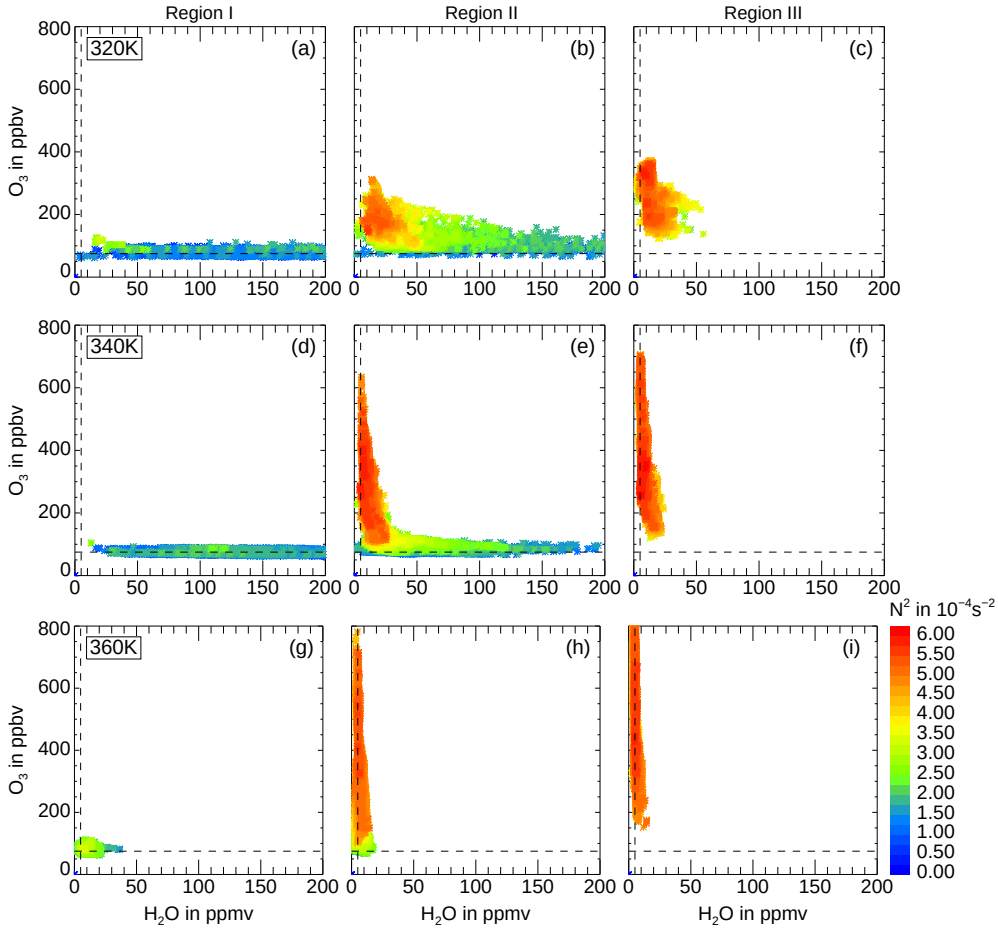

Figure 5.12: Winter ECMWF water vapor and ozone tracer correlation on different isentropes 320 K (top), 340 K (middle) and 360 K (bottom) based on all SPURT flight days between 2001 and 2003. Data are selected within Region I (left–hand column), Region II (middle column) and Region III (right–hand column). The color code reflects the static stability N^2 in $10^{-4}\,\mathrm{s}^{-2}$.

the stratospheric reservoir. Air masses within Region II are largely related to an intermediate static stability typical for the fresh mixing events in the vicinity of the jet streams already discussed as TFM branch in Chapter 4.

The permeability of the jet stream during summer is most clearly seen on the 340 K isentrope (middle panels). Region I shows the lower branch of the 'L–shape' related to low static stability typical for the troposphere. Region II, which is constrained to the jet streams, is related to a well pronounced mixing layer with intermediate static stability values. Region III in the

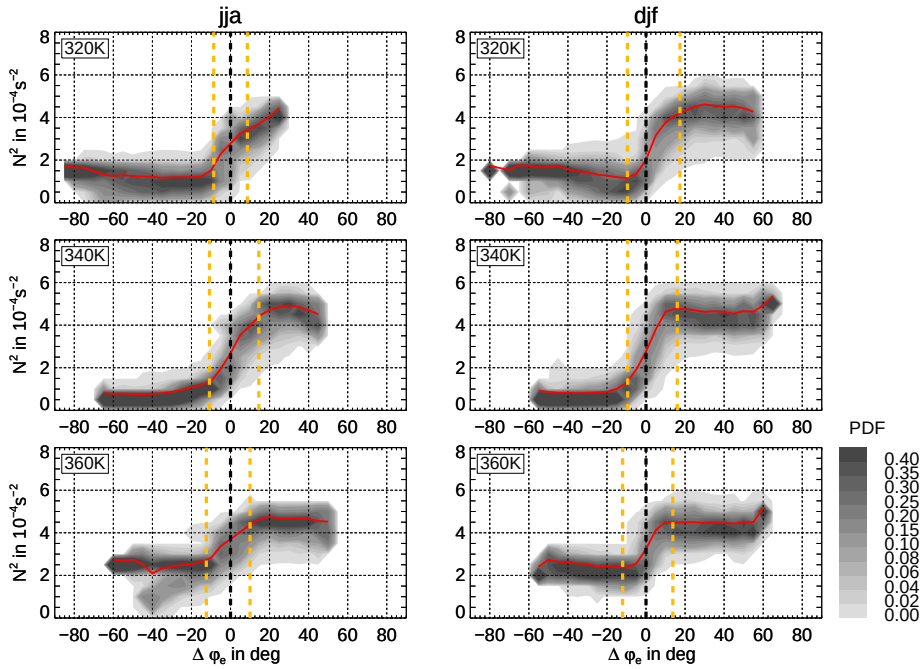

Figure 5.13: Probability distribution functions of static stability N^2 in $10^{-4}\,\mathrm{s}^{-2}$ relative to the jet core ($\Delta\varphi_e$=0, dashed black line) in equivalent latitude differences $\Delta\varphi_e$ for summer (left–hand panels) and winter (right–hand panels) on three different isentropes. The mean jet boundaries for the different seasons are shown by the dashed yellow lines and the mean of the N^2 probability distribution per $\Delta\varphi_e$ bin is given by the solid red line. The bin size for N^2 is $0.5 \cdot 10^{-4}\,\mathrm{s}^{-2}$ and for $\Delta\varphi_e$ it is $5°$.

stratosphere shows an even higher mixing degree related to a high stability in the TIL. This shows, that the jet streams are very permeable for an isentropic transport of air masses from the troposphere to the stratosphere during summer. The summer 360 K isentrope does not show a well defined mixing layer, indicated by the upper part of the 'L–shape'. The mixing layer is thus very close to the stratospheric reservoir within each region (Region I–Region III). The mixing of air between the troposphere and the stratosphere is strongest on lower isentropic surfaces. The lowermost stratosphere becomes more isolated concerning a mixing of tropospheric air masses across the tropopause with increasing altitude.

The isentropic transport across the tropopause and the jet core has a pronounced seasonal cycle. Therefore, the winter isentropes (Figure 5.12) show a different behavior regarding the tracer correlation between ECMWF ozone and water vapor than the summer isentropes. The jet streams act as a transport barrier during the winter months. The 340 K isentrope is related to a typical 'L–shaped' tracer correlation in the vicinity of the jet stream within Region II (Figure 5.12, lower middle panel). Thus, the nearly perfect 'L–shaped' tracer correlation in

the vicinity of the jet core between the jet boundaries demonstrates the tropopause barrier in the vicinity of the jet streams during winter. Further, the tropospheric part in Region I is related to the lower branch and the stratospheric branch in Region III to the upper part of a 'L–shaped' tracer correlation. Tropospheric air masses at lower latitudes are separated from stratospheric air masses at higher latitudes on isentropes and there is a sharp transition of the static stability across the jet streams demonstrating the sharpness of the tropopause.

The mixing degree is very low on the 340 K and 360 K isentrope during winter, the mixed branch is very close to the original reservoirs. However, at the 320 K isentrope during winter a certain mixing degree across the jet stream is also observed. For isentropes crossing the lower parts of the jet streams the isentropic transport may also play a large role during winter. This is indicated by the mixing layer on the 320 K isentrope within Region II (middle panel) which is very similar to that during the summer. The transport across the jet core on the 340 K and 360 K isentropes has a stronger seasonality. Largest values of mixing degree occur during summer, whereas during winter they are lower due to the reduced mixing across the jet stream.

In order to investigate the dependence of the static stability relative to the jet cores on the isentropes the data from Figures 5.11 and 5.12 are transformed on a new coordinate system relative to the jet cores. For each data point the distance relative to the jet core $\Delta\varphi_e$ in equivalent latitudes is calculated. The position of the jet core dependent in space and time is used as point of origin and is set to zero. Poleward values are related to positive values of equivalent latitude $\Delta\varphi_e$ relative to the jet core, values toward the equator to a negative $\Delta\varphi_e$. Figure 5.13 shows the probability distribution function of static stability N^2 from the three different isentropic areas (Region I–III) in Figures 5.11 and 5.12 relative to the jet core. Here, the data are binned in equivalent latitude space and the mean static stability (solid red lines) is calculated per bin. For each selected isentropic surface (320 K, 340 K and 360 K) a continuous increase of N^2 across the jet streams (Region II) from lower latitudes on the equatorward side of the jet stream (Region I) to higher latitudes on the poleward side of the jet stream (Region III) is observed both for summer (left–hand panels) and for winter (right–hand panels). Within the troposphere equatorward of the lower jet boundary (left–hand dashed yellow line) in Region I the mean N^2 distribution per $\Delta\varphi_e$ bin (red line) is very homogeneous and lowest on the 340 K isentrope. Poleward of the upper jet boundary (right–hand dashed yellow line) in Region III, N^2 is also very homogeneous with distance from the jet core and the mean N^2 is now highest on the 340 K isentrope. The gradient of N^2 between the tropospheric part on lower latitudes toward the stratospheric part at higher latitudes is highest through the jet core on the 340 K isentrope. Both for summer and winter the increase of N^2 between the jet boundaries is largest on the 340 K isentrope, but during winter this

increase is sharper and happens at a closer distance from the jet core compared to summer. This again shows the jet stream as a strong barrier to quasi–isentropic transport during the winter months. Consistent with the 'L–shaped' tracer correlation during winter on the 340 K isentrope between the jet boundaries in Region II (Figure 5.12, panel (e)) the stratospheric branch is clearly separated from the tropospheric branch. Similar to the characteristics in the gradient of chemical trace gas concentrations a very low N^2 concentration within the troposphere is clearly separated from a very high concentration in the stratosphere, especially on the 340 K isentrope (Figure 5.13, middle right–hand panel).

5.3 Results of this chapter

This chapter presents a method to determine the location of the jet cores $J_c(\theta)$ and the jet boundaries $J_b(\theta)$ including the meandering shape of the jet streams. This method is based on the isentropic gradient of PV with equivalent latitude. On the one hand this facilitates an analysis of transport between the troposphere and the stratosphere across the jet streams. On the other hand the jet cores allow a definition of a new dynamical tropopause, the PV gradient tropopause $\mathrm{TP}_{\mathrm{gradPV}}$, which depends on the isentropic gradient of PV. This tropopause serves as an alternative of the dynamical tropopause $\mathrm{TP}_{\mathrm{dyn}}$, which is based on a particular value of the PV.

A zonal and time mean analysis of the PV distribution at $\mathrm{TP}_{\mathrm{gradPV}}$ suggests roughly the $2.5\,\mathrm{PVU} - 3.5\,\mathrm{PVU}$ isolines as dynamical tropopause in the northern hemisphere extratropics depending on season. In contrast, in the southern hemisphere, where a greater gradient between the zonal and time mean PV at $\mathrm{TP}_{\mathrm{gradPV}}$ appears from the midlatitudes to the pole than in the northern hemisphere, the zonal and time mean PV at $\mathrm{TP}_{\mathrm{gradPV}}$ ranges between 2 PVU and 3.5 PVU. The commonly used 2 PVU isoline as dynamical tropopause is with a probability of around 51% (11%) representative for the $\mathrm{TP}_{\mathrm{gradPV}}$ during winter (DJF) (summer (JJA)) in the northern hemisphere. In winter (DJF) in the northern hemisphere the mean percentage of PV at $\mathrm{TP}_{\mathrm{gradPV}}$ is highest for PV=2.0 PVU. In summer the most probable PV values at $\mathrm{TP}_{\mathrm{gradPV}}$ are between PV=3.0−3.5 PVU. Based on the isentropic gradient of PV with equivalent latitude the analysis suggests that a particular PV value is not appropriate for the tropopause in the entire extratropics.

The seasonality of isentropic mixing across the jet stream is studied within three isentropic regions: between the jet boundaries (Region II), outside the jet boundaries toward the pole (Region III) and outside toward the equator (Region I). Water vapor and ozone tracer correlations in connection to the static stability N^2 are a valuable tool to study the dependence dependence of mixing across the jet stream on the height of the isentropic surface. The cross–

tropopause transition from the troposphere to the stratosphere is sharpest during winter on the 340 K. On the one hand this is shown by the 'L–shaped' tracer correlation in the vicinity of the jet stream separating low stability air masses on the equatorward side of the jet streams from high stability air masses on their poleward side. On the other side the transition of N^2 across the jet streams relative to the jet cores in equivalent latitude differences from Region I to Region III is sharper during winter than during summer. These analyses demonstrate the isentropic transport barrier function of the jet streams during winter and their permeability during summer.

Chapter 6

Summary and outlook

In this thesis, the extratropical upper troposphere and lower stratosphere (UT/LS) is investigated with the help of in–situ measurements of O_3, H_2O and CO from the SPURT and POLARCAT–GRACE campaigns as well as from the MOZAIC long–term observations. Furthermore, model calculations are performed using CLaMS and the Reading radiative transfer model.

In the first part of the thesis, the measurements performed during the sparse SPURT flights and the frequent MOZAIC flights between November 2001 and July 2003 over the European region are statistically analyzed. For this purpose, a suitable statistical procedure is developed for comparing trace gas data sets from different instruments with different sampling characteristics, which do not coincide in space and time. With the help of the statistical tests the following questions concerning the UT/LS can be answered:

1. *Do the H_2O and O_3 data sets of MOZAIC and SPURT with different spatial and temporal coverage in the UT/LS and with different instrument characteristics represent the same population in the atmospheric system?*

   The H_2O and the O_3 data sets of MOZAIC and SPURT differ from each other and do not belong to the same population. The Kolmogoroff–Smirnoff test reveals that the distribution functions from SPURT and MOZAIC trace gases differ from each other with a confidence of 95 %. A sampling and a modification of the H_2O data sets is necessary before the performance of the statistical analysis due to the different measurement techniques in SPURT (Fast In–situ Stratospheric Hygrometer, FISH) and in MOZAIC (MOZAIC Humicap sensor). In contrast, a modification of the O_3 data is not necessary because of the same measurement techniques. Nevertheless, the sample means are still different with a higher mean H_2O (lower O_3) for SPURT than for MOZAIC due to different flight patterns.

2. *Are the SPURT campaigns, with around eight flight missions in each season, as representative as the daily MOZAIC flights above Europe? Are the SPURT measurements suited for a climatological investigation on a seasonal and annual time scale and do they represent the full atmospheric variability of trace gases in the UT/LS?*
   A variance analysis shows a different character of variability for the two trace gas data sets. While the SPURT H_2O data only contain atmospheric processes variable on a diurnal or synoptic time scale, MOZAIC H_2O data also reveal processes which vary on inter–seasonal and seasonal time scales. The SPURT H_2O data set does not represent the full MOZAIC H_2O variance in the UT/LS for climatological investigations, whereas the variance of SPURT O_3 is represented much better. This means that the SPURT data set with around eight flights per season is sufficient to represent the O_3 variability in the UT/LS as described by the frequent, almost daily, MOZAIC flights. SPURT H_2O data are better suited for the stratosphere than MOZAIC H_2O data, since the MOZAIC RH sensor loses its sensitivity in the stratosphere.

3. *How many flights are necessary to capture the full H_2O variability in the UT/LS?*
   A variance analysis of subsamples of MOZAIC data between November 2001 and July 2003 shows that the full H_2O variability revealed by the MOZAIC data set would be captured if there were measurement flights every fourth day in the upper troposphere (UT) and every sixth day in the lower stratosphere (LS). That means flights would have to be performed on around eight days per month in the troposphere and on around four days per month in the stratosphere. These flights have to be equally distributed over time, i.e., they cannot be performed on four consecutive days

In the second part of the thesis, the relationship between the static stability N^2 and the mixing of trace gases in the tropopause inversion layer (TIL) is investigated using in–situ aircraft observations obtained during SPURT. A new simple measure of the mixing degree of a particular air mass based on O_3–CO tracer correlations is developed. Two different branches, the TFM branch and the TIL branch, were identified in the extratropical mixing layer, with different characteristics in thermal stratification, i.e., static stability N^2. The mixing layer contains, on the one hand, older air masses within the so–called TIL branch, with high values of N^2 likely due to radiative adjustment. On the other hand, there are younger air masses with lower N^2 values within the mixing layer, which are above the dynamical and below the thermal tropopause within the so–called TFM branch. These lower N^2 values are most likely due to recent intrusion processes as a result of the permeability or so–called midlatitude breaks associated with the jet streams. The following questions concerning the TIL above the tropopause can be answered:

1. *Is there any relationship between mixing and static stability within the extratropical tropopause region?*
   Within the mixing layer, as revealed by SPURT and POLARCAT–GRACE O_3–CO tracer correlations, high N^2 is observed. Here, N^2 is related to an enhanced mixing degree f_{mix} in the extratropical mixing layer. This relation becomes even more pronounced if fresh mixing events within the TFM branch are excluded.

2. *What are the time scales of the TIL maintenance processes?*
   The higher correlation between N^2 and the mixing degree f_{mix} if the TFM branch is excluded indicates that mixing within the TIL probably occurs on larger than synoptic time scales. A temporal variance analysis of N^2 within the TIL branch during SPURT suggests that processes responsible for the composition of the TIL may occur on seasonal time scales. The other branch of the mixing layer, the TFM branch, reveals a variance on a synoptic time scale, which is typical of the quasi–isentropic mass exchange or of the midlatitude baroclinic instability. Backward trajectories with CLaMS reveal that N^2 is nearly unchanged over 10 days before entering the TIL branch during a SPURT or POLARCAT–GRACE flight. However, N^2 changes within these 10 days before entering the TFM branch.

3. *What kind of upper tropospheric flow is related to the TIL and TFM branches?*
   An analysis of the relative vorticity field ζ on the 200 hPa pressure level related to the SPURT flight positions reveals that both branches within the mixing layer are associated with both anticyclonic and cyclonic upper tropospheric systems. In particular, the upper tropospheric flow associated with the TIL branch is mainly anticyclonic, whereas that associated with the TFM branch is mainly cyclonic. The anticyclonic (cyclonic) activity is related to a larger (lower) N^2 maximum and thus a sharper tropopause within the TIL branch. In contrast, the TFM branch is characterized by a larger sharpness of the tropopause and a larger maximum of N^2 above the tropopause in the case of cyclonic activity compared to anticyclonic activity. The maximum of N^2 within the TFM branch is smaller related to a decreased sharpness of the tropopause for a subsample of the TFM branch with measurements in regions with a large difference between the thermal and the dynamical tropopause ($\mathrm{DTP_{dyn}} = 30 - 60\,\mathrm{K}$).

4. *Does mixing influence the thermal stratification via radiative adjustment within the UT/LS?*
   With radiative transfer calculations the influence of a change in O_3 and H_2O vertical gradients on the temperature gradient and thus on the static stability above the tropopause is analyzed. Here, the profiles are perturbed in a well–directed manner to

represent a non–mixed atmospheric state regarding a 'L–shaped' O_3 and H_2O correlation. The results indicate that the radiative response to increases in O_3 and H_2O near the tropopause caused by an increased mixing is followed by an enhancement of N^2. At the same time, the temperature above the tropopause decreases together with the development of an inversion and the TIL. In the idealized case of non–mixed profiles, i.e., 'L–shaped' O_3 and H_2O correlation, the TIL vanishes.

5. *Do O_3 and H_2O play comparable roles in maintaining the TIL?*
   The results suggest that H_2O plays the major role in maintaining the temperature inversion and the TIL structure compared to O_3. The TIL remained approximately unchanged if only O_3 is reduced to a constant mixing ratio within the stratosphere. If only H_2O is changed in the sense of non–mixing, the TIL will be destroyed.

6. *What is the dominant process in maintaining the TIL?*
   So far it has not been possible to identify a particular atmospheric process as the sole contributor to the maintenance of the TIL. The radiation may well be an important forcing mechanism in maintaining the TIL, but there are also dynamic mechanisms discussed by Wirth (2003), Birner (2006), Son and Polvani (2007) and also in Chapter 4.5 of this thesis. Model simulations based on the dry primitive equations by Son and Polvani (2007) revealed a TIL which is not as sharp as in observations. Contrary to Wirth (2003), who proposed the TIL as result of anticyclonic influences, the analysis of the relative vorticity field in this thesis revealed that the TIL is a phenomenon connected to both anticyclonic and cyclonic systems (see also Randel et al., 2007b). One may conclude that synoptic–scale balanced dynamics alone may not be sufficient to explain the quantitative features of the observed TIL and that radiative processes may play an additional important role for maintaining the TIL. To determine the exact contributions of radiation and dynamics to the TIL, further model studies are needed considering both the dynamics and the radiation.

In the third part of the thesis, a method is proposed for determining the jet cores $J_c(\theta)$ and the jet boundaries $J_b(\theta)$ including the meandering shape of the jet streams. These are based on the isentropic gradient of PV with equivalent latitude. An analysis of N^2 in combination with mixing on isentropes between the troposphere and the stratosphere across the tropopause and thus the jet streams is performed using water vapor and ozone correlations.
The determination of the jet core leads at the same time to a new definition of the tropopause. The PV gradient tropopause $\mathrm{TP}_{\mathrm{gradPV}}$ is based on the isentropic gradient of PV and can be used as an alternative of the dynamical tropopause, which is based on an ad–hoc assumption of a particular value of PV. This new tropopause describes the spatial dependence of

the PV in a more appropriate manner, depending on the prevailing situation in the atmosphere (tropopause breaks associated with secondary thermal tropopauses, tropopause foldings etc.). Finally, the following questions can be answered:

1. *What is the zonal and time mean PV distribution at TP_{gradPV} and what PV value represents the dynamical tropopause best within the northern hemisphere extratropics?*
   Depending on season, a zonal and time mean analysis of the PV distribution at $\mathrm{TP_{gradPV}}$ suggests roughly the $2.5\,\mathrm{PVU} - 3.5\,\mathrm{PVU}$ isolines as the dynamical tropopause in the northern hemisphere extratropics. The PV values at $\mathrm{TP_{gradPV}}$ are higher during summer (JJA) and autumn (SON) and lower during winter (DJF) and spring (MAM), respectively. In contrast, in the southern hemisphere, where a sharper gradient between the zonal and time mean PV at $\mathrm{TP_{gradPV}}$ than in the northern hemisphere appears from the midlatitudes to the pole, the zonal and time mean PV at $\mathrm{TP_{gradPV}}$ ranges between 2.0 PVU and 3.5 PVU.
   The commonly used 2 PVU isoline as the dynamical tropopause is, with a probability of around 51 % (11 %), representative of $\mathrm{TP_{gradPV}}$ during winter (DJF) (summer (JJA)) in the northern hemisphere. In winter (DJF) in the northern hemisphere, the mean percentage of PV at $\mathrm{TP_{gradPV}}$ is highest for PV=2.0 PVU. In summer, the most probable PV values at $\mathrm{TP_{gradPV}}$ are between PV=3.0−3.5 PVU. Based on the isentropic gradient of PV with equivalent latitude the analysis suggests that a particular PV value is not appropriate for the tropopause in the entire extratropics.

2. *Is there any seasonal dependence of the thermal stratification on isentropes across the jet streams?*
   An analysis of the static stability N^2 on isentropes both relative to the jet core in equivalent latitude differences φ_e and in the frame of water vapor and ozone tracer correlations shows a sharper increase of N^2 across the tropopause and the jet stream between the two jet boundaries (Region II) during winter than summer. The zonal and time mean N^2 is approximately constant with distance to the jet stream on the different isentropes (320 K, 340 K and 360 K) during summer and winter within the tropospheric branch of the isentropes toward the equator (Region I) and within the stratospheric branch of the isentropes toward the pole (Region III). The sharper increase of N^2 between the jet boundaries across the jet stream during winter shows the greater strength of the tropopause barrier and the tropopause sharpness during winter than summer. This is clearly evident from the nearly perfect 'L–shaped' correlation between the tropospheric tracer $\mathrm{H_2O}$ and the stratospheric tracer $\mathrm{O_3}$ between the jet boundaries during winter.

In the future, the statistical procedure for testing the comparability of data sets developed within this thesis will be adapted to other observational data sets. The analysis tools are not restricted to these particular data sets used here and are applicable to the comparison of different data sets, including model results, in a general sense. Thus, the tests are further suited for an evaluation and comparison with results from atmospheric models.

The results and the knowledge gained from the observation and model based analysis of the tropopause inversion layer in Chapter 4 forms a basis for further model evaluation regarding mixing processes in the UT/LS. In particular, the mixing procedure in CLaMS will be improved and validated with respect to the relation between mixing and N^2, which is discussed in this thesis. Today the mixing procedure in CLaMS is dependent on deformation, i.e., the wind shear $\partial u/\partial z$. A new parameterization will be developed, which includes N^2 according to the Gradient–Richardson number, which is dependent both on N^2 and $(\partial u/\partial z)^2$.

To understand the maintenance processes of the TIL in much more detail, further model studies including both radiation and dynamics within the atmosphere will be necessary. A common investigation of the dynamical and radiative processes in the UT/LS is necessary to further determine the exact contributions of radiative forcing and dynamics in the tropopause region in maintaining the TIL. A global climate model would be well suited for this purpose.

Bibliography

Ancellet, G., N. M. Beekman, and A. Papayannis, 1994: Impact of a cutoff low development on downward transport of ozone in the troposphere. *J. Geophys. Res*, **99**, 3451–3468.

Appenzeller, C. and H. C. Davies, 1992: Structure of stratospheric intrusions into the troposphere. *Nature*, **358**, 570–572.

Atticks, M. G. and G. D. Robinson, 1983: Some features of the structure of the tropical tropopause. *Quart. J. Roy. Meteorol. Soc.*, **109**, 295–308.

Bethan, S. G., G. Vaughan, and S. J. Reid, 1996: A comparison of ozone and thermal tropopause heights and the impact of tropopause definition on quantifying the ozone content of the troposphere. *Quart. J. Roy. Meteorol. Soc.*, **122**, 929–944.

Bian, J. and H. Chen, 2008: Statistics of the tropopause inversion layer over Beijing. *Adv. Atmos. Sci.*, **25**, 381–386.

Birner, T., 2006: Fine-scale structure of the extratropical tropopause region. *J. Geophys. Res.*, **111**, D04104, doi:10.1029/2005JD006301.

Birner, T., A. Dörnbrack, and U. Schumann, 2002: How sharp is the tropopause at midlatitudes? *Geophys. Res. Lett.*, **29(14)**, doi:10.1029/2002GL015142.

Birner, T., D. Sankey, and T. G. Shepherd, 2006: The tropopause inversion layer in models and analyses. *Geophys. Res. Lett.*, **33**, L14804, doi:10.1029/2006GL026549.

Bousserez, N., J. L. Attie, V. H. Peuch, M. Michou, G. Pfister, D. Edwards, L. Emmons, C. Mari, B. Barret, S. R. Arnold, A. Heckel, A. Richter, H. Schlager, A. Lewis, M. Avery, G. Sachse, E. V. Browell, and J. W. Hair, 2007: Evaluation of the MOCAGE chemistry transport model during the ICARTT/ITOP experiment. *J. Geophys. Res.*, **112**, D10S42, doi:10.1029/2006JD007595.

Brandt, S., 1999: *Data Analysis – Statistical and Computational Methods for Scientists and Engineers*. Springer Berlin, 686 pp.

Brenninkmeijer, C. A. M., P. Crutzen, F. Boumard, T. Dauer, B. Dix, R. Ebinghaus, D. Filippi, H. Fischer, H. Franke, U. Frieß, J. Heintzenberg, F. Helleis, M. Hermann, H. H. Kock, C. Koeppel, J. Lelieveld, M. Leuenberger, B. G. Martinsson, S. Miemczyk, H. P. Moret, H. N. Nguyen, P. Nyfeler, D. Oram, D. O'Sullivan, S. Penkett, U. Platt, M. Pupek, M. Ramonet, B. Randa, M. Reichelt, T. S. Rhee, J. Rohwer, K. Rosenfeld, D. Scharffe, H. Schlager, U. Schumann, F. Slemr, D. Sprung, P. Stock, R. Thaler, F. Valentino, P. van Velthoven, A. Waibel, A. Wandel, K. Waschitschek, A. Wiedensohler, I. Xueref-Remy, A. Zahn, U. Zech, and H. Ziereis, 2007: Civil aircraft for the regular investigation of the atmosphere based on an instrumented container: The new CARIBIC system. *Atmos. Chem. Phys*, **7**, 4953–4976.

Brewer, A. W., 1949: Evidence for a world circulation provided by the measurements of helium and water vapor distribution in the stratosphere. *Q. J. Roy. Meteor. Soc.*, **75**, 351–363.

Brioude, J., J.-P. Cammas, O. R. Cooper, and P. Nedelec, 2008: Characterization of the composition, structure, and seasonal variation of the mixing layer above the extratropical tropopause as revealed by MOZAIC measurements. *J. Geophys. Res.*, **113**, doi:10.1029/2007JD009184.

Brough, N., C. E. Reeves, S. A. Penkett, D. J. Stewart, K. Dewey, J. Kent, H. Barjat, P. S. Monks, H. Ziereis, P. Stock, H. Huntrieser, and H. Schlager, 2003: Intercomparison of aircraft instruments on board the C–130 and Falcon 20 over southern Germany during EXPORT 2000. *Atmos. Chem. Phys.*, **3**, 2127–2138.

Butchart, N. and E. E. Remsberg, 1986: The area of the stratospheric polar vortex from analyzed winds. *J. Atmos. Sci.*, **43**, 1319–1339.

Chen, P., 1995: Isentropic cross–tropopause mass exchange in the extratropics. *J. Geophys. Res.*, **100**, 16,661–16,673.

Choi, Y., Y. Wang, T. Zeng, D. Cunnold, E.-S. Yang, R. Martin, K. Chance, V. Thouret, and E. Edgerton, 2008: Springtime transitions of NO_2, CO, and O_3 over North America: Model evaluation and analysis. *J. Geophys. Res.*, **113**, D20311, doi:10.1029/2007JD009632.

Dessler, A. E., E. J. Hintsa, E. M. Weinstock, J. G. Anderson, and K. R. Chan, 1995: Mechanisms controlling water vapor in the lower stratosphere: "A tale of two stratospheres". *J. Geophys. Res.*, **100(D11)**, 23,167–23,172.

Dethof, A., A. O'Neill, and J. Slingo, 2000: Quantification of the isentropic mass transport across the dynamical tropopause. *J. Geophys. Res.*, **105**, 12,279–12,293.

Dobson, G. M. B., A. W. Brewer, and B. M. Cwilong, 1946: Meteorology of the lower stratosphere. *Proc. Roy. Soc. Lond. A*, **185**.

Ebisuzaki, W., 1997: A method to examine the statistical significance of a correlation when the data are serially correlated. *J. Climate*, **10**, 2147–2153.

Elbern, H., J. Hendricks, and A. Ebel, 1998: A climatology of tropopause folds by global analyses. *Theor. Appl. Climatol.*, **59**, 181–200, doi:10.1007/s007040050023.

Engel, A., H. Bönisch, D. Brunner, H. Fischer, H. Franke, G. Günther, C. Gurk, M. Hegglin, P. Hoor, R. Königstedt, M. Krebsbach, R. Maser, U. Parchatka, T. Peter, D. Schell, C. Schiller, U. Schmidt, N. Spelten, T. Szabo, U. Weers, H. Wernli, T. Wetter, and V. Wirth, 2006: Highly resolved observations of trace gases in the lowermost stratosphere and upper troposphere from the SPURT project: an overview. *Atmos. Chem. Phys.*, **6**, 283–310.

Ertel, H., 1942: Ein neuer hydrodynamischer Wirbelsatz. *Meteorol. Z.*, **59(9)**, 277–281.

Feck, T., 2009: *Wasserstoff–Emissionen und ihre Auswirkungen auf den arktischen Ozonverlust - Risikoanalyse einer globalen Wasserstoffwirtschaft*. Ph.D. thesis, University of Wuppertal.

Fels, S. B., J. D. Mahlmann, M. D. Schwarzkopf, and R. W. Sinclair, 1980: Stratospheric sensitivity of perturbations in ozone and carbon dioxide: radiative and dynamical response. *J. Atmos. Sci.*, **37**, 2265–2297.

Fischer, H., M. de Reus, M. Traub, J. Williams, J. Lelieveld, J. de Gouw, C. Warnecke, H. Schlager, A. Minikin, R. Scheele, and P. Siegmund, 2003: Deep convective injection of boundary layer air into the lowermost stratosphere at midlatitudes. *Atmos. Chem. Phys.*, **3**, 739–745.

Fischer, H., M. Lawrence, C. Gurk, P. Hoor, J. Lelieveld, M. I. Hegglin, D. Brunner, and C. Schiller, 2006: Model simulations and aircraft measurements of vertical, seasonal and latitudinal O_3 and CO distributions over Europe. *Atmos. Chem. Phys.*, **6**, 339–348.

Fischer, H., F. G. Wienhold, P. Hoor, O. Bujok, C. Schiller, P. Siegmund, M. Ambaum, H. A. Scheeren, and J. Lelieveld, 2000: Tracer correlations in the northern high latitude lowermost stratosphere: Influence of cross–tropopause mass exchange. *Geophys. Res. Lett.*, **27(1)**, 97–100.

Forster, P. M. and K. P. Shine, 2002: Assessing the climate impact of trends in stratospheric water vapor. *Geophys. Res. Lett.*, **29(6)**, doi:10.1029/2001GL013909.

Forster, P. M. d. F., 1999: Radiative forcing due to stratospheric ozone changes 1979–1997, using updated trend estimates. *J. Geophys. Res.*, **104**, 24,395–24,399.

Forster, P. M. d. F., R. S. Freckleton, and K. P. Shine, 1997: On aspects of the concept of radiative forcing. *Climate Dynamics*, **13**, 547–560.

Forster, P. M. d. F. and K. P. Shine, 1997: Radiative forcing and temperature trends from stratospheric ozone changes. *J. Geophys. Res.*, **102(D9)**, 10841–10855.

— 1999: Stratospheric water vapour changes as a possible contributor to observed stratospheric cooling. *Geophys. Res. Lett.*, **26**, 3309–3312.

Fueglistaler, S., A. E. Dessler, T. J. Dunkerton, I. Folkins, Q. Fu, and P. W. Mote, 2009: Tropical tropopause layer. *Rev. Geophys.*, **47**, doi:10.1029/2008RG000267.

Gerbig, C., S. Schmitgen, D. Kley, A. Volz-Thomas, K. Dewey, and D. Haaks, 1999: An improved fast–response vacuum–UV resonance fluorescence CO instrument. *J. Geophys. Res.*, **104**, 1699–1704.

Grooß, J.-U., 1996: *Modelling of Stratospheric Chemistry based on HALOE/UARS Satellite Data*. Ph.D. thesis, University of Mainz.

Grooß, J.-U. and J. M. Russell, 2005: Technical note: A stratospheric climatology for O_3, H_2O, CH_4, NO_x, HCl and HF derived from HALOE measurements. *Atmos. Chem. Phys.*, **5**, 2797–2807.

Haynes, P. and E. Shuckburgh, 2000a: Effective diffusivity as a diagnostic of atmospheric transport 1. stratosphere. *J. Geophys. Res.*, **NO. D18**, 22,777–22,794.

— 2000b: Effective diffusivity as a diagnostic of atmospheric transport 2. troposphere and lower stratosphere. *J. Geophys. Res.*, **105**, 22,795–22,810.

Hegglin, M. I., C. D. Boone, G. L. Manney, and K. A. Walker, 2009: A global view of the extratropical tropopause transition layer from atmospheric chemistry experiment fourier transform spectrometer O_3, H_2O and CO. *J. Geophys. Res.*, **114**, D00B11, doi:10.1029/2008JD009984.

Hegglin, M. I., D. Brunner, T. Peter, P. Hoor, H. Fischer, J. Stähelin, M. Krebsbach, C. Schiller, U. Parchatka, and U. Weers, 2006: Measurements of NO, NO_y, N_2O, and O_3 during SPURT: implications for transport and chemistry in the lowermost stratosphere. *Atmos. Chem. Phys.*, **6**, 1331–1350.

Hegglin, M. I., D. Brunner, H. Wernli, C. Schwierz, O. Martius, P. Hoor, H. Fischer, U. Parchatka, N. Spelten, C. Schiller, M. Krebsbach, U. Weers, J. Staehelin, and T. Peter, 2004: Tracing troposphere–to–stratosphere transport above a mid–latitude deep convective system. *Atmos. Chem. Phys.*, **4**, 741–756.

Helten, M., H. Smit, W. Sträter, D. Kley, P. Nedelec, M. Zöger, and R. Busen, 1998: Calibration and performance of automatic compact instrumentation for the measurement of relative humidity from passenger aircraft. *J. Geophys. Res.*, **103**, 25,643–25,652.

Hintsa, E. J., K. A. Boering, E. M. Weinstock, J. G. Anderson, B. L. Gary, L. Pfister, B. C. Daube, S. C. Wofsy, M. Loewenstein, J. R. Podolske, J. J. Margitan, and T. P. Bui, 1998: Troposphere–stratosphere transport in the lowermost stratosphere from measurements H_2O, CO_2, N_2O and O_3. *Geophys. Res. Lett.*, **25**, 2655–2658.

Hoerling, M. P., T. K. Schaack, and L. A. J., 1991: Global objective tropopause analysis. *Mon. Wea. Rev.*, **119**, 1816–1831.

Hoinka, K. P., 1996: The tropopause: discovery, definition and demarcation. *Meteorol. Z.*, **6**, 281–303.

— 1998: Statistics of the global tropopause pressure. *Mon. Wea. Rev.*, **126**, 3303–3325.

Holton, J. R., 2004: *An introduction to Dynamic Meteorology Fourth Edition*. Elsevier Academic Press Amsterdam Boston Heidelberg London New York Oxford Paris San Diego San Francisco Singapore Sydney Tokyo, 535 pp.

Holton, J. R. and A. Gettelman, 2001: Horizontal transport and the dehydration of the stratosphere. *Geophys. Res. Lett.*, **28**, 2799–2802.

Holton, J. R., P. H. Haynes, M. E. McIntyre, A. R. Douglass, R. B. Rood, and L. Pfister, 1995: Stratosphere–troposphere exchange. *Rev. Geophys.*, **33**, 403–440.

Hoor, P., H. Fischer, L. Lange, J. Lelieveld, and D. Brunner, 2002: Seasonal variations of a mixing layer in the lowermost stratosphere as identified by the CO–O_3 correlation from in–situ measurements. *J. Geophys. Res.*, **107**, doi:10.1029/2000JD000289.

Hoor, P., H. Fischer, and J. Lelieveld, 2005: Tropical and extratropical tropospheric air in the lowermost stratosphere over Europe: A CO–based budget. *Geophys. Res. Lett.*, **32**, doi:10.1029/2004GL022018.

Hoor, P., C. Gurk, D. Brunner, M. I. Hegglin, H. Wernli, and H. Fischer, 2004: Seasonality and extent of extratropical TST derived from in–situ CO measurements during $SPURT$. *Atmos. Chem. Phys.*, **4**, 1427–1442.

Hoskins, B. J., 1991: Towards a PV $-\theta$ view of the general circulation. *Tellus*, **43 B**, 27–35.

Hoskins, B. J. and F. P. Bretherton, 1972: Atmospheric frontogenesis models: mathematical formulation and solution. *J. Atmos. Sci*, **29**, 11–37.

Hoskins, B. J., M. E. McIntyre, and A. W. Robertson, 1985: On the use and significance of isentropic potential–vorticity maps. *Quart. J. Roy. Meteor. Soc.*, **111**, 877–946.

Juckes, M. N. and M. E. McIntyre, 1987: A high resolution one–layer model of breaking planetary waves in the stratosphere. *Nature*, **328**, 590–596.

Konopka, P., G. Günther, R. Müller, F. H. S. dos Santos, C. Schiller, F. Ravegnani, A. Ulanovsky, H. Schlager, C. M. Volk, S. Viciani, L. L. Pan, D.-S. McKenna, and M. Riese, 2007: Contribution of mixing to upward transport across the tropical tropopause layer (TTL). *Atmos. Chem. Phys.*, **7**, 3285–3308.

Krebsbach, M., C. Schiller, D. Brunner, G. Günther, M. I. Hegglin, D. Mottaghy, M. Riese, N. Spelten, and H. Wernli, 2006: Seasonal cycles and variability of O_3 and H_2O in the UT/LMS during SPURT. *Atmos. Chem. Phys.*, **6**, 109–125.

Kristjannsson, J. E., A. Staple, and J. Kristiansen, 2002: A new look at possible connections between solar activity, clouds and climate. *Geophys. Res. Let.*, **29(23)**, doi:10.1029/2002GL015646.

Kunz, A., P. Konopka, R. Müller, L. L. Pan, C. Schiller, and F. Rohrer, 2009: High static stability in the mixing layer above the extratropical tropopause. *J. Geophys. Res.*, **114**, D16305, doi:10.1029/2009JD011840.

Kunz, A., C. Schiller, F. Rohrer, H. G. J. Smit, P. Nedelec, and N. Spelten, 2008: Statistical analysis of water vapour and ozone in the UT/LS observed during SPURT and MOZAIC. *Atmos. Chem. Phys.*, **8**, 6603–6615.

Lamarque, J. F., A. O. Langford, and M. H. Profitt, 1996: Cross–tropopause mixing of ozone through gravity wave breaking: Observation and modeling. *J. Geophys. Res.*, **101**, 22,969–22,976.

Law, K. S., P. H. Plantevin, D. E. Shallcross, H. I. Rogers, and J. A. Pyle, 1998: Evaluation of modeled O_3 using measurement of ozone by airbus in-service aircraft (MOZAIC) data. *J. Geophys. Res.*, **103**, 25721–25737.

Luo, Z., D. Kley, R. H. Johnson, and H. Smit, 2008: Ten years of measurements of tropical upper–tropospheric water vapor by MOZAIC. Part II: Assessing the ECMWF humidity analysis. *J. Climate*, **21**, 1449–1466, doi:10.1175/2007JCLI1887.1.

Marenco, A., V. Thouret, P. Nedelec, H. Smit, M. Helten, D. Kley, F. Karcher, P. Simon, K. Law, J. Pyle, G. Poschmann, R. Von Wrede, C. Hume, and T. Cook, 1998: Measurements of ozone and water vapor by airbus in–service aircraft: The MOZAIC airborne program, an overview. *J. Geophys. Res.*, **103**, 25,631–25,642.

McIntyre, M. E. and T. N. Palmer, 1984: The "surf zone" in the stratosphere. *J. Atmos. Terr. Phys.*, **46**, 825–849.

McKenna, D. S., J.-U. Grooß, G. Günther, P. Konopka, R. Müller, G. Carver, and Y. Sasano, 2002a: A new Chemical Lagrangian Model of the Stratosphere (CLaMS) 2. Formulation of chemistry scheme and initialization. *J. Geophys. Res.*, **107(D15)**, doi:10.1029/2000JD000113.

McKenna, D. S., P. Konopka, J.-U. Grooß, G. Günther, R. Müller, R. Spang, D. Offermann, and Y. Orsolini, 2002b: A new Chemical Lagrangian Model of the Stratosphere (CLaMS) 1. Formulation of advection and mixing. *J. Geophys. Res.*, **107(D16)**, doi:10.1029/2000JD000114.

Mohanakumar, K., 2008: *Stratosphere Troposphere Interactions An Introduction*. Springer Netherlands, 416 pp.

Mote, P. W., T. J. Dunkerton, M. E. McIntyre, E. Ray, P. H. Haynes, and J. M. Russel, 1998: Vertical velocity, vertical diffusion, and dilution by midlatitude air in the tropical lower stratosphere. *J. Geophys. Res.*, **103**, 8651–8666.

Mote, P. W., K. H. Rosenlof, M. E. McIntyre, E. S. Carr, J. C. Gille, J. R. Holton, J. S. Kinnersley, H. C. Pumphrey, J. M. Russel, and J. W. Waters, 1996: An atmospheric tape recorder: The imprint of tropical tropopause temperatures on stratospheric water vapor. *J. Geophys. Res.*, **101**, 3989–4006.

Mottaghy, D., 2001: *Ozonmessungen in der unteren Stratosphäre*. Ph.D. thesis, Rheinisch-Westfälische Technische Hochschule Aachen, in cooperation with the Institute for Chemistry and Dynamics of the Geosphere, ICG-1: Stratosphere.

Nash, E. R., P. A. Newman, J. E. Rosenfield, and M. R. Schoeberl, 1996: An objective determination of the polar vortex using Ertel's potential vorticity. *J. Geophys. Res.*, **101**, 9471–9478.

Nedelec, P., J.-P. Cammas, V. Thouret, G. Athier, J. M. Cousin, C. Legrand, C. Abonnel, F. Lecoeur, G. Cayez, and C. Marizy, 2003: An improved infrared carbon monoxide analyser for routine measurements aboard commercial airbus aircraft: technical validation and first scientific results of the MOZAIC III programme. *Atmos. Chem. Phys.*, **3**, 1551–1564.

Nedelec, P., V. Thouret, J. Brioude, B. Sauvage, J.-P. Cammas, and A. Stohl, 2005: Extreme CO concentrations in the upper troposphere over northeast Asia in June 2003 from in situ MOZAIC aircraft data. *Geophys. Res. Let.*, **32**, L14807, doi:10.1029/2005GL023141.

Pan, L. L., K. P. Bowman, E. Atlas, S. C. Wofsy, F. Zhang, J. F. Bresch, B. A. Ridley, J. V. Pittman, C. Homeyer, P. Romashkin, and W. A. Cooper, 2009a: Stratosphere–troposphere analyses of regional transport experiment. *Bull. Amer. Meteor. Soc.*.

Pan, L. L., K. P. Bowman, M. Shapiro, W. J. Randel, R. S. Gao, T. Campos, C. Davis, S. Schauffler, B. A. Ridley, J. C. Wei, and C. Barnet, 2007a: Chemical behavior of the tropopause observed during the stratosphere–troposphere analyses of regional transport experiment. *J. Geophys. Res.*, **112**, D18110, doi:10.1029/2007JD008645.

Pan, L. L., P. Konopka, and E. V. Browell, 2006: Observations and model simulations of mixing near the extratropical tropopause. *J. Geophys. Res.*, **111**, D05106, doi:10.1029/2005JD006480.

Pan, L. L., W. J. Randel, B. L. Gary, M. J. Mahoney, and E. J. Hintsa, 2004: Definitions and sharpness of the extratropical tropopause: A trace gas perspective. *J. Geophys. Res.*, **109**, D23103, doi:10.1029/2004JD004982.

Pan, L. L., W. J. Randel, J. C. Gille, W. D. Hall, B. Nardi, S. Massie, V. Yudin, R. Khosravi, P. Konopka, and D. Tarasick, 2009b: Tropospheric intrusions associated with the secondary tropopause. *J. Geophys. Res.*, **114**, D10302, doi:10.1029/2008JD011374.

Pan, L. L., J. C. Wei, D. E. Kinnison, R. R. Garcia, D. J. Wuebbles, and G. P. Brasseur, 2007b: A set of diagnostics for evaluating chemistry–climate models in the extratropical tropopause region. *J. Geophys. Res.*, **112**, D09316, doi:10.1029/2006JD007792.

Patmore, N. and R. Toumi, 2006: An entropy–based measure of mixing at the tropopause. *Quart. J. Roy. Meteorol. Soc.*, **132**, 1949–1967.

Plöger, F., P. Konopka, G. Günther, J.-U. Grooß, and R. Müller, 2009: Impact of the vertical velocity scheme on modeling transport in the tropical tropopause layer. *J. Geophys. Res.*, in press, doi:10.1029/2009JD012023.

Poulida, O., R. R. Dickerson, and A. Heymsfield, 1996: Stratosphere–troposphere exchange in a midlatitude mesoscale convective complex. 1. observations. *J. Geophys. Res.*, **101**, 6823–6836.

Press, W. H., S. A. Teukolsky, W. T. Vetterling, and B. P. Flannery, 2002: Numerical recipes in C: the art of scientific computing. *Cambridge University Press, 2^{nd} ed.*, 691–692.

Quenouille, M. K., 1952: *Associated measurements*. Butterworths, 241 pp.

Ramanathan, V. and R. E. Dickinson, 1979: The role of stratospheric ozone in the zonal and seasonal radiative energy balance of the Earth–troposphere system. *J. Atmos. Sci.*, **36**, 1084–1104.

Randel, W. J., R. R. Garcia, and F. Wu, 2002: Time–dependent upwelling in the tropical lower stratosphere estimated from the zonal–mean momentum budget. *J. Atmos. Sci*, **59**, 2141–2152.

Randel, W. J., D. J. Seidel, and L. L. Pan, 2007a: Observational characteristics of double tropopauses. *J. Geophys. Res.*, **112**, D07309, doi:10.1029/2006JD007904.

Randel, W. J., F. Wu, and P. Forster, 2007b: The extratropical tropopause inversion layer: Global observations with GPS data, and a radiative forcing mechanism. *J. Atmos. Sci.*, **64**, 4489–4496, doi:10.1175/2007JAS2412.1.

Rao, T. N., J. Arvelius, and S. Kirkwood, 2008: Climatology of tropopause folds over a European Arctic station (Esrange). *J. Geophys. Res.*, **113**, doi:10.1029/2007JD009638.

IPCC, 1996: *Climate Change 1995. The IPCC Second Scientific Assessment Report*.

Rohrer, F. and H. Berresheim, 2006: Strong correlation between levels of tropospheric hydroxyl radicals and solar ultraviolet radiation. *Nature*, **442**, 184–187, doi:10.1029/2000JD000114.

Sachs, L. and J. Hedderich, 2006: *Angewandte Statistik - Methodensammlung mit R*. Springer Berlin Heidelberg New York, 702 pp.

Sankey, D. and T. G. Shepherd, 2003: Correlations of long–lived chemical species in a middle atmosphere general circulation model. *J. Geophys. Res.*, **108**, doi:10.1029/2002JD002799.

Santer, B. D., M. F. Wehner, T. M. L. Wigley, R. Sausen, G. A. Meehl, K. E. Taylor, C. Ammann, J. Arblaster, W. M. Washington, J. S. Boyle, and W. Brüggemann, 2003: Contributions on anthropogenic and natural forcing to recent tropopause height changes. *Science*, **301**, 479–483.

Schiller, C., J.-U. Grooß, P. Konopka, F. Plöger, F. H. Silva dos Santos, and N. Spelten, 2009: Hydration and dehydration at the tropical tropopause. *Atmos. Chem. Phys. Discuss.*, **9**, 17495–17529.

Schoeberl, M. R., L. R. Lait, P. A. Newman, and J. E. Rosenfield, 1992: The structure of the polar vortex. *J. Geophys. Res.*, **97(8)**, 7859–7882.

Shapiro, M. A., 1980: Turbulent mixing within tropopause folds as a mechanism for the exchange of chemical constituents between the stratosphere and the troposphere. *J. Atmos. Sci.*, **37**, 994–1004.

Shepherd, T. G., 2002: Issues in stratosphere–troposphere coupling. *J. Meteorol. Soc. Jpn.*, **80**, 769–792.

— 2007: Transport in the middle atmosphere. *J. Meteorol. Soc. Jpn.*, **85B**, 165–191.

Sherwood, S. C. and A. E. Dessler, 2001: A model for transport across the tropical tropopause. *J. Atmos. Sci.*, **58**, 765–779.

Shine, K. P., 1991: On the cause of relative greenhouse strength of gases such as the halocarbons. *J. Atmos. Sci*, **48**, 1513–1518.

Simmons, A., M. Hortal, G. Kelly, A. McNally, A. Untch, and S. Uppala, 2005: ECMWF analyses and forecasts of stratospheric winter polar vortex breakup: September 2002 in the southern hemisphere and related events. *J. Atmos. Sci.*, **62**, 668–689.

Smit, H. G. J., A. Volz-Thomas, M. Helten, W. Paetz, and D. Kley, 2008: An in–flight calibration method for real–time humidity measurements with the airborne MOZAIC sensor. *J. Atmos. and Ocean. Techn.*, doi:10.1175/2007JTECHA975.1.

Son, S. W. and L. M. Polvani, 2007: Dynamical formation of an extra–tropical tropopause inversion layer in a relatively simple general circulation model. *Geophys. Res. Lett.*, **34**, L17806, doi:10.1029/2007GL030564.

Søvde, O. A., M. Gauss, S. P. Smyshlyaev, and I. S. A. Isaksen, 2008: Evaluation of the chemical transport model Oslo CTM2 with focus on Arctic winter ozone depletion. *J. Geophys. Res.*, **113**, D09304, doi:10.1029/2007JD009240.

Sprenger, M., M. Croci Maspoli, and H. Wernli, 2003: Tropopause folds and cross–tropopause exchange: A global investigation based upon ECMWF analyses for the time period March 2000 to February 2001. *J. Geophys. Res.*, **108(D12)**, doi:10.1029/2002JD002587.

Sprenger, M., H. Wernli, and M. Bourqui, 2007: Stratosphere–troposphere exchange and its relation to potential vorticity streamers and cut–offs near the extratropical tropopause. *J. Atmos. Sci.*, **64**, 1587–1602, doi:10.1175/JAS3911.1.

Steinhorst, H.-M., P. Konopka, G. Günther, and M. R., 2005: How permeable is the edge of the Arctic vortex: Model studies of winter 1999–2000. *J. Geophys. Res.*, **110**, D06105, doi:10.1029/2004JD005268.

Stohl, A., P. Bonasoni, P. Cristofanelli, W. Collins, J. Feichter, A. Frank, C. Forster, E. Gerasopoulos, H. Gäggeler, P. James, T. Kentarchos, H. Kromp-Kolb, B. Krüger, C. Land, J. Meloen, A. Papayannis, A. Priller, P. Seibert, M. Sprenger, G. J. Roelofs, H. Scheell, C. E. Schnabel, P. Siegmund, L. Tobler, T. Trickl, H. Wernli, V. Wirth, P. Zanis, and C. Zerefos, 2003: Stratosphere-troposphere exchange: A review, and what we have learned from STACCATO. *J. Geophys. Res.*, **108**, doi:10.1029/2002JD002490.

Thouret, V., J.-P. Cammas, B. Sauvage, G. Athier, R. Zbinden, R. Nedelec, P. Simon, and F. Karcher, 2006: Tropopause referenced ozone climatology and inter-annual variability (1994–2003) from the MOZAIC programme. *Atmos. Chem. Phys.*, **6**, 1033–1051.

Thouret, V., A. Marenco, J. Logan, P. Nedelec, and C. Grouhel, 1998: Comparisons of ozone measurements from the MOZAIC airborne program and the ozone sounding network at eight locations. *J. Geophys. Res.*, **103**, 25695–25720.

Toenges-Schuller, N., O. Stein, F. Rohrer, A. Wahner, A. Richter, J. P. Burrows, S. Beirle, T. Wagner, U. Platt, and C. D. Elvidge, 2006: Global distribution pattern of anthropogenic nitrogen oxide emissions: Correlation analysis of satellite measurements and model calculations. *J. Geophys. Res.*, **111**, D05312, doi:10.1029/2005JD006068.

Wernli, H. and M. Sprenger, 2007: Identification and ERA–15 climatology of potential vorticity streamers and cutoffs near the extratropical tropopause. *J. Atmos. Sci.*, **64**, 1569–1586, doi:10.1175/JAS3912.1.

Wienhold, F., H. Fischer, P. Hoor, V. Wagner, R. Konigstedt, G. Harris, J. Anders, R. Grisar, M. Knothe, W. Riedel, F. Lübken, and T. Schilling, 1998: TRISTAR–a tracer in situ TDLAS for atmospheric research. *App. Phys. B–Lasers and Optics*, **67**, 411–417.

Wirth, V., 2000: Thermal versus dynamical tropopause in upper-tropospheric balanced flow anomalies. *Quart. J. Roy. Meteor. Soc.*, **126**, 299–317.

— 2001: Cyclone–anticyclone asymmetry concerning the height of the thermal and dynamical tropopause. *J. Atmos. Sci*, **58**, 26–37.

— 2003: Static stability in the extratropical tropopause region. *J. Atmos. Sci.*, **60**, 1395–1409.

— 2004: A dynamical mechanism for tropopause sharpening. *Meteor. Z.*, **13**, 477–484.

Wirth, V. and T. Szabo, 2007: Sharpness of the extratropical tropopause in baroclinic life cycle experiments. *Geophys. Res. Lett.*, **34**, L02809, doi:10.1029/2006GL028369.

WMO, 1957: *Meteorology–A three–dimensional science*. WMO Bull (6), 134-138 pp.

— 1986: *Atmospheric ozone*. WMO Rep. (16).

Zahn, A., C. A. M. Brenninkmeijer, and P. F. J. van Velthoven, 2004: Passenger aircraft project CARIBIC 1997–2002, Part I: the extratropical chemical tropopause. *Atmos. Chem. Phys. Discuss.*, **4**, 1091–1117.

Zierl, B. and V. Wirth, 1997: The role of radiation for stratosphere-troposphere exchange in an upper tropospheric anticyclone. *J. Geophys. Res.*, **102**, 23,883–23,894.

Zöger, M., A. Afchine, N. Eicke, M.-T. Gerhards, E. Klein, D. S. McKenna, U. Mörschel, U. Schmidt, V. Tan, F. Tuitjer, T. Woyke, and C. Schiller, 1999: Fast in situ stratospheric hygrometers: A new family of balloon-borne and airborne Lyman α photofragment fluorescence hygrometers. *J. Geophys. Res.*, **104**, 1807–1816.

Acknowledgments

This thesis benefits from the cooperation, help and support from a number of persons.
I address my first thanks to Prof. Dr. Martin Riese and to Dr. Cornelius Schiller for offering the possibility to work at the ICG–1 (Forschungszentrum Jülich) and for their trust in my work and freedom in scientific questions. Thanks for the opportunity to contribute to interesting scientific conferences as well as workshops, to publish the results of this thesis in scientific journals, to participate in a summer school in Athens and in the POLARCAT campaign in Kangerlussuaq (Greenland). Thanks also for the frequent discussions on the scientific results of my thesis both in personal communications with Cornelius and in the monthly 'Ph.D. talks' with Martin.
I am also grateful to Prof. Dr. Andreas Wahner for the possibility to prepare my Ph.D.–thesis in cooperation between the ICG–2 (Forschungszentrum Jülich) and the ICG–1 as well as to Prof. Dr. Ralf Koppmann for the supervision of this thesis as the second examiner.
Sincere thanks to Dr. Paul Konopka and Dr. Rolf Müller for the good collaboration and the precious discussions on the results concerning the processes within the tropopause region. Thank you for the introduction to the CLaMS model and its use, respectively. I could always trust in you concerning an arranged date for the proofread of several workings.
Dr. Franz Rohrer for the discussions in the statistical analyses and the good collaboration concerning the two scientific publications. Dr. Herman Smit and Dr. Andreas Volz–Thomas for the use of the MOZAIC data and the discussions on the quality and interpretation of these data. The discussions were very worthwhile for the statistical analyses of these data.
I also thank Reimar Bauer and Nicole Thomas for technical support and help with programming skills.
Sincere thanks are given to Dr. Laura Pan for the cooperation and scientific discussions concerning the work on the link between static stability and mixing in the UT/LS, to Dr. Peter Hoor for the invitation to a talk in the Meteorology colloquia at the University of Mainz and the scientific discussions, and to Prof. Dr. Thomas Birner for the discussions on the results concerning the possible tropopause inversion layer forcing processes.
Many thanks to Dr. Samuel Oltmans for the use of the Boulder sonde data, to Dr. Philippe Nedelec for the use of the MOZAIC ozone data and also to the SPURT and POLARCAT communities for the use of the water vapor, ozone and carbon monoxide in–situ data.
Special thanks to Nicole Spelten for the little piece of home in the distance and to the entire ICG–1 for the pleasant working atmosphere.
I want to express my gratitude also to the Helmholtz Gemeinschaft for the support of this thesis within the HGF programme EOS (Earth Observing System).

1. **Einsatz von multispektralen Satellitenbilddaten in der Wasserhaushalts- und Stoffstrommodellierung – dargestellt am Beispiel des Rureinzugsgebietes**
   von C. Montzka (2008), XX, 238 Seiten
   ISBN: 978-3-89336-508-1

2. **Ozone Production in the Atmosphere Simulation Chamber SAPHIR**
   by C. A. Richter (2008), XIV, 147 pages
   ISBN: 978-3-89336-513-5

3. **Entwicklung neuer Schutz- und Kontaktierungsschichten für Hochtemperatur-Brennstoffzellen**
   von T. Kiefer (2008), 138 Seiten
   ISBN: 978-3-89336-514-2

4. **Optimierung der Reflektivität keramischer Wärmedämmschichten aus Yttrium-teilstabilisiertem Zirkoniumdioxid für den Einsatz auf metallischen Komponenten in Gasturbinen**
   von A. Stuke (2008), X, 201 Seiten
   ISBN: 978-3-89336-515-9

5. **Lichtstreuende Oberflächen, Schichten und Schichtsysteme zur Verbesserung der Lichteinkopplung in Silizium-Dünnschichtsolarzellen**
   von M. Berginski (2008), XV, 171 Seiten
   ISBN: 978-3-89336-516-6

6. **Politikszenarien für den Klimaschutz IV – Szenarien bis 2030**
   hrsg.von P. Markewitz, F. Chr. Matthes (2008), 376 Seiten
   ISBN 978-3-89336-518-0

7. **Untersuchungen zum Verschmutzungsverhalten rheinischer Braunkohlen in Kohledampferzeugern**
   von A. Schlüter (2008), 164 Seiten
   ISBN 978-3-89336-524-1

8. **Inorganic Microporous Membranes for Gas Separation in Fossil Fuel Power Plants**
   by G. van der Donk (2008), VI, 120 pages
   ISBN: 978-3-89336-525-8

9. **Sinterung von Zirkoniumdioxid-Elektrolyten im Mehrlagenverbund der oxidkeramischen Brennstoffzelle (SOFC)**
   von R. Mücke (2008), VI, 165 Seiten
   ISBN: 978-3-89336-529-6

10. **Safety Considerations on Liquid Hydrogen**
    by K. Verfondern (2008), VIII, 167 pages
    ISBN: 978-3-89336-530-2

11. **Kerosinreformierung für Luftfahrtanwendungen**
    von R. C. Samsun (2008), VII, 218 Seiten
    ISBN: 978-3-89336-531-9

12. **Der 4. Deutsche Wasserstoff Congress 2008 – Tagungsband**
    hrsg. von D. Stolten, B. Emonts, Th. Grube (2008), 269 Seiten
    ISBN: 978-3-89336-533-3

13. **Organic matter in Late Devonian sediments as an indicator for environmental changes**
    by M. Kloppisch (2008), XII, 188 pages
    ISBN: 978-3-89336-534-0

14. **Entschwefelung von Mitteldestillaten für die Anwendung in mobilen Brennstoffzellen-Systemen**
    von J. Latz (2008), XII, 215 Seiten
    ISBN: 978-3-89336-535-7

15. **RED-IMPACT**
    Impact of Partitioning, Transmutation and Waste Reduction Technologies on the Final Nuclear Waste Disposal
    SYNTHESIS REPORT
    ed. by W. von Lensa, R. Nabbi, M. Rossbach (2008), 178 pages
    ISBN 978-3-89336-538-8

16. **Ferritic Steel Interconnectors and their Interactions with Ni Base Anodes in Solid Oxide Fuel Cells (SOFC)**
    by J. H. Froitzheim (2008), 169 pages
    ISBN: 978-3-89336-540-1

17. **Integrated Modelling of Nutrients in Selected River Basins of Turkey**
    Results of a bilateral German-Turkish Research Project
    project coord. M. Karpuzcu, F. Wendland (2008), XVI, 183 pages
    ISBN: 978-3-89336-541-8

18. **Isotopengeochemische Studien zur klimatischen Ausprägung der Jüngeren Dryas in terrestrischen Archiven Eurasiens**
    von J. Parplies (2008), XI, 155 Seiten, Anh.
    ISBN: 978-3-89336-542-5

19. **Untersuchungen zur Klimavariabilität auf dem Tibetischen Plateau - Ein Beitrag auf der Basis stabiler Kohlenstoff- und Sauerstoffisotope in Jahrringen von Bäumen waldgrenznaher Standorte**
    von J. Griessinger (2008), XIII, 172 Seiten
    ISBN: 978-3-89336-544-9

20. **Neutron-Irradiation + Helium Hardening & Embrittlement Modeling of 9%Cr-Steels in an Engineering Perspective (HELENA)**
by R. Chaouadi (2008), VIII, 139 pages
ISBN: 978-3-89336-545-6

21. **Messung und Bewertung von Verkehrsemissionen**
von D. Klemp, B. Mittermaier (2009), ca. 230 Seiten
ISBN: 978-3-89336-546-3

22. **Verbundvorhaben APAWAGS (AOEV und Wassergenerierung) – Teilprojekt: Brennstoffreformierung – Schlussbericht**
von R. Peters, R. C. Samsun, J. Pasel, Z. Porš, D. Stolten (2008), VI, 106 Seiten
ISBN: 978-3-89336-547-0

23. **FREEVAL**
Evaluation of a Fire Radiative Power Product derived from Meteosat 8/9 and Identification of Operational User Needs
Final Report
project coord. M. Schultz, M. Wooster (2008), 139 pages
ISBN: 978-3-89336-549-4

24. **Untersuchungen zum Alkaliverhalten unter Oxycoal-Bedingungen**
von C. Weber (2008), VII, 143, XII Seiten
ISBN: 978-3-89336-551-7

25. **Grundlegende Untersuchungen zur Freisetzung von Spurstoffen, Heißgaschemie, Korrosionsbeständigkeit keramischer Werkstoffe und Alkalirückhaltung in der Druckkohlenstaubfeuerung**
von M. Müller (2008), 207 Seiten
ISBN: 978-3-89336-552-4

26. **Analytik von ozoninduzierten phenolischen Sekundärmetaboliten in *Nicotiana tabacum* L. cv Bel W3 mittels LC-MS**
von I. Koch (2008), III, V, 153 Seiten
ISBN 978-3-89336-553-1

27. **IEF-3 Report 2009. Grundlagenforschung für die Anwendung**
(2009), ca. 230 Seiten
ISBN: 978-3-89336-554-8

28. **Influence of Composition and Processing in the Oxidation Behavior of MCrAlY-Coatings for TBC Applications**
by J. Toscano (2009), 168 pages
ISBN: 978-3-89336-556-2

29. **Modellgestützte Analyse signifikanter Phosphorbelastungen in hessischen Oberflächengewässern aus diffusen und punktuellen Quellen**
von B. Tetzlaff (2009), 149 Seiten
ISBN: 978-3-89336-557-9

30. **Nickelreaktivlot / Oxidkeramik – Fügungen als elektrisch isolierende Dichtungskonzepte für Hochtemperatur-Brennstoffzellen-Stacks**
von S. Zügner (2009), 136 Seiten
ISBN: 978-3-89336-558-6

31. **Langzeitbeobachtung der Dosisbelastung der Bevölkerung in radioaktiv kontaminierten Gebieten Weißrusslands – Korma-Studie**
von H. Dederichs, J. Pillath, B. Heuel-Fabianek, P. Hill, R. Lennartz (2009), Getr. Pag.
ISBN: 978-3-89336-532-3

32. **Herstellung von Hochtemperatur-Brennstoffzellen über physikalische Gasphasenabscheidung**
von N. Jordán Escalona (2009), 148 Seiten
ISBN: 978-3-89336-532-3

33. **Real-time Digital Control of Plasma Position and Shape on the TEXTOR Tokamak**
by M. Mitri (2009), IV, 128 Seiten
ISBN: 978-3-89336-567-8

34. **Freisetzung und Einbindung von Alkalimetallverbindungen in kohlebefeuerten Kombikraftwerken**
von M. Müller (2009), 155 Seiten
ISBN: 978-3-89336-568-5

35. **Kosten von Brennstoffzellensystemen auf Massenbasis in Abhängigkeit von der Absatzmenge**
von J. Werhahn (2009), 242 Seiten
ISBN: 978-3-89336-569-2

36. **Einfluss von Reoxidationszyklen auf die Betriebsfestigkeit von anodengestützten Festoxid-Brennstoffzellen**
von M. Ettler (2009), 138 Seiten
ISBN: 978-3-89336-570-8

37. **Großflächige Plasmaabscheidung von mikrokristallinem Silizium für mikromorphe Dünnschichtsolarmodule**
von T. Kilper (2009), XVII, 154 Seiten
ISBN: 978-3-89336-572-2

38. **Generalized detailed balance theory of solar cells**
von T. Kirchartz (2009), IV, 198 Seiten
ISBN: 978-3-89336-573-9

39. **The Influence of the Dynamic Ergodic Divertor on the Radial Electric Field at the Tokamak TEXTOR**
von J. W. Coenen (2009), xii, 122, XXVI Seiten
ISBN: 978-3-89336-574-6

40. **Sicherheitstechnik im Wandel Nuklearer Systeme**
von K. Nünighoff (2009), viii, 215 Seiten
ISBN: 978-3-89336-578-4

41. **Pulvermetallurgie hochporöser NiTi-Legierungen für Implanat- und Dämpfungsanwendungen**
von M. Köhl (2009), XVII, 199 Seiten
ISBN: 978-3-89336-580-7

42. **Einfluss der Bondcoatzusammensetzung und Herstellungsparameter auf die Lebensdauer von Wärmedämmschichten bei zyklischer Temperaturbelastung**
von M. Subanovic (2009), 188, VI Seiten
ISBN: 978-3-89336-582-1

43. **Oxygen Permeation and Thermo-Chemical Stability of Oxygen Permeation Membrane Materials for the Oxyfuel Process**
by A. J. Ellett (2009), 176 Seiten
ISBN: 978-3-89336-581-4

44. **Korrosion von polykristallinem Aluminiumoxid (PCA) durch Metalljodidschmelzen sowie deren Benetzungseigenschaften**
von S. C. Fischer (2009), 148 Seiten
ISBN: 978-3-89336-584-5

45. **IEF-3 Report 2009. Basic Research for Applications**
(2009), 217 Seiten
ISBN: 978-3-89336-585-2

46. **Verbundvorhaben ELBASYS (Elektrische Basissysteme in einem CFK-Rumpf) - Teilprojekt: Brennstoffzellenabgase zur Tankinertisierung - Schlussbericht**
von R. Peters, J. Latz, J. Pasel, R. C. Samsun, D. Stolten
(2009), xi, 202 Seiten
ISBN: 978-3-89336-587-6

47. **Aging of ^{14}C-labeled Atrazine Residues in Soil: Location, Characterization and Biological Accessibility**
by N. D. Jablonowski (2009), IX, 104 Seiten
ISBN: 978-3-89336-588-3

48. **Entwicklung eines energetischen Sanierungsmodells für den europäischen Wohngebäudesektor unter dem Aspekt der Erstellung von Szenarien für Energie- und CO_2 - Einsparpotenziale bis 2030**
von P. Hansen (2009), XXII, 281 Seiten
ISBN: 978-3-89336-590-6

49. **Reduktion der Chromfreisetzung aus metallischen Interkonnektoren für Hochtemperaturbrennstofzellen durch Schutzschichtsysteme**
von R. Trebbels (2009), iii, 135 Seiten
ISBN: 978-3-89336-591-3

50. **Bruchmechanische Untersuchung von Metall / Keramik-Verbundsystemen für die Anwendung in der Hochtemperaturbrennstoffzelle**
von B. Kuhn (2009), 118 Seiten
ISBN: 978-3-89336-592-0

51. **Wasserstoff-Emissionen und ihre Auswirkungen auf den arktischen Ozonverlust**
Risikoanalyse einer globalen Wasserstoffwirtschaft
von T. Feck (2009), 180 Seiten
ISBN: 978-3-89336-593-7

52. **Development of a new Online Method for Compound Specific Measurements of Organic Aerosols**
by T. Hohaus (2009), 156 Seiten
ISBN: 978-3-89336-596-8

53. **Entwicklung einer FPGA basierten Ansteuerungselektronik für Justageeinheiten im Michelson Interferometer**
von H. Nöldgen (2009), 121 Seiten
ISBN: 978-3-89336-599-9

54. **Observation – and model – based study of the extratropical UT/LS**
by A. Kunz (2010), xii, 120, xii Seiten
ISBN: 978-3-89336-603-3

Energie & Umwelt / Energy & Environment
Band / Volume 54
ISBN 978-3-89336-603-3

JÜLICH
FORSCHUNGSZENTRUM